Synthesis, Purification and Characterization of Ferredoxins with Re-Designed Active Sites

Kristensen, Jytte

Publication date:
2010

Document Version
Publisher's PDF, also known as Version of record

Synthesis, Purification and Characterization of Ferredoxins with Re-Designed Active Sites

Ph.D. Thesis by
Jytte Kristensen

Department of Chemistry
Technical University of Denmark

2010

Synthesis, purification and Characterization of Ferredoxins with Re-Designed Active Sites

Ph.D. Thesis by
Jytte Kristensen

Department of Chemistry
Technical University of Denmark

2010

Preface

The present dissertation is submitted in partial fulfillment of the requirements of the degree of Doctor of Philosophy at the Technical University of Denmark (DTU). The Ph.D. scholarship was funded by DTU and the work was carried out at Department of Chemistry at DTU from January 2007 to March 2010 with the late Associate Professor Bee Lean Ooi and Associate Professor Hans E. M. Christensen as main supervisors, while Professor Jens Ulstrup and Associate Professor Jingdong Zhang functioned as co-supervisors.

First of all I wish to thank all my supervisors for their great help and support throughout the process, especially during the difficult periods and during Bee Lean's disease.

A special thank goes to Professor Wilfred R. Hagen at Delft University of Technology (Netherlands) for allowing me into his laboratories and for his valuable practical and analytical help and guidance with electron paramagnetic resonance spectroscopic characterization. I also wish to thank the members of his group for making my two stays in Delft enjoyable. The Danish Chemical Society is acknowledged for financing the second visit to Delft.

Parts of the results presented in the thesis were presented at the 14th International Conference on Biological Inorganic Chemistry (ICBIC 14). The financial support for participation in this conference from the Otto Mønsted Foundation is greatly appreciated.

I also wish to thank the members of the Metalloprotein Chemistry Group and Nanoscale Chemistry Group for having helped me during my project and for providing a nice and friendly atmosphere. Many thanks are owed to Ph.D. student Maja Martic for carrying out numerous mass spectrometric experiments. Special thoughts go to Laboratory Technicians Lise-Lotte Jespersen, Stefanie Boy and Martin Hasling Pedersen.

Finally I want to thank Ph.D. student Anders C. Raffalt for not only helping me with parts of the characterization, but also for an ongoing friendship and for sharing frustrations and successes.

_____

Jytte Kristensen
Kgs. Lyngby, 26th of April 2010.

Abstract

Iron-sulfur proteins with cuboidal [Fe_4S_4] clusters exhibit a remarkable functional diversity. Insights on the factors determining the function of the protein can be obtained by modifications of the metal site by incorporation of metals other than iron in the active site of the protein. This approach further has interesting perspectives in the design of new biologically based catalytic systems. This project presents two strategies for incorporation of non-natural metals in iron-sulfur proteins.

These studies are based on the ferredoxin from *Pyrococcus furiosus*. This ferredoxin can contain either a [Fe_3S_4] cluster or a [Fe_4S_4] cluster. One new protein was synthesized by incorporating cobalt into the [Fe_3S_4] cluster thus creating a [$CoFe_3S_4$] cluster. The other artificial protein was designed by replacement of the iron-sulfur cluster with a synthetic [Mo_4S_4] cluster. The synthesis, purification and characterization of the two new proteins were carried out. The *P. furiosus* ferredoxin was studied as a reference for the two artificial proteins.

The *P. furiosus* [Fe_3S_4] and [Fe_4S_4] ferredoxins were studied with cyclic voltammetry as reference for the work on the artificial proteins. The effects of different buffer systems and additives were tested to find the optimal conditions for electrochemical characterization. Different buffer systems did not have a significant effect, but the voltammograms were strongly dependent on the NaCl content as NaCl had an attenuating effect on the redox signals of the *P. furiosus* ferredoxins.

The *P. furiosus* ferredoxin with the heterometallic [$CoFe_3S_4$] cluster was synthesized and purified in the oxidized [$CoFe_3S_4]^{2+}$ state. The chromatographic, mass spectrometric and EPR spectroscopic results indicated that the [$CoFe_3S_4]^{2+}$ ferredoxin was purified to high purity and that the protein was stable under the used conditions. These results are in disagreement with previous reports of readily oxidative degradation of the [$CoFe_3S_4]^{2+}$ ferredoxin to [$Fe_3S_4]^{+}$ ferredoxin. Experiments with chemical reduction and oxidation suggested a redox active protein and this was confirmed by cyclic voltammetry. One well-defined pair of redox peaks appeared and the pair was assigned to the [$CoFe_3S_4]^{2+/+}$ redox couple and had a formal potential of -177 mV versus SHE.

Unlike the naturally occurring iron-sulfur cluster the molybdenum-sulfur cluster is not incorporated into the ferredoxin by self-assembly. Instead the molybdenum-sulfur analogue was synthesized by addition of pre-prepared [$Mo_4S_4(H_2O)_{12}]Cl_5$ to the apo-

ferredoxin which was stabilized by sulfonation. The purification of the molybdenum-sulfur analogue revealed two closely related species and that the ratio between the two species depended on the experimental conditions. The two purified species were subjected to EPR monitored redox titration and the obtained EPR spectra were compared to the spectra of $[Mo_4S_4(H_2O)_{12}]^{5+}$. The results confirmed the incorporation of the intact $[Mo_4S_4]$ cluster and suggested stabilization of the cluster in three oxidation states; the 4+, 5+ and 6+ states. The formal potentials of the transitions between the three oxidation states were determined to -195 mV and -295 mV versus SHE for the first species and -205 mV and -380 mV versus SHE for the other species. The obtained spectra after oxidative titration suggested oxidative break down of the $[Mo_4S_4]$ cluster. It is not possible to identify the ligands on the cluster based on these studies, however, the spectra suggest that the difference between the two species in variations in the ligand environment.

These studies have given important insights on these new proteins and have increased the understanding of ferredoxins with re-designed active sites. This is an important step for use of these proteins in new catalytic systems.

Resumé

Jern-svovl proteiner med kubiske [Fe_4S_4] klynger udviser en bemærkelsesværdig diversitet i funktion. Der kan opnås forståelse af de afgørende faktorer for proteinets funktion ved at modificere metal centeret ved at indsætte andre metaller end jern i det aktive center. Denne metode har yderligere interessante perspektiver for design af nye biologisk baserede katalytiske systemer. I dette projekt præsenteres to strategier for indsættelse af ikke-naturlige metaller i jern-svovl proteiner.

Disse studier er baseret på ferredoxin fra *Pyrococcus furiosus*. Denne ferredoxin kan have enten en [Fe_3S_4] klynge eller en [Fe_4S_4] klynge. Det ene nye protein blev fremstillet ved at indsætte kobolt i [Fe_3S_4] klyngen og derved danne en [$CoFe_3S_4$] klynge. I det andet kunstige protein blev jern-svovl klyngen udskiftet med en syntetisk [Mo_4S_4] klynge. De nye proteiner blev syntetiseret, oprenset og karakteriseret. *P. furiosus* ferredoxin blev studeret som reference for studierne af de kunstige proteiner.

P. furiosus [Fe_3S_4] og [Fe_4S_4] ferredoxin blev studeret ved cyklisk voltammetri som reference for arbejdet med de kunstige proteiner. Effekterne af forskellige puffer systemer og tilsatte stoffer blev testet for at finde de optimale betingelser for elektrokemisk karakterisering. Variation af puffer systemer havde ikke væsentlig betydning for redox signalerne, men voltammogrammerne var markant afhængige af NaCl, da NaCl havde en dæmpende effekt på redox signalerne af *P. furiosus* ferredoxin.

P. furiosus ferredoxin med den hetormetalliske [$CoFe_3S_4$] klynge blev syntetiseret og oprenset in den oxiderede [$CoFe_3S_4]^{2+}$ tilstand. De kromatografiske, massespektrometriske og EPR spektroskopiske resultater indikerede, at [$CoFe_3S_4$] ferredoxin blev oprenset til høj renhed, og at proteinet var stabilt under de benyttede forhold. Disse resultater er i modstrid med tidligere rapporteret hurtig oxidativ nedbrydning af [$CoFe_3S_4]^{2+}$ ferredoxin til [$Fe_3S_4]^{+}$ ferredoxin. Forsøg med kemisk oxidation of reduktion tydede på et redox aktivt protein, og denne aktivitet blev bekræftet ved cyklisk voltammetri. Et veldefineret sæt af redox-toppe fremkom og blev tilskrevet [$CoFe_3S_4]^{2+/+}$ redox parret og havde et formelt potential ved -177 mV mod SHE.

I modsætning til naturligt forekommende jern-svovl klynger samles molybdæn-svovl klyngen ikke i ferredoxin af sig selv. Molybdæn-svovl analogen syntetiseredes i stedet ved at tilsætte på forhånd fremstillet [$Mo_4S_4(H_2O)_{12}]Cl_5$ til apo-ferredoxin, som var stabiliseret ved sulfonering. Oprensningen af molybdæn-svovl analogen viste to beslægtede specier, hvis indbyrdes mængdeforhold afhang af de eksperimentelle

betingelser. De to specier blev undersøgt ved EPR-monitorerede redox-titreringer og de opnåede EPR spektre blev sammenlignet med spektre målt for $[Mo_4S_4(H_2O)_{12}]^{5+}$. Resultaterne heraf bekræftede indsættelsen af den intakte $[Mo_4S_4]$ klynge og indikerede stabilisering af molybdæn-svovl klyngen i tre oxidationstilstande; 4+, 5+ og 6+ tilstandene. De formelle potentialer for overgangene mellem de tre oxidationstilstande blev bestemt til -195 mV og -295 mV mod SHE for den ene specie og -205 mV og -380 mV mod SHE for den anden specie. Spektre målt efter oxidativ titrering antydede oxidativ nedbrydning af $[Mo_4S_4]$ klyngen. Ud fra EPR spektrene af de to molybdæn-svovl analog specier er det ikke muligt at identificere klyngens ligander, men spektrene indikerer, at de to specier adskiller sig fra hinanden ved at have forskellige ligander på klyngen.

Disse studier har givet væsentlig ny indsigt i disse nye proteiner og har øget forståelsen af ferredoxiner med re-designede aktive centre. Det er derfor et vigtigt skridt på vej til udnyttelse af disse proteiner i nye katalytiske systemer.

List of Abbreviations

Au/mAu	Absorbance units/milli-absorbance units
A	Hyperfine splitting/electrode area
B	Applied external field
CV	Column volume
D. gigas	*Desulfovibrio gigas*
DTT	Dithiothreitol
E^0	Standard electrode potential
$E^{0'}$	Formal potential
ΔE	Peak-peak separation
E_a	Anodic peak potential
E_c	Cathodic peak potential
$E_{p/2}$	Half peak potential
edta/EDTA	Ethylenediaminetetraacetate
EPG	Edge-plane pyrolytic graphite
EPR	Electron paramagnetic resonance
G	Electronic gain
HiPIP	High-potential iron-sulfur protein
HPLC	High perfomance liquid chromatography
I	Nucleus spin
i	EPR intensity
i_a	Anodic peak current
i_c	Cathodic peak current
ICP-MS	Inductively coupled plasma mass spectrometry
j_a	Anodic peak current density
j_c	Cathodic peak current density
k_s	Electron transfer reaction rate constant
LCA	Last common ancestor
M	Modulation amplitude
MWCO	Molecular weight cut off
NTSB	2-nitro-5-thiosulfobenzoate
v	Frequency of radiation/voltammetric scan rate
Ori-ISP	Origin of iron-sulfur proteins

P	Microwave power attenuation
P. furiosus	*Pyrococcus furiosus*
PDB	Protein Data Bank
S	Unpaired electron spin
SHE	Standard hydrogen electrode
SCE	Saturated calomel electrode
T	Temperature
Tris	Tris(hydrodymethyl)-aminoethane
W	Magnetic field scan width
UV-vis	Ultraviolet-visible light

Contents

Chapter One

1 Introduction

The primary focus of this dissertation is the synthesis and characterization of two artificial metalloproteins, the design of which is crucially based on iron-sulfur proteins. Almost one third of naturally occurring proteins contain metal binding sites and many of these have been mimicked in designed metalloproteins. Metalloprotein design provides means for testing and increasing the understanding of the interactions between metal centers and proteins [1]. Furthermore, incorporation of non-natural metal sites in the matrix of proteins has been exploited in the design of new biologically based catalytic systems [2].

This project concerns the design and studies of two artificial proteins where metals other than iron are incorporated in the active site of iron-sulfur proteins. The *Pyrococcus furiosus* ferredoxin is the starting point for both new metalloproteins. In the first new protein cobalt is inserted in the *P. furiosus* ferredoxin iron-sulfur cluster, thereby creating a heterometallic cobalt-iron-sulfur cluster. The second protein is designed by substituting the iron-sulfur cluster with a molybdenum-sulfur cluster. Both proteins are interesting for design of new catalytic systems.

The design of iron-sulfur proteins with synthetic heterometallic clusters is inspired by enzymes with heterometallic sites catalyzing biological processes involving uptake or formation of gasses such as H_2, CO_2 and N_2 [3]. The potential of heterometallic clusters to participate in enzymatic catalysis has stimulated the design of novel heterometallic clusters in iron-sulfur proteins to increase the understanding of natural iron-sulfur clusters and heterometallic clusters [4] as well as design of new catalytic systems [3].

Synthetic molybdenum-sulfur clusters have attracted interest due to their reactivity and catalytic activity in industrial hydrogenation and dehydrogenation processes. In addition they have structural similarities to the cuboidal clusters in iron-sulfur proteins [5]. This makes them intriguing candidates for incorporation in iron-sulfur proteins. Design of molybdenum-sulfur analogues of iron-sulfur proteins holds potential both to provide new fundamental understanding of iron-sulfur proteins and in the design of new catalytic systems based on the properties of molybdenum-sulfur clusters.

This thesis presents the preparation and characterization of these two novel designed proteins as well as a multitude of studies of *P. furiosus* ferredoxin serving as reference for the characterization of the cobalt-iron-sulfur and the molybdenum-sulfur proteins.

1.1 Outline of the thesis

Iron-sulfur proteins are the basis for the work in this project. They are encountered in all life forms and are essential in a range of biological reactions. In spite of simple and structurally similar metal centers, the proteins display a remarkable functional diversity. Chapter 2 introduces the iron-sulfur protein class and particularly the target *P. furiosus* ferredoxin in this project. This chapter also briefly presents the ferredoxins with synthetic, heterometallic clusters. The molybdenum-sulfur clusters relevant for this project are introduced in Chapter 3. This chapter offers a comparison of the molybdenum-sulfur and iron-sulfur clusters and a more detailed description of the potential of substituting an iron-sulfur cluster with a molybdenum-sulfur cluster. Chapter 4 presents cyclic voltammetry and EPR spectroscopy as the main characterization methods used in this project as well as the equipment used in the experimental work.

The experimental work is described in Chapters 5 to 9. Chapter 5 describes the studies of iron-sulfur proteins that serve as a reference for the studies of the two artificial proteins. The purification of *P. furiosus* ferredoxin is first briefly presented. The electrochemical studies of the two forms of the *P. furiosus* ferredoxin are then described in some detail along with the electrochemical studies of ancient ferredoxins. The synthesis, purification and multidisciplinary characterization of the artificial [$CoFe_3S_4$] ferredoxin are described in Chapter 6. Chapter 7 presents the sulfonation of *P. furiosus* ferredoxin which is an intermediate step on the way to the incorporation of the molybdenum-sulfur cluster. The synthesis of the aqueous complex of the molybdenum-sulfur cluster is described in Chapter 8 in which the EPR spectroscopic characterization that serves as a reference for the characterization of the molybdenum-sulfur analogue of *P. furiosus* ferredoxin is also presented. Chapter 9 describes the studies of the molybdenum sulfur analogue, including the synthesis, purification and EPR spectroscopic analysis.

The thesis is concluded in Chapter 10 with a summary of the results of the experimental work and an outlook to further studies based on this work.

Chapter Two

2 Iron-Sulfur Proteins

2.1 Introduction

Iron-sulfur proteins have attracted much attention due to their ubiquitous distribution in nature, high functional diversity and vital importance in all life forms. They were first discovered in the mid-1960s. Since then, a wide range of techniques have been used to image in great detail the structural, chemical and magnetic properties of iron-sulfur clusters. [6]

2.2 Iron-sulfur clusters

With the exception of rubredoxin the core groups of all iron-sulfur proteins are clusters of iron ions and inorganic acid-labile sulfide most often linked to the protein by cysteine ligands [7]. Iron-sulfur clusters can contain between one and up to eight iron atoms. Some proteins contain multiple clusters [8]. The most common and earliest discovered clusters are the $[Fe_2S_2]$, $[Fe_3S_4]$ and $[Fe_4S_4]$ clusters [9], Figure 2.1. More complex clusters have also been discovered [10]. The $[Fe_2S_2]$ and $[Fe_4S_4]$ clusters are readily formed by self-assembly in apo-proteins. A variety of synthetic analogues of the clusters have also been designed and prepared [8].

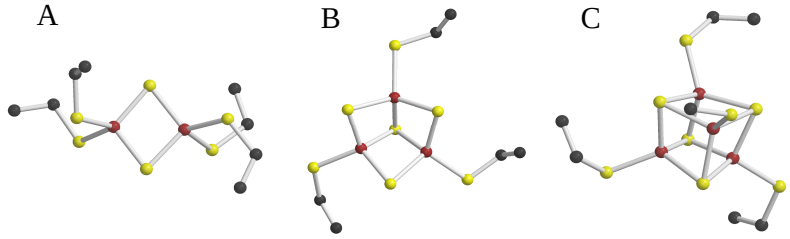

Figure 2.1: The common iron-sulfur clusters and the coordinating cysteines. A) $[Fe_2S_4]$, B) $[Fe_3S_4]$, and C) $[Fe_4S_4]$. Color code: Red = iron, yellow = sulfur, black = carbon. One of the cysteines in C is only marked with a sulfur atom for clarity.

In all these clusters, each iron atom is surrounded by four sulfur atoms in a distorted tetrahedral coordination. This is notably different from the usual characteristic octahedral coordination sphere of iron. This untypical arrangement is enforced by the steric requirements of the large sulfur atoms. An important consequence of this is that iron atoms in these clusters always occur in the high-spin configuration (cf. section 2.7) [11]. Iron-sulfur clusters are highly sensitive towards oxygen, the stability depending on the protein. Some iron-sulfur proteins are stable in air for weeks while

others lose the cluster in less than a second [6]. Below we focus on proteins containing the cuboidal [Fe_4S_4] cluster and the incomplete cuboidal [Fe_3S_4] cluster which are the core proteins of the project.

2.3 Biological functions of [Fe_3S_4] and [Fe_4S_4] clusters

The cuboidal iron-sulfur clusters are highly versatile and involved in various types of essential biological reactions among which electron transfer is the most common function [9]. Electron transfer is the key function of the ferredoxin and high-potential iron-sulfur protein (HiPIP) families, particularly as part of anaerobic bacterial metabolism [7]. Ferredoxins can contain one or two [Fe_3S_4] or [Fe_4S_4] clusters and have been isolated from all hydrogen-consuming or –producing organisms, including anaerobic and aerobic photosynthetic bacteria as well as (hyper-)thermophilic bacteria and extremophilic archaea [7, 9]. Non-ligating cysteines form a disulfide bond in many monocluster ferredoxins that can participate in the redox cycle in the protein. HiPIPs contain a single [Fe_4S_4] cluster and have mostly, but not exclusively, been isolated from photosynthetic bacteria [9]. HiPIPs have been proven to be involved in electron transfer in photosynthetic bacteria, but their role in non-photosynthetic organism is still unknown [6]. Many cuboidal iron-sulfur clusters in redox enzymes also have electron transfer functions [9]. The differences between ferredoxins and HiPIPs will be described in more detail in section 2.6.

In addition to the established role of iron-sulfur clusters in electron transfer, cuboidal iron-sulfur clusters are a critical part of the active site in a plethora of catalytic enzymes where they have key functions in substrate binding, both redox and non-redox catalysis, redox-mediated generation of free radicals, and stabilization of intermediates. Clusters in other proteins are essential for regulation and sensing functions related to oxygen and iron [9].

2.4 Evolution of iron-sulfur proteins

The ubiquitous occurrence of iron-sulfur proteins, especially their presence in ancient organisms has led to the idea that iron-sulfur proteins are very old proteins emerging in the early stages of evolution [7]. This hypothesis has been supported broadly by the functional diversity of iron-sulfur clusters [6]. The structural similarities between ferredoxins containing cuboidal clusters thus suggest that these proteins share an evolutionary common ancestor. According to a prevalent model, this ancestor is a simple two [Fe_4S_4] cluster ferredoxin [12]. Other ferredoxins subsequently evolved through N- and C-terminal extensions, abstraction of an iron atom or loss of one of the cluster which in some cases resulted in the formation of a disulfide bond between remaining cysteine residues [6, 12]. Other iron-sulfur proteins may also have evolved in an early stage of evolution and still others may be adaptions of already existing proteins folds to host an iron-sulfur cluster in the active site [6].

Recent theories [13, 14] on the origin of life suggest a start near hydrothermal vents on pyrite, FeS_2, surfaces. According to these theories, the iron-sulfur structures in

pyrite catalyzed reactions from simple inorganic compounds such as H_2S, CO/CO_2 and H_2O first leading to simple organic compounds which subsequently were precursors for more complex polymers such as proteins and nucleic acids [13, 14]. An interesting feature of pyrite is the presence of $[Fe_2S_2]$ and $[Fe_4S_4]$ sites, suggested to be precursors for the iron-sulfur clusters in iron-sulfur proteins [14]. The family of ferredoxins containing two $[Fe_4S_4]$ clusters has been suggested to be the extant remnants of this process [6].

2.5 $[Fe_3S_4]$ and $[Fe_4S_4]$ cluster interconversion

The interconversion of $[Fe_4S_4]$ and $[Fe_3S_4]$ clusters by uptake or removal of an iron ion is a well-known phenomenon and represents one of the most common reactions of protein bound iron-sulfur clusters. Oxidative removal of an iron ion from $[Fe_4S_4]^{2+}$ often observed during aerobic purification of iron-sulfur proteins [9] is just one among many examples.

The $[Fe_3S_4]$ and $[Fe_4S_4]$ clusters are interconvertible in ferredoxin with only a single cluster [7]. Not all $[Fe_3S_4]$-containing proteins can incorporate an additional Fe-atom, and the proteins vary in ease and rapidity of interconversion [15]. The ease of inter-conversion seems to be related to the presence of a non-thiol (non-cysteine) ligand. However, other factors are also involved since proteins with $[Fe_3S_4]$-clusters that do not convert to $[Fe_4S_4]$-clusters even in the presence of four available cysteine ligands are known [15]. The biological significance of the $[Fe_3S_4]$ cluster in ferredoxins is under discussion [7]. The cluster conversion could be a controlling mechanism since different structures and activities have been determined for the $[Fe_4S_4]$ and $[Fe_3S_4]$ forms of *Desulfovibrio gigas* (*D. gigas*) ferredoxin. The $[Fe_4S_4]$ form is dimeric and the more efficient form for coupling pyruvate dehydrogenase activity to H_2 evolution, whereas the $[Fe_3S_4]$ is tetrameric and more efficient coupling H_2 consumption to sulfite reduction [9].

The conversion between the $[Fe_3S_4]$ and $[Fe_4S_4]$ forms is also crucial for the activity of certain iron-sulfur enzymes. Aconitase and S-adenosylmethionine (AdoMet)-dependent class III ribonucleotide reductase (RNR III) are enzymes that undergo interconversions between $[Fe_3S_4]$ and $[Fe_4S_4]$. The $[Fe_4S_4]$ cluster is contained in the active form of both enzymes, but the cluster is converted to $[Fe_3S_4]$ upon exposure to oxygen, and the mechanism is believed to have an oxygen sensing function in the proteins. Aconitase is re-activated in the presence of Fe^{2+} under reducing conditions, while exogenous iron is not required for regeneration of the $[Fe_4S_4]$ cluster in the AdoMet-dependent RNR III [9, 16, 17].

2.6 Redox properties of Fe_3S_4 and Fe_4S_4 containing proteins

The redox potentials of the cuboidal iron-sulfur clusters in electron transfer proteins versus a standard hydrogen electrode (SHE) are given in Figure 2.2. The redox potentials differ by more than 1 V and vary remarkably even within the same family of proteins. The potentials of the redox couples in model compounds are significantly

lower than in proteins [9]. The diversity of the redox chemistry of iron-sulfur proteins is all based on the ability of the surrounding protein to regulate the Fe^{2+}/Fe^{3+} redox couple [9].

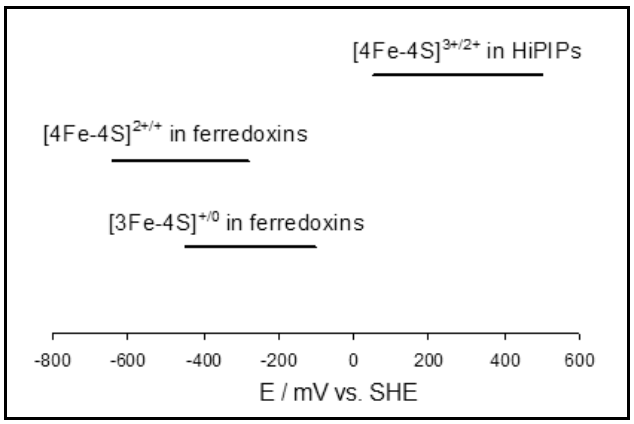

Figure 2.2: Redox potentials vs. SHE of cuboidal iron-sulfur clusters in electron transfer proteins [9].

As noted, the $[Fe_4S_4]$ cluster is the core cluster in both ferredoxins and in HiPIPs. The clusters in the two types of iron-sulfur proteins are structurally very similar, but the redox properties are remarkably different [18]. The redox potentials of the $[Fe_4S_4]$-cluster in ferredoxins show a range of -650 to -280 mV vs. SHE, while potentials in HiPIPs range from 90 to 500 mV vs. SHE [9]. This has been described by Carter et al. as the "three-state hypothesis" [18]. According to this model different oxidation states are stabilized in $[Fe_4S_4]$ ferredoxin and HiPIPs, cf. below. Ferredoxins stabilize the $[Fe_4S_4]^{2+}$ and $[Fe_4S_4]^{+}$ states [12] whereas HiPIPs cycle between the $[Fe_4S_4]^{3+}$ and $[Fe_4S_4]^{2+}$ states [20], Figure 2.3. Only these states are physiologically relevant [11].

$$\underset{\text{ferredoxins}}{[Fe_4S_4]^{+} \underset{e^-}{\rightleftharpoons} [Fe_4S_4]^{2+}} \quad \underset{\text{HiPIPs}}{\underset{e^-}{\rightleftharpoons} [Fe_4S_4]^{3+}}$$

Figure 2.3: The redox states of the [4Fe-4S]-cluster in ferredoxins and HiPIPs.

It is still unclear which factors determine the available oxidations states of the cluster. Several suggestions have been forwarded. These include hydrogen bonding to the cluster, solvent access to the cluster, covalency of Fe-S bonds, number and position of hydrophobic residues surrounding the cluster, and electrostatic effects of the protein backbone [21]. Ferredoxins have more NH-S hydrogen bonds to the inorganic cluster sulfur atoms than HiPIPs. The hydrogen bonds may stabilize the more reduced states in ferredoxins [20]. The protein bound cluster has an overall negative charge since each cysteine contributes with a charge of -1. The hydrogen bonds stabilize the more negatively charged reduced cluster. A larger number of hydrophobic amino acids surround the cluster in HiPIPs and thus diminishes the solvent access. This might stabilize the higher oxidation states in HiPIPs [11, 21], since access of water leads to increased hydrogen bonding and polarity [21, 22]. It has been suggested that the number of partial positive charges arising from backbone amide group dipoles can

explain the redox differences between ferredoxins and HiPIPs because the polar groups also interact with the charged cluster. Ferredoxins contain more of these than HiPIPs [23]. It is likely that a combination of various effects determines the biologically available cluster states and potentials.

Other states can be obtained under non-physiological conditions. A $[Fe_4S_4]^0$ cluster has been identified in the ferredoxin-like Fe-protein in *Azotobacter vinelandii* nitrogenase [24] and in the activator of 2-hydroxyglutaryl-CoA dehydratase from *Acidaminococcus fermentans* [25]. Both proteins are known to cycle between the $[Fe_4S_4]^{2+}$ and $[Fe_4S_4]^{+}$ states. These are the only known iron-sulfur proteins in which the same cluster has been stabilized in three different oxidation states [24, 25].

2.7 Electronic and magnetic properties of Fe_3S_4 and Fe_4S_4 clusters

As noted iron is tetrahedrally coordinated in iron-sulfur proteins and the iron atoms are in the high spin configuration [11]. Each iron ion is either in the +2 or the +3 oxidation state with spins $S = 2$ and $S = 5/2$, respectively [9].

Iron-sulfur clusters that contain both Fe^{2+} and Fe^{3+} can form delocalized $Fe^{2.5+}$-$Fe^{2.5+}$ pairs with a total spin of $S = 9/2$. All the biologically relevant states of the $[Fe_4S_4]$ cluster have at least one of these pairs. The $[Fe_4S_4]^{2+}$ cluster have two such pairs that are anti-ferromagnetically coupled to give a total spin of $S = 0$ and a diamagnetic cluster. The $[Fe_4S_4]^{+}$ cluster has one $Fe^{2.5}$-$Fe^{2.5}$ pair coupled anti-ferromagnetically to a Fe^{2+}-Fe^{2+} pair ($S = 4$) giving a total spin of $S = ½$. The delocalized pair in the $[Fe_4S_4]^{3+}$ cluster is coupled to a Fe^{3+}-Fe^{3+} pair also giving a total spin $S = ½$. The $[Fe_3S_4]^0$ cluster contains one $Fe^{2.5+}$-$Fe^{2.5+}$ pair coupled anti-ferromagnetically to an Fe^{3+} [8]. It is noteworthy that the $[Fe_4S_4]^{2+}$ in both HiPIPs and ferredoxins has a zero net spin and possible differences in the two protein families can therefore not be studied with EPR spectroscopy. Table 2.1 gives an overview of the spin states of the iron-sulfur clusters.

Table 2.1: Spin states and coupling in iron-sulfur clusters.

Cluster	Individual spins	Coupling	Total spin
$[Fe_3S_4]^0$	2, 5/2, 5/2	$Fe^{2.5+}$-$Fe^{2.5+}$ coupled to Fe^{3+}.	2
$[Fe_3S_4]^+$	5/2, 5/2, 5/2	Fe^{3+}-Fe^{3+} coupled to Fe^{3+}	½
$[Fe_4S_4]^+$	2, 2, 2, 5/2	$Fe^{2.5+}$-$Fe^{2.5+}$ coupled to Fe^{2+}-Fe^{2+}	½
$[Fe_4S_4]^{2+}$	2, 2, 5/2, 5/2	2 $Fe^{2.5+}$-$Fe^{2.5+}$ pairs	0
$[Fe_4S_4]^{3+}$	2, 5/2, 5/2, 5/2	$Fe^{2.5+}$-$Fe^{2.5+}$ coupled to Fe^{3+}-Fe^{3+}	½

2.8 *Pyrococcus furiosus* ferredoxin

P. furiosus is a hyperthermophilic, anaerobic archeaon that has a growth optimum at 100 °C isolated from submarine volcanic areas [26]. A single ferredoxin has been isolated and was one of the first proteins isolated from this organism [27]. The

ferredoxin shuffles electrons in the organism's hydrogen metabolism, where it is an electron acceptor for glyceraldehyde-3-phosphate oxidoreductase and pyrovate oxidoreductase and an electron donor for a membrane-bound hydrogenase complex and sulfide dehydrogenase [28].

P. furiosus ferredoxin is a small protein and contains 66 amino acids and one $[Fe_4S_4]$ cluster in monomeric form. One of the iron atoms of the cluster is coordinated to the protein through aspartate instead of the usual cysteine ligation [29] making it one of only two ferredoxin containing a single $[Fe_4S_4]$ cluster with this coordination [30]. Aspartate coordination has been found in other ferredoxins containing two $[Fe_4S_4]$ clusters [29]. The $[Fe_4S_4]$ degrades to $[Fe_3S_4]$ upon exposure to oxidizing conditions, the labile iron being the one coordinated to aspartate. [29]. The ferredoxin has a very high thermostability with unchanged activity and UV-visible absorption after incubation even at 95 °C for 12 hours under anaerobic conditions [27]. The protein has an overall high negative charge (-13/-14 depending on the redox state of the $[Fe_4S_4]$ cluster) and a disulfide bridge [12].

P. furiosus ferredoxin was reported to exist as a monomer in early studies [29]. It has later been suggested that a monomer/dimer equilibrium exists depending on the ionic strength and that the protein is a dimer at physiological ionic strength [31]. The crystal structures have been solved for both the native protein containing a $[Fe_3S_4]$ cluster [30] and for the $[Fe_4S_4]$ mutant where the ligating aspatate has been exchanged with a cysteine ligand [32], Figure 2.4. In the $[Fe_3S_4]$ ferredoxin structure, the cluster is shielded from direct solvent interactions by the protein backbone and the non-ligating aspartate is located close to the missing iron so that it easily can switch to coordinate a fourth iron. The structure disclosed possible dimerization sites [30]. The crystal structure of the native $[Fe_4S_4]$ *P. furiosus* ferredoxin has yet to be solved.

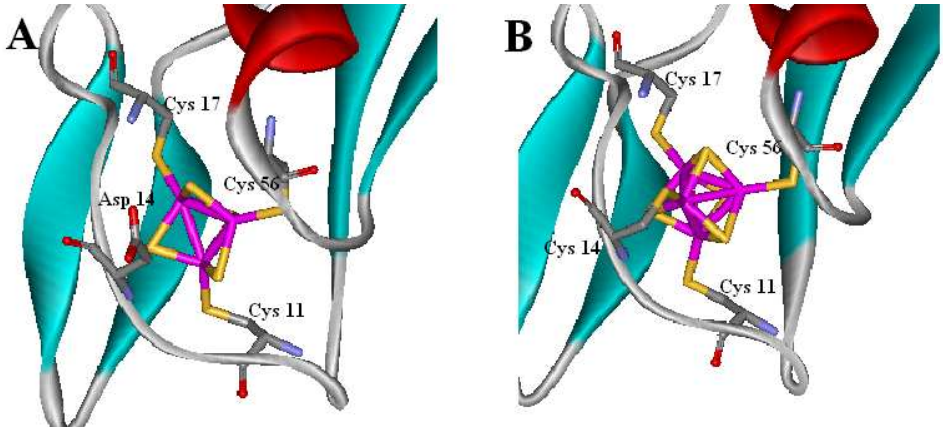

Figure 2.4: Close-up illustrations of the structures surrounding the clusters in A) the native protein with $[Fe_3S_4]$ (PDB ID: 1SJ1 [30]), and B) the D14C mutant with $[Fe_4S_4]$ (PDB ID: 2Z8Q [32]). The figures were prepared with ViewerLite [33].

EPR spectroscopy has shown that the reduced $[Fe_4S_4]^+$ ferredoxin exist in a spin mixture of $S = 1/2$ and $S = 3/2$. S = 1/2 is normal for $[Fe_4S_4]$ ferredoxins, though the signal is remarkably broad. The $S = 3/2$ resonance is unusual, but has been observed in multiple iron-sulfur proteins [29]. The ratio of $S = 3/2$ over $S = 1/2$ species has been

shown to depend on ionic strength and $S = 3/2$ was assigned to the dimeric form and $S = 1/2$ to the monomer [31].

2.9 Incorporation of exogenous metals in *P. furiosus* ferredoxin

Enzymes catalyzing biological reactions involving gasses like N_2, H_2, CO, CO_2 and CH_4 have been found to involve iron-sulfur based clusters, in most cases in assemblies with other metals such as nickel and molybdenum [3]. For example, nickel-iron hydrogenases catalyze formation or cleavage of H_2 at a Ni-Fe center [34], CO is generated from CO_2 at a distorted cuboidal nickel-iron-sulfur cluster in CO dehydrogenases [35], and a complex molybdenum-iron-sulfur cluster in nitrogenases catalyze reduction of N_2 to NH_3 [36]. These reactions are interesting both in fundamental research on the origin of life and for technical applications due to the environmental and industrial importance of these gasses and processes [3].

The potential of heterometallic centres to participate in enzymatic catalysis has stimulated synthesis and characterization of novel, artificial heterometallic clusters inserted in proteins [4]. The facility of $[Fe_3S_4]/[Fe_4S_4]$ interconversions has further suggested that exogenous metals can be incorporated into the vacant sites of the $[Fe_3S_4]$ cluster. This has led to the generation of a novel whole class of clusters [37].

The first reported formation of a heterometallic cluster in a protein was the formation of a $[CoFe_3S_4]$ cluster in *D. gigas* ferredoxin II in 1986 [37]. Since, proteins suitable for incorporation have been extended to include *P. furiosus* ferredoxin and *D. africanus* ferredoxin and also aconitase [4].

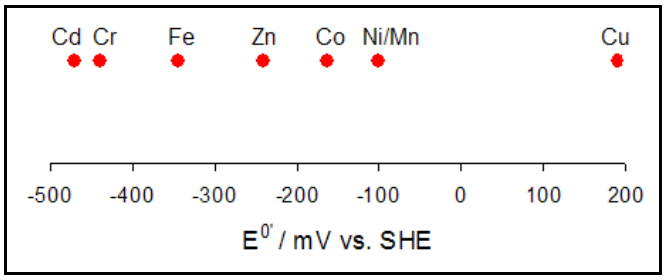

Figure 2.5: Plot of redox potentials of $[M\text{-}3Fe\text{-}4S]^{2+/+}$ in *P. furiosus* Ferredoxin for different heterometals, M [data from 38, 39].

A range of metals have been incorporated in *P. furiosus* ferredoxin including monovalent, trivalent and divalent metal ions [4]. Most reports have focused on the incorporation of divalent metal ions in $[Fe_3S_4]^0$ under reducing conditions to yield $[MFe_3S_4]^+$-clusters (M = Zn^{2+}, Ni^{2+}, Co^{2+}, Mn^{2+}, Cd^{2+}, Cu^{2+} and Cr^{2+}) [38, 39, 40]. These clusters are redox active and undergo $[MFe_3S_4]^{2+/+}$ transformations [38, 39]. The redox potentials are displayed in Figure 2.5. Johnson et. al. have suggested that the heterometallic clusters can be rationalized as a cluster fragment, $[Fe_3S_4]^{0/-1}$ ($S = 2/S = 5/2$), coupled antiferromagnetically to the metal ion, M^{2+}, the redox chemistry being confined in the cluster fragment [38, 39]. The clusters with potentials higher than $[ZnFe_3S_4]$ have heterometals with accessible $M^{2+/+}$ couples in the physiological potential range and show a tendency to withdraw electrons from the $[Fe_3S_4]$-fragment,

reduced $[Fe_3S_4]^0$ state easier accessible. In comparison the heterometals in the clusters with potentials lower than $[ZnFe_3S_4]$ have accessible $M^{3+/2+}$ couples in the physiological potential range and donates electrons to the $[Fe_3S_4]$-fragment, making the reduced state harder to access [39].

CHAPTER THREE

3 Molydenum-Sulfur Analogues of Iron-Sulfur Proteins

3.1 Introduction

Like iron, molybdenum forms cuboidal clusters with sulfur donor. As noted in chapter 2.1, the cuboidal iron-sulfur [Fe_4S_4] clusters occur ubiquitously in natural proteins. On the other hand, the molybdenum-sulfur analogue [Mo_4S_4] does not occur naturally, but complexes with the cuboidal molybdenum-sulfur core can be synthesized.

The similarities and differences between the two clusters are described in this chapter and make the [Mo_4S_4] cluster an attractive candidate as an alternative for the [Fe_4S_4] clusters in iron-sulfur proteins. In view of the uniquely efficient catalysis of both iron-sulfur and molybdenum-sulfur clusters in redox catalysis as well as in industrial catalysis, this approach offers interesting perspectives in fundamental understanding of protein-cluster interactions as well as design of new catalytic systems.

3.2 Molybdenum-sulfur clusters

The structure of the cuboidal [Mo_4S_4] cluster and the incomplete cuboidal [Mo_3S_4] cluster are shown schematically in Figure 3.1. The aqua complexes, $[Mo_4S_4(H_2O)_{12}]^{n+}$ and $[Mo_3S_4(H_2O)_9]^{m+}$, can be prepared in aqueous solution [5]. Molybdenum-sulfur clusters have attracted attention due to their ability to catalyze in hydrogenation, hydrodesulforization and hydrogen evolution [41, 42].

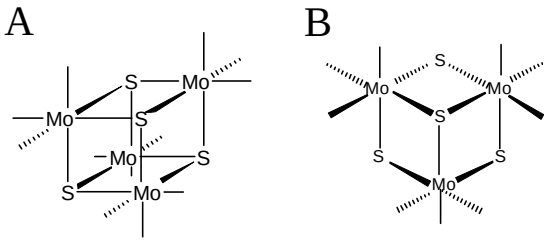

Figure 3.1: Schematic drawings of A) the cuboidal [Mo_4S_4] cluster, and B) the incomplete cuboidal [Mo_3S_4] cluster. Aqua ligands are omitted for clarity.

The cuboidal cluster is a distorted cube consisting of two interpenetrating tetrahedra of Mo_4 and S_4 of different dimensions [5]. On mild oxidation, such as exposure to air, one of the molybdenum ions is lost from the [Mo_4S_4] cluster to give the incomplete cuboidal [Mo_3S_4] cluster [43]. The trinuclear complex can be stored for years in air in

acidic solutions with $[H^+] > 0.3$ M [5].

$[Mo_3S_4(H_2O)_9]^{4+}$ is capable of incorporating transition and post-transition metals to give $[MMo_3S_4]$, Figure 3.2A. Both tetrahedrally and octahedrally coordinating metals have been incorporated. In many cases, metallic M^0 can be used as the source of M leading to $[MMo_3S_4]^{4+}$ clusters [5]. Some heterometals give only single cuboidal clusters. The clusters incorporating tetrahedrally coordinating metals, like Co, also give edge-linked double-cuboidal clusters, Figure 3.2B, while corner-shared double-cuboidal clusters are obtained with octahedrally coordinating heterometals Figure 3.2C [5]. Interesting catalytic properties have been reported for multiple $[MMo_3S_4]$ clusters. For example, $[PdMo_3S_4]$ cores catalyze reaction of alkynes with methanol or carboxylic acids and $[NiMo_3S_4]$ is an efficient catalyst in hydrodesulfurization [41].

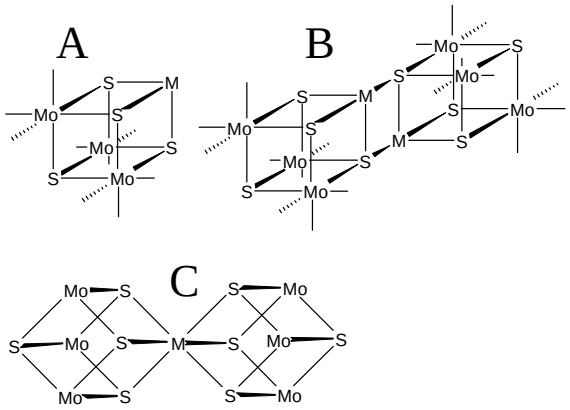

Figure 3.2: Schematic drawings of heterometallic A) single cuboidal cluster, B) edge-linked double-cuboidal cluster, and C) corner-shared double-cuboidal cluster. Aqua ligands are omitted for clarity.

3.3 Redox, magnetic and electronic properties of $[Mo_4S_4]$ clusters

The green $[Mo_4S_4]^{5+}$ is most readily prepared in aqueous solution, but two additional oxidation states, the orange, reduced $[Mo_4S_4]^{4+}$ and the red, oxidized $[Mo_4S_4]^{6+}$, can also be obtained, Figure 3.3 [5].

$$[Mo_4S_4]^{4+} \underset{e^-}{\rightleftharpoons} [Mo_4S_4]^{5+} \underset{e^-}{\rightleftharpoons} [Mo_4S_4]^{6+}$$

Figure 3.3: The redox states of $[Mo_4S_4]$ clusters in aqueous solution.

Cyclic voltammetry of the cluster with aqua ligands gives two redox-couples at 0.227 V and 0.900 V versus SHE. The corresponding ethylenediaminetetraacetate (edta) complexes $[Mo_4S_4(edta)_2]^{2-/3-/4-}$ give two redox couples at significantly lower potentials (-0.11 V and 0.59 V versus SHE) [44].

All the Mo atoms in $[Mo_4S_4]^{4+}$ are in the Mo^{III} oxidation state, while the $[Mo_4S_4]^{5+}$ and $[Mo_4S_4]^{6+}$ are mixed-valence states, formally $Mo^{III}_3Mo^{IV}$ and $Mo^{II}_2Mo^{IV}_2$ [45].

The number of available 4d-electrons in the $[Mo_4S_4]^{4+}$, $[Mo_4S_4]^{5+}$ and $[Mo_4S_4]^{6+}$ states are 12, 11 and 10, respectively. It has been found that the $[Mo_4S_4]^{4+}$ and $[Mo_4S_4]^{6+}$ states are diamagnetic, while the $[Mo_4S_4]^{5+}$ state is paramagnetic with S = ½ [46]. The magnetism for iron-sulfur clusters can be explained ferromagnetic and antiferro-

magnetic interactions, but this approach is not suitable for the molybdenum-sulfur clusters. The magnetism of these clusters is better explained by molecular orbital models [47], such as the molecular orbital model suggested by Shibahara et. al. [44].

3.4 Comparison of the $[Fe_4S_4]$ and $[Mo_4S_4]$ Clusters

Structural parameters of the $[Fe_4S_4]$ and $[Mo_4S_4]$ clusters are given in Table 3.1. As can be seen from the table, the sizes of the two cluster types are very similar. The molybdenum-sulfur clusters are, however, a little larger than the iron-sulfur clusters. The bond lengths in both types of clusters depend only very slightly on the oxidation state of the cluster.

Table 3.1: Bond lengths in $[Fe_4S_4]$ and $[Mo_4S_4]$ clusters. All bond lengths are given in Å.

Cluster	M-M	M-S(cluster)	M-S(cys) /ligand	ref.
$[4Fe\text{-}4S]^{3+}$ in $(Bu_4N)[Fe_4S_4(S\text{-}2,4,6\text{-}(i\text{-}Pr)_3C_6H_2)_4]$	av. 2.74	2.23-2.28	2.20-2.21	49
$[4Fe\text{-}4S]^{2+}$ in $(PPh_4)_2[Fe_4S_4(SH)_4]$	2.74-2.77	2.27-2.30	2.25-2.27	50
$[4Fe\text{-}4S]^{2+}$ in $(Et_4N)_2[Fe_4S_4(SCH_2Ph)_4]$	2.73-2.78	2.23-2.32	2.24-2.26	51
$[4Fe\text{-}4S]^{+}$ in $(Et_4N)_3[Fe_4S_4(SH)_4]$	2.76	2.31	2.32	52
$[4Fe\text{-}4S]^{+}$ in $(Et_4N)_3[Fe_4S_4(SCH_2Ph)_4]$	2.71-2.78	2.30-2.33	2.28-2.30	53
$[4Mo\text{-}4S]^{6+}$ in $Na_2[Mo_4S_4(edta)_2]\cdot 6H_2O$	2.74-2.87	2.32-2.39	2.08-2.28	44
$[4Mo\text{-}4S]^{5+}$ in $[Mo_4S_4(H_2O)_{12}](PTS)_5\cdot 14H_2O$*	2.79-2.83	2.34-2.36	2.17-2.21	44
$[4Mo\text{-}4S]^{4+}$ in $[Mo_4S_4(NH_3)_{12}]Cl_4\cdot 7H_2O$	2.79-2.81	2.36-2.37	2.28-2.31	44

*) PTS = paratoluenesulfonic acid.

Despite the similar cluster sizes there are also some notable structural differences. Iron is almost always tetrahedrally coordinated in iron-sulfur clusters, although iron normally has octahedral coordination spheres [48]. Molybdenum has a distorted octahedral coordination in molybdenum-sulfur cluster complexes. Iron thus holds a coordination number of four, while the coordination number of molybdenum is six.

The $[Fe_4S_4]$ clusters are formed by "self-assembly" in proteins or *in vitro*, and can easily be synthesized in the presence of Fe^{2+}/Fe^{3+}-ions, sulfide and apo-protein or thiolates [46]. The synthesis of $[Mo_4S_4]$ clusters, on the other hand, involves multiple steps [54, 55]. This is to some extent explained by the different starting ions in aqueous solution. Iron is present as $[Fe(H_2O)_6]^{2+}$ or $[Fe(H_2O)_6]^{3+}$ with labile aqua ligands, whereas the prevalent molybdenum species is the very stable MoO_4^{2-} with not easily exchangeable ligands [48].

The most common oxidation states for the $[Fe_4S_4]$ cluster are the three $[Fe_4S_4]^{3+/2+/+}$ states. $[Mo_4S_4]$ can also exist in three oxidation states, namely $[Mo_4S_4]^{6+/5+/4+}$. The charges are thus higher for the cuboidal molybdenum-sulfur clusters. Both the

$[Mo_4S_4]$ and $[Fe_4S_4]$ clusters appear in both paramagnetic and diamagnetic states. $[Mo_4S_4]^{5+}$ is paramagnetic, whereas $[Mo_4S_4]^{4+}$and $[Mo_4S_4]^{6+}$ are diamagnetic. The opposite scheme appears for the iron-sulfur-cluster where $[Fe_4S_4]^{2+}$ is diamagnetic and $[Fe_4S_4]^{+}$ and $[Fe_4S_4]^{3+}$ are paramagnetic. This is summarized in Table 3.2.

Table 3.2 The magnetic states of $[Mo_4S_4]$ and $[Fe_4S_4]$ clusters.

$[Mo_4S_4]^{4+}$ diamagnetic	$[Mo_4S_4]^{5+}$ paramagnetic	$[Mo_4S_4]^{6+}$ diamagnetic
paramagnetic $[Fe_4S_4]^{+}$	diamagnetic $[Fe_4S_4]^{2+}$	paramagnetic $[Fe_4S_4]^{3+}$

Both clusters can be converted to incomplete cuboidal clusters, $[M_3S_4]$ where M = Fe or Mo. The incomplete cuboidal clusters are capable of incorporating exogenous metals to form heterometallic $[M'M_3S_4]$ clusters where M' is the exogenous metal.

3.5 Potential of incorporation of $[Mo_4S_4]$ clusters in iron-sulfur Proteins

The similarities and differences between the $[Fe_4S_4]$ and $[Mo_4S]$ clusters makes $[Mo_4S_4]$ clusters interesting candidates for substituting $[Fe_4S_4]$ clusters in iron-sulfur proteins.

First of all, the similar sizes of the two cluster types suggest that the $[Mo_4S_4]$-cluster can be incorporated. Ferredoxins especially are attractive for cluster substitution, since the protein structure is highly flexible (see chapter 2.6). The cluster is located near the protein surface and is exposed to the solvent. In addition, the cluster undergoes interconversion to $[Fe_3S_4]$ and, as noted, exogenous metals can be incorporated in some ferredoxins (chapter 2.9).

Ferredoxins stabilize the lower charges on $[Fe_4S_4]$ cluster, whereas HiPIPs stabilize the higher charges. It is therefore interesting to investigate which oxidation states of $[Mo_4S_4]$ are stabilized in ferredoxins and HiPIPs, respectively. This might disclose important new information on how the protein affects the cluster.

The $[Fe_4S_4]^{2+}$ cluster is the intermediate redox state which appears in both ferredoxins and HiPIPs is diamagnetic and gives no electron paramagnetic resonance (EPR) signal. In contrast, the intermediate molybdenum-sulfur cluster, $[Mo_4S_4]^{5+}$, is paramagnetic and can be studied by EPR spectroscopy. It will therefore be possible to investigate the intermediate state of the molybdenum-sulfur clusters which suggestively appears in both ferredoxin and HiPIP analogues using this technique. This can potentially give new insight into the interactions between the cluster and the protein.

Another interesting feature is the difference in coordination numbers. As noted, molybdenum is octahedral in $[Mo_4S_4]$ clusters with two extra coordination sites per metal compared to iron in the corresponding $[Fe_4S_4]$ clusters. If this coordination geometry is maintained upon incorporation, and the cluster binding is analogous to the $[Fe_4S_4]$ cluster, two extra coordination sites will therefore be present on each molyb-

denum atom. These eight extra sites hold potential for applications in catalysis.

CHAPTER FOUR

4 Introduction to the Experimental Section

4.1 Cyclic voltammetry

4.1.1 Introduction

Voltammetry is an electrochemical method based on measurement of current as a function of potential applied to an electrode versus a fixed reference electrode potential. In cyclic voltammetry the applied potential is increased or decreased linearly as a function of time to a maximum or minimum, E_2, and then decreased or increased back in a reverse scan to the original value, E_1, Figure 4.1. The slope, i.e. the scan rate, is constant. The current is recorded as a function of time and thus as a function of the applied potential [56].

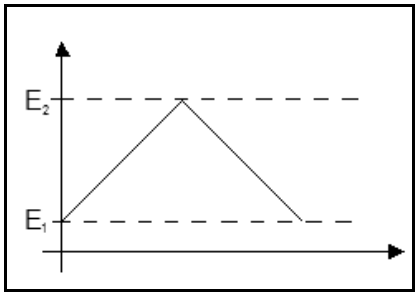

Figure 4.1: Variation of the applied potential with time in cyclic voltammetry.

Cyclic voltammetry is an important diagnostic tool, that provides information about intrinsic properties of a redox system, particularly the formal equilibrium potential $E^{0'}$, and about the kinetics and mechanisms of oxidation and reduction under various conditions [56]. Cyclic voltammetry can be carried out either on electro-active molecules in solution or electro-active molecules adsorbed in a thin layer on an electrode surface. This project focuses on cyclic voltammetry of electro-active molecules in homogeneous solutions.

4.1.2 Cyclic voltammetry of reversible systems

A simple cyclic voltammogram for a reversible system, cf. below, in homogenous solution is shown in Figure 4.2. The scan is started at a potential negative of $E^{0'}$, when the electro-active molecule is in its reduced form. As the electrode potential ap-

proaches $E^{0'}$, oxidation begins and a current starts to flow [57]. The current depends on two steps in the overall process, i.e. the diffusion of electro-active material to the electrode surface and the interfacial electron transfer reaction itself [58]. The first step is determined by the concentration gradient at the electrode surface and the second step by the electrode potential. The concentration of the redox species at the electrode surface drops to zero and the concentration gradient assumes a maximum value as the potential passes $E^{0'}$, and the current reaches its maximum, i_a, at the anodic peak potential E_a. At potentials higher than E_a, the current decreases as depletion of the reduced form close to the electrode sets in and the concentration gradient is gradually lowered and the mass transfer to the electrode declines. This appears as a peak in the voltammogram [57]. When the sweep is reversed, there is a significant concentration of the oxidized species near the electrode surface. Some further oxidation will continue until the potential approaches $E^{0'}$. As the potential approaches $E^{0'}$, reduction of the oxidized species will, however, gradually dominate and a reverse current will flow [59].

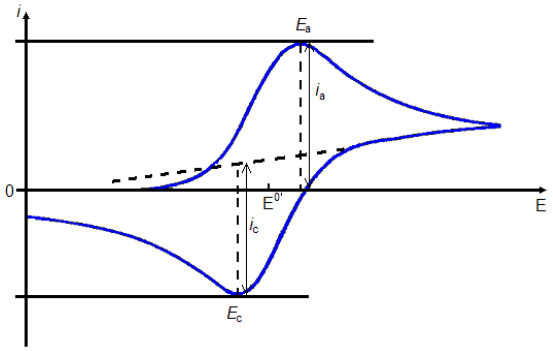

Figure 4.2: Cyclic voltammogram for a homogenous solution. $E^{0'}$ = formal potential, E_a = anodic peak potential, E_c = cathodic peak potential, i_a = anodic peak current, and i_c = cathodic peak currentl.

An electrochemical reaction is termed reversible if the reaction is fast enough to maintain equilibrium between the concentrations of the oxidized and reduced forms at the electrode surface [58]. This implies that the electron transfer rates are larger than the mass transfer rates [59]. The separation between the anodic and the cathodic peak potential, ΔE_p, is independent of the scan rate for a reversible process. For an n-electron process

$$\Delta E_p = \left| E_{p,a} - E_{p,c} \right| = 2.2\frac{RT}{nF} \quad \left(= \frac{59\,\text{mV}}{n} \text{ at } 25\,^{\circ}\text{C} \right) \tag{4-1}$$

The average of the anodic and the cathodic peak potential is, further, a good approximation for the formal potential of the redox couple, $E^{0'}$ [58].

$$E^{0'} \approx \frac{E_{p,a} - E_{p,c}}{2} \tag{4-2}$$

The peak current, i_p, is given by the Randles-Sevčik equation:

$$i_p = 0.4463nFAC^{*}\left(\frac{nF}{RT}\right)^{1/2} \nu^{1/2} D^{1/2} \tag{4-3}$$

where A is the electrode area, C^* the bulk concentration of the electro-active species, ν the scan rate and D the diffusion coefficient [57]. From (4-3) there is a linear dependence between i_p and $\nu^{1/2}$. This relation can be an indication of diffusion control. Totally irreversible processes, however, also follow such a dependency, cf. below. i_a and i_c are numerically the same for reversible processes [59].
The difference between the peak potential and the potential at the half peak height, $E_{p/2}$, is another important characteristic of electrochemical reaction. This quantity depends on the number of electrons involved in the reaction and is given by (4-4) for a reversible reaction [59].

$$\left|E_p - E_{p/2}\right| = \frac{59}{n} \text{ mV at } 25\,^{\circ}\text{C} \qquad (4\text{-}4)$$

4.1.3 Cyclic voltammetry of non-reversible systems

The electron transfer rates in an irreversible system are not high enough to maintain surface equilibrium at all scan rates. The shape of the voltammogram therefore changes but a linear dependence between i_p and $\nu^{1/2}$ remains as for the reversible process:

$$i_p = 2.99 \cdot 10^5 n(\alpha n_\alpha)^{1/2} A C^* D^{1/2} \nu^{1/2} \qquad (4\text{-}5)$$

The slope, however, is now also determined by the kinetic parameters of the process such as the charge transfer coefficient, α, a number between 0 and 1. n_α is the number of electrons in the rate determining step. No parts of the peaks overlap in a totally irreversible system. A subset of this class is chemically irreversible reactions, which yield products that cannot be recycled electrochemically [58]. Another characteristics of the irreversible system is a shift of the peak potential with increasing scan rates, cf. below. In an irreversible reaction $|E - E_{p/2}|$ also depends on α and n_α [59]:

$$\left|E_p - E_{p/2}\right| = \frac{48}{\alpha n_\alpha} \qquad (4\text{-}6)$$

which gives 96 mV for a one-electron irreversible reaction with α = 0.5, i.e. significantly higher than for reversible systems.

A system can be "effectively" reversible at low scan rates. At higher scan rates the peak-peak separation, however, increases to values larger than 59/n. This type of system is termed quasi-reversible. The transition from reversible to totally irreversible behavior occurs when the electron transfer reaction is too slow to maintain equilibrium at the electrode surface. In the quasi-reversible system both the forward and reverse reactions contribute to the observed current [58]. The transition from reversible, trough quasi-reversible, to irreversible behavior is shown schematically in Figure 4.3. Both the reversible and the irreversible peak current have a linear relation to $\nu^{1/2}$, but with different slopes. When the system changes from reversible to irreversible behaviour it passes through the quasi-reversible region with an increasing but non-linear dependence of the square root of the scan rate [59].

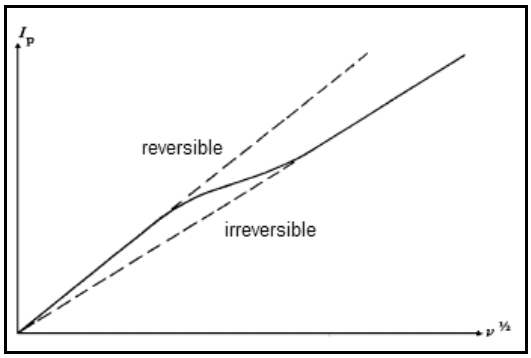

Figure 4.3: Plot the peak current in diffusion controlled systems as a function of the square root of the scan rate, showing the transition from reversible to irreversible behaviour. [4]

In the quasi-reversible region, the rate constant for the electron transfer reaction, k_s, can be determined from the peak separation by the following relation:

$$\psi = \frac{\gamma k_s}{\sqrt{aD\pi}} \qquad (4\text{-}7)$$

where $\gamma = (D_O/D_R)^{1/2}$ (we take here $\gamma = 1$), a = $nF\nu/RT$, and the kinetic parameter ψ can be obtained from working curves as function of $n\Delta E_p$ [60]. When the system approaches reversibility and $n\Delta E_p$ becomes smaller than 70 mV, ψ becomes very large and changes strongly for even small changes in ΔE_p, making accurate determination of the rate constant impossible. On the other hand, when $n\Delta E_p$ becomes larger than 150 mV, *i.e.* approaches total irreversibility, ψ changes very little with changes in ΔE_p, again resulting in inaccurate rate constant determination.

4.2 Electron paramagnetic resonance spectroscopy

EPR spectroscopy is a technique used to study paramagnetic centers, i.e. species containing one or more unpaired electrons. It can thus be used to study metal centers in metalloproteins. A deep quantum mechanical understanding is not always necessary to describe, quantify and interpret biomolecular EPR spectra [61] and metal centers in proteins are often investigated by comparisons to similar compounds. The expressions given in this part of the thesis are sufficient for the analysis of the EPR spectroscopic characterization in the experimental section of the thesis.

4.2.1 Basic principle

A charged particle that moves generates a magnetic field with an associated magnetic moment, μ. An electron has an intrinsic magnetic moment, μ_e, arising from the electron's spin around it's own axis, **S**. The relation between the magnetic moment and the spin is described as

$$\mu_e = -g\beta\mathbf{S} \qquad (4\text{-}8)$$

where β is the Bohr magneton, a physical constant with value $9.2740 \cdot 10^{-24}$ J/T, and g is a dimensionless proportionality factor termed the g factor. The g factor depends on the system under investigation. The g-value of a free electron (and radicals) is 2.0023, the paramagnetic metal systems can exhibit g-values substantially different from 2.

If an electron is exposed to an external magnetic field, ***B***, its change in energy, E, is:

$$E = g\beta m_S B \qquad (4\text{-}9)$$

where m_S is the electron spin quantum number, which can have two values, +½ or -½., depending on the orientation of the electron's magnetic moment in the field. m_S is +½ if **S** is directed along **B** and -½ if it is in the opposite direction of **B**. As a consequence, the electron can have two energies, namely $E = \pm\frac{1}{2} g\beta B$, and the splitting between two energy levels ($\Delta E = g\beta B$) is proportional to the strength of the magnetic field, Figure 4.4. Due to Boltzmann distribution, more electrons will be in the lower, spin-down, energy level than in the spin-up level at low temperatures.

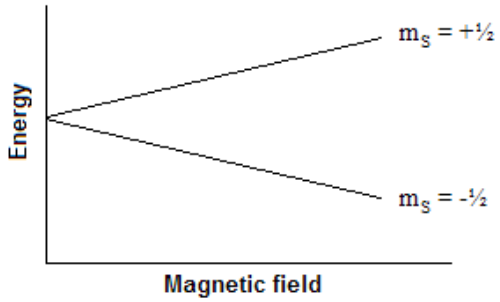

Figure 4.4: Splitting of the energy levels of an unpaired electron in a magnetic field.

The electron can flip to the higher energy state upon exposure to electromagnetic radiation. The requirement for transition is that the energy of the radiation, $h\nu$, is equal to the energy separation between the two levels:

$$h\nu = g\beta B \qquad (4\text{-}10)$$

m_S can only change by ±1 during an EPR transition.

The population of the two energy levels follows the Boltzmann distribution and therefore depends on temperature. When the temperature is lowered, the percentage of electrons in spin down orientation increases and the probability of absorbing microwaves increases. It therefore follows that the sensitivity of EPR measurements increases with decreasing temperature.

Standard EPR instruments are so-called continuous wave spectrometers, in which the frequency of the radiation source is kept constant and the field is varied. From (4-10) $B = h\nu/g\beta$, or more conveniently, $g = h\nu/\beta B$. The *g*-value can therefore be calculated straightforwardly from the field of the maximum absorption. It is worth to notice that *B* and *g* are inversely proportional and low *g*-values thus appear at high fields and high *g*-values appear at low fields. [62]

In order to decrease the noise and increase the sensitivity, standard EPR measurements are represented as a spectrum of the first derivative of the observed EPR absorption with respect to the magnetic field. An absorption peak will therefore result in a peak and a crossing of zero followed by a negative peak in the first derivative spectrum with the zero crossing at the absorption maximum. Peaks and other features in the first derivative spectrum correspond to inflection points in the EPR absorption

spectrum. By double integration of the standard EPR spectrum, the area under the EPR adsorption spectrum is obtained. This quantity is proportional to the "spin concentration". EPR measurements can therefore be used for relative concentration determination and for determination of the spin of the sample [63].

4.2.2 Anisotropy

The *g*-factor depends on the electronic structure and orientation of the paramagnetic centre. This is understood by considering e.g. a low-spin Fe(III) heme with a single unpaired d-electron with methionine and histidine as the axial ligands, Figure 4.5, with the Cartesian *x*- and *y*-axes in the porphyrin ring plane and the *z*-axis along the methionine and histidine bonds. The EPR absorption depends on the orientation of the paramagnetic centre in the external field. If the molecule is placed with the *x*-axis in the same direction as the field, the *g*-value with maximum absorption will depend on the electronic structure in the porphyrin ring as this affects the properties of the unpaired d-electron. The absorption will be the same with the field aligned along the *y*-axis, since the porphyrin ring is symmetric. If, however, the field is aligned along the *z*-axis, the g-value will be different, since it is now affected by the electronic structure of the histidine and methionine ligands [61].

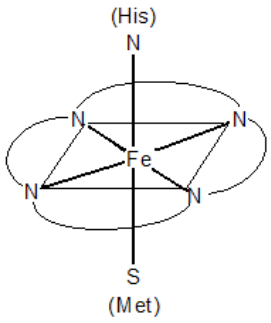

Figure 4.5: Schematic representation of Fe(III) heme with methionine and histidine axial ligands.

A solution contains a distribution of randomly oriented molecules. The *g*-value for each orientation is a weighted mean of the principal *g*-values, g_x, g_y, and g_z.

If all three *g*-values are identical, $g_x = g_y = g_z$, the EPR absorption is independent of the molecular orientation. The resulting derivative spectrum is termed isotropic and has a positive peak immediately followed by a negative peak. The zero crossing corresponds to the absorption maximum and the *g*-value [62].

If one of the *g*-values differs from the other two, a) $g_x = g_y < g_z$ or b) $g_x = g_y > g_z$, as in the example above, the EPR spectrum is axial. The absorption spectrum will have one minor peak at g_z and a major peak corresponding to the two identical *g*-values. The absorption at the two identical *g*-values is higher than at g_z since there are more molecules with the **B** vector anywhere in *xy* plane than in molecules with **B** parallel to the *z*-axis [61]. The derivative spectrum will have a zero crossing from g_x and g_y, and g_z resulting in either a) a positive peak at lower field (and higher *g*-value) or b) a

negative peak at higher field (and lower *g*-value) [62].

If all three *g*-values are different, $g_x \neq g_y \neq g_z$, the spectrum is termed rhombic. The absorption spectrum now has one peak from g_y with shoulders on each side of the peak corresponding to g_x and g_z. The resulting derivative spectrum will have a positive peak at low field from g_z, a zero crossing from g_y, and a negative peak from g_x [62].

Proteins contain distributions of structures retained even in crystallized proteins and in the frozen aqueous solutions commonly used for EPR spectroscopy [64]. The consequence of this is a field dependent inhomogeneous line width contribution, termed *g*-strain [65]. *g*-strain can be described by not-straightforward statistical theory (not to be described here), which allows simulation of the effects. Simulated *g*-strain effects are denoted *W* in this thesis. It has been suggested that *g*-strain contains information on the ligands in a metalloprotein, but the nature and causes of *g*-strain are not fully understood [61].

4.2.3 Hyperfine interactions

The paramagnetic centre can also be influenced by an interacting nucleus with spin, the relevant nucleus being either the metal ion nucleus or a ligand atom nucleus. This section focuses on such metal ion hyperfine interactions.

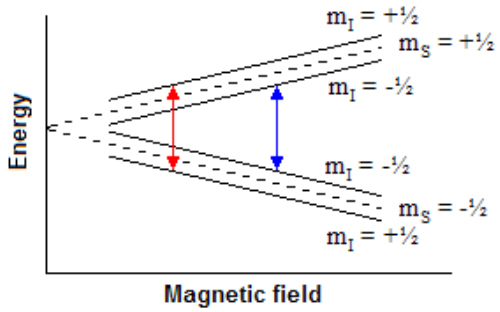

Figure 4.6: Hyperfine splitting of $m_S = ±½$ levels upon interaction with a nucleus with $m_I = ±½$.

A nucleus has a charge and when it also posses a spin, it will posses a magnetic moment and it is therefore the source of a magnetic field, the nucleus hyperfine field. The hyperfine field modifies the energy levels of the electron by splitting them up. E.g. if an electron with spin S = ½ interacts with a nucleus with spin I = ½, then each of the two $m_S = ±½$ states will be split up in two $m_I = ±½$ states as illustrated in Figure 4.6. The selection rule for allowed transition is $\Delta m_S = ±1$ and $\Delta m_I = 0$. That gives two allowed transitions in the example; one from the $m_S = -½$, $m_I = -½$ state to the $m_S = +½$, $m_I = -½$ state (blue arrow), and one from the $m_S = -½$, $m_I = +½$ state to the $m_S = +½$, $m_I = +½$ state (red arrow). If the energy of the radiation is constant, the latter transition will occur at lower field. The difference in magnetic field is termed the hyperfine splitting, *A*. A nucleus with nuclear spin *I* will give rise to $2I + 1$ hyperfine interaction lines [62]. The magnitude of *A* depends on the strength of the interaction between the nucleus and the electron [63].

The interaction between the electron and the nucleus depends on the spatial distribution of the electron. This distribution not only depends on the orbital with the unpaired electron, but can also be different in different directions. The hyperfine splitting, *A*, thus depends on the direction and is anisotropic [62].
The widths of hyperfine lines are affected by inhomogeneous broadening similar to *g*-strain. For hyperfine interactions the effect is termed *A*-strain. *A*-strain causes asymmetries in the hyperfine line width that depend on the nuclear quantum number. *A*-strain is simulated with asymmetric parameters. *A*-strain effects are less understood than *g*-strain effects [61].

4.2.4 EPR monitored redox titration

EPR can be used for determination of redox potentials of metalloproteins.
Metalloprotein redox reactions are usually one-electron reactions. Redox reactions are therefore often transitions between states with different electron configurations, i.e. states with different EPR signals, most often between an EPR silent state and an EPR active state. A relative measurement of the concentration of the EPR active specie can be estimated through double integration of the EPR spectrum (see section 4.2.1). It is therefore possible to use EPR for relative measurement of the concentration at different potentials if the potential of a sample can be controlled and changed.
A frequently used method is by having the protein in a solution with a mixture of redox mediators with redox potentials distributed in the desired potential range. The potential of the solution with respect to a reference electrode can be measured using a platinum wire. The protein (and the mediators) are then reduced or oxidized by stepwise addition of either a reductant, most often $S_2O_4^{2-}$, or an oxidant, $[Fe(CN)_6]^{3-}$. When equilibrium is reached at (or near) the desired potential a sample is taken out and frozen in liquid N_2 for subsequent EPR measurements. [61]

Table 4.1: Translated Nernstian equations in three different situations [61].

Situation	Translated Nernstian expression
oxidized form is EPR active	$i_{OX} = \frac{i_{max}}{1+\exp((E^{0'}-E)\frac{nF}{RT})}$
reduced form is EPR active	$i_{OX} = \frac{i_{max}}{1+\exp((E-E^{0'})\frac{nF}{RT})}$
intermediate in a two-step reaction is EPR active	$i_{OX} = \frac{i_{max}}{1+\exp((E-E_1^{0'})\frac{nF}{RT})+\exp((E_2^{0'}-E)\frac{nF}{RT})}$

The relative concentrations at the various potentials are then plotted in a diagram to fit to a Nernstian curve. The Nernst equation can be translated to equations in terms of EPR intensity, *i* (area under the adsorption curve) [61]. These equations are given in Table 4.1.

4.2.5 Quantification

EPR spectra can be used for quantification of paramagnetic species by double integration of the spectrum, cf. section 4.2.1. The doubly integrated spectrum gives a relative measure of the concentration of the paramagnetic spin. The "spin concentration" of an unknown sample is determined by comparing it to the intensity of a known standard sample. The concentration of the unknown sample is given by:

$$c_U = c_S \frac{\iint_U}{\iint_S} \frac{I_S}{I_U} \tag{4-11}$$

where the subscripts "U" and "S" refers the unknown and the standard sample, respectively. *I* is an intensity factor that depends on the g-values and can be approximated by:

$$I \cong \frac{2}{3}\sqrt{\frac{g_x^2 + g_y^2 + g_z^2}{3}} + \frac{g_x + g_y + g_z}{9} \tag{4-12}$$

(4-11) only applies if all experimental conditions are the same for the two measurements. If that prerequisite is not fulfilled, one has to take these factors into account and use:

$$\frac{c_U}{c_S} = \frac{\iint_U}{\iint_S} \frac{I_S}{I_U} \frac{M_S}{M_U} 10^{\frac{P_U - P_S}{20}} \left(\frac{W_S}{W_U}\right)^2 \frac{G_S}{G_U} \frac{d_S}{d_U} \frac{T_U}{T_S} \tag{4-13}$$

where *M* is the modulation amplitude, *P* is the microwave power attenuation, *W* is the magnetic field scan width, *G* is the electronic gain, *d* is the sample diameter, and *T* is the sample temperature [61].

4.3 Instrumentation, setups and materials

4.3.1 Anaerobic systems

Most of the experimental work was performed under anaerobic conditions, since both the wild type ferredoxins and the modified proteins are highly sensitive to oxygen.

A LabStar 50 glove box (M. Braun) with nitrogen atmosphere was used for most of the work. This box was prepared for protein purification by S. S. Helt [66]. It was equipped with an HPLC system (ÄKTAprime™, GE Healthcare) enabling measurement of the absorbance at 280 nm, a spectrophotometer (NanoDrop ND-1000, NanoDrop Technologies) and a magnetic stirrer. The glove box did not have a humidity control system. Solutions were therefore kept tightly sealed when not in use. Also, there was no temperature control in the box. The temperature could therefore vary during the work. Most often the temperature was ~27 °C during experiments. This glove box was setup for electrochemistry in the present work.

A smaller part of the work was carried out using Anaerobic Flexible Vinyl Coy Chambers (Coy Laboratories) with a nitrogen/hydrogen atmosphere (2-4% hydrogen). This system was equipped like the box with a similar HPLC system, spectrophotometer and a magnetic stirrer. In addition, this chamber had an inlet to provide N_2

to add pressure to Vivacell caps and was primarily used for concentration of purified samples after transferring the samples either in the sealed Vivacell 70 or in another sealed container from the other glove box. A Vivacell 70 (Sartorius Stedum Biotech) equipped with a 5000 MWCO membrane was used for concentration of samples and changing buffers throughout the experimental work. This glove box was also used to prepare samples for EPR monitored redox titrations.
In all experiments in both boxes, the oxygen concentrations were below the detection limit of the gas analyzers.

4.3.2 Setup for anaerobic electrochemistry

The setup for electrochemistry inside the glove box was based on the in-house setup for electrochemical experiments (described in a number of papers, e.g. [67]). This system is a three-electrode, two-chamber electrochemical cell with the reference electrode in one smaller chamber and the working electrode and the counter electrode in a bigger chamber. The counter electrode is a Pt-wire. The reference electrode is a home-made, freshly prepared reversible hydrogen electrode. The choice of working electrode depends on system and desired information.
It was desired to set up a similar system in the Labstar 50 glove box (M. Braun). The biggest obstacle towards this goal was that all electrodes should be transferred through the vacuum antechamber prior to each experiment since the glove box was not equipped with (and did not have room for) electrode polishing equipment. The electrochemical cell and the counter electrode could be transferred to the glove box without problems. It was, however, not possible to transfer hydrogen electrodes into the glove box, since the solution and the hydrogen would simply leak in the vacuum chamber. Instead, a commercially available Ag/AgCl electrode (Metrohm) was used. This electrode could be sealed and was transferred without leakage in the antechamber. An edge-plane pyrolytic graphite electrode (EPG) was the working electrode in the presented experiments. It was necessary to protect the electrode surface from vacuum to maintain the active electrode surface. The electrode was therefore transferred with water in the cap and sealed. This proved to maintain the active surface and no leakage was observed upon transfer trough the antechamber. Two EPG electrodes were used; a home-made electrode with d = 0.4 cm and a commercially available electrode with d = 0.5 cm (Pine Instruments). Both were coated with Teflon to ensure that only one plane, the edge plane, is in contact with the solution through a known area. The EPG electrodes were polished with SiC paper followed by ø = 1 µm and ø = 0.05 µm Al_2O_3 slurry and ultrasonicated twice in water prior to each experiment before they were transferred to the glove box. The potential of the Ag/AgCl reference electrode was checked versus a saturated calomel electrode after each experiment and potentials were converted to E versus the standard hydrogen electrode by using the factor E(SCE vs. SHE) = 0.244 V [56].
The glove box was already equipped with multiple coax cables suitable for connecting the electrodes to a potentiostat. Cyclic voltammetry was performed on an Electro-

chemical Analyzer/Workstation, 700C Series (CH Instruments) controlled by the accompanying CH Instruments software.
The anaerobic electrochemical setup was tested as described in (chapter 5).

4.3.3 EPR sample preparation, measurements and data analysis

Samples for EPR spectroscopy were prepared in quartz tubes and frozen in liquid N_2. Protein samples were prepared inside the glove box, sealed with a rubber lid, taken out through the antechamber, and frozen immediately, followed by removal of the lid. The samples were stored and shipped in liquid N_2.
The redox mediators used for EPR spectroscopic monitored redox titrations are listed in Table 4.2. Benzyl viologen and methyl viologen themselves give EPR active radicals in their reduced forms, disturbing the spectra at low potentials. TMPD is a two electron donor.

Table 4.2: Redox mediators used for EPR monitored redox titrations and their formal potentials.

Mediator	E^0 (mV vs. SHE)
N,N,N',N'-tetramethyl-p-phenylendediamine (TMPD)	+276
2,6-dichlorophenol indophenol (DCIP)	+217
Phenazine ethosulfate (PES)	+55
Methylene blue	+11
Resorufine	-51
Indigodisulfonate (indigo carmine)	-125
2-hydroxy-1,4-naphtaquinone	-145
Anthraquinone-2-sulfonate	-225
Phenosafranin	-252
Safranin O	-280
Neutral red	-340
Benzyl viologen	-350
Methyl viologen	-440

EPR monitored redox titrations were carried out by dissolving the listed mediators in 50 mM buffer (in this project Tris/HCl, pH 8.0) with 0.25 M NaCl to a concentration of 155 mM of each mediator. This solution was mixed with protein solution in a small glass cell in a 1:1 ratio. A reference Ag/AgCl electrode (Princeton Applied Research) and a Pt-wire were inserted in the cell and the potential measured. Small aliquots of freshly prepared solutions of $Na_2S_2O_4$ or $K_3Fe(CN)_6$ in 50 mM Tris/HCl, pH 8.0 were added to the solution to reduce or oxidize the mix. Samples were taken out at the desired, stable potentials by transferring 200 µl of the solution to an EPR tube and freezing it as described above. The potential was measured at the time of freezing,

assuming that what potential changes that happen in the solution in the cell also happen in the solution in the EPR tube. The potential of the reference electrode was checked versus a saturated calomel electrode and potentials were converted to E versus the standard hydrogen electrode by using the factor E (SCE vs. SHE) = 0.244 V [56].
All EPR spectroscopic measurements were carried out in the laboratory of Professor Wilfred R. Hagen at Delft University of Technology. X-band spectra were recorded on a Bruker ER 200 D spectrometer with an ER 4116 DM resonator and a home-built cooling flow system for liquid He or liquid N_2. The recorded spectra were analyzed using WR Hagen Visual Software programs [68]. Quantification of intensity was performed by double integration. In spectra with radical signals, the radical signal was quantified and subtracted from the double integral of the full spectrum. Molar quantification was carried out by comparison of intensity to a Cu^{2+} standard sample 10.00 mM $CuSO_4$ in 10 mM HCl + 2 M $NaClO_4$; a S = ½ system which *g*-values are $g_{\|}$ = 2.404 and $g_{\perp}$ = 2.076 and $A_{\|}$ = 131 and $A_{\perp}$ unresolved [61].
The intensities of EPR spectra (as found by double integration) were adjusted to the same conditions according to the relations between the different experimental parameters in 4-13 when necessary and divided by the concentration of protein in the sample before plotting titration curves. The concentration was adjusted by the added volumes of $Na_2S_2O_4$ and/or $K_3Fe(CN)_6$ solutions.

4.3.4 Chemicals and column materials

All chemicals applied were of analytical grade. Water used throughout the experiments was 18.2 MΩcm QPAK Milli-Q (Millipore).
MoO_3 enriched in ^{95}Mo was purchased from Medical Isotopes, Inc., as 94.74% enrichment.
Pre-packed columns and column materials for home-packed columns for HPLC or gravitational protein purification were purchased from Amersham Biosciences (GE Healthcare).
Column materials for purification of molybdenum-sulfur clusters were purchased from Sigma-Aldrich.

CHAPTER FIVE

5 Purification and Electrochemical Studies of Iron-Sulfur Proteins

5.1 Introduction

This chapter describes the studies of *P. furiosus* $[Fe_3S_4]$ and $[Fe_4S_4]$ ferredoxin. These studies serve as reference for the studies of the modified ferredoxins described in chapters 6 and 9. The electrochemical studies of the $[Fe_3S_4]$ and $[Fe_4S_4]$ ferredoxins were also used to test the setup for anaerobic electrochemistry (chapter 4.3.2). Also included in this chapter are the electrochemical studies of ancient ferredoxins that are being investigated in our group.

The electrochemical properties of both *P. furiosus* ferredoxins have been studied thoroughly [67, 69, 70]. Armstrong et. al. studied both the $[Fe_3S_4]$ and the $[Fe_4S_4]$ ferredoxins in solution and adsorbed as a protein film on the electrode surface [69]. Members of the Nanoscale Chemistry group have studied the $[Fe_3S_4]$ ferredoxin in homogeneous solution and adsorbed as a self-assembled monolayer on single-crystalline gold surfaces modified by a molecular monolayer of a linker molecule [67]. Hagen et. al. have studied the $[Fe_4S_4]$ ferredoxin in solution and directly adsorbed on polycrystalline gold electrodes [31, 70]. The $[Fe_4S_4]$ ferredoxin was studied briefly under conditions similar to the studies of $[Fe_3S_4]$ ferredoxin in ref. 67 in my M.Sc. thesis [71].

In this project, proteins in homogeneous solution are studied under circumstances similar to the previous study in our group, with the exception that anaerobic conditions in a glove box are used. There was a large contribution from oxygen that had to be removed by hours of deoxygenation in the previous studies and since the proteins are very sensitive towards oxygen the use of anaerobic conditions is likely to be beneficial. The effects of different buffers and promoters are investigated.

Large amounts of *P. furiosus* ferredoxin have been used in this project both for these reference studies and for the syntheses of the modified ferredoxins, particularly the synthesis of the molybdenum-sulfur analogue (chapter 9). Most of the ferredoxin used was expressed and purified by me. The aerobically purified samples were frozen and

stored at -20 °C until further use.

Procedures for aerobic expression and purification of *P. furiosus* ferredoxin have been developed in the Metalloprotein Chemistry group [72], the final purification step being an anion-exchange step. Protein for sulfonation (for further incorporation of $[Mo_4S_4]$, chapter 9) was used in aerobically purified form, chapter 7, while samples for incorporation of Co^{2+} and for electrochemistry were prepared as described below.

5.2 Anaerobic purification of *P. furiosus* ferredoxin

Aerobically purified protein samples were re-purified in the glove box immediately before use for electrochemistry or for incorporation of Co^{2+} (chapter 6) to remove all traces of oxygen and to ensure pure samples. The re-purification step is similar to the final anion-exchange step in the purification protocol. The purification of $[Fe_3S_4]$ and $[Fe_4S_4]$ ferredoxin was used as reference for the purification of the $[CoFe_3S_4]$ ferredoxin and will briefly be described here.

5.2.1 Experimental

Frozen samples of *P. furiosus* ferredoxin were transferred into the glove box and purified by HPLC (ÄKTAprime^{TM} plus) by loading the protein on a 20 mM Tris/HCl, pH 8.0 equilibrated 16/10 Source 30Q column. The protein was eluted by a linear gradient, 0.20 M NaCl to 0.35 M NaCl in 10 column volumes, CVs, 6 ml/min. Collected fractions were concentrated using a Vivacell 70 with a 5000 MWCO membrane. The concentration was determined by UV-vis spectrophotometry, using the molar absorption coefficients determined by Conover et. al.: $18 \cdot 10^3$ $M^{-1}cm^{-1}$ at 408 nm for $[Fe_3S_4]$ ferredoxin and $17 \cdot 10^3$ $M^{-1}cm^{-1}$ at 390 nm for $[Fe_4S_4]$ ferredoxin [29].

5.2.2 Results

A representative chromatogram for purification of a mixture of $[Fe_3S_4]$ and $[Fe_4S_4]$ ferredoxin, $[Fe_4S_4]$ ferredoxin being the main component, is shown in Figure 5.1. The chromatogram is in agreement with results from aerobic purification according to the in-house standard protocols with two peaks from $[Fe_4S_4]^{2+}$ ferredoxin (eluting at ~25 mS/cm) and $[Fe_3S_4]^{+}$ ferredoxin (eluting at ~27.5 mS/cm), respectively, both in the oxidized forms.

The fractions containing the desired form of the protein were collected and pooled leaving out fractions with mixtures of the two forms. The remaining protein-containing fractions were collected and stored at -20 °C.

The normalized UV-vis spectra of the purified and concentrated fractions in Figure 5.2 show the spectral characteristics of the oxidized $[Fe_3S_4]$ and $[Fe_4S_4]$ ferredoxin; the absorption maximum of the $[Fe_3S_4]$ ferredoxin is at 408 nm and that of the $[Fe_4S_4]$ ferredoxin at 390 nm [73]. These spectra are in agreement with spectra for aerobically purified *P. furiosus* ferredoxins and confirm that the oxidized forms of the protein are the ones purified by this method.

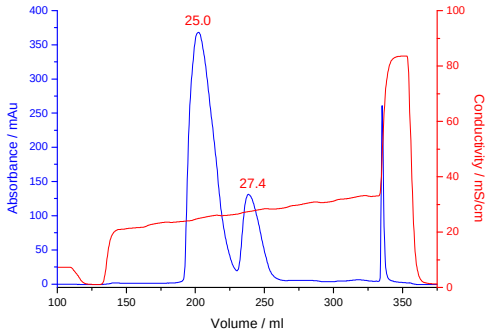

Figure 5.1: Chromatogram of anaerobic re-purification of a mixture of *P. furiosus* [Fe_3S_4] and [Fe_4S_4] ferredoxin on a 16/10 Source 30Q column. The blue line indicates the absorption at 280 nm and the red line the conductivity gradient. The numbers written in red indicate the conductivities at the absorption maxima.

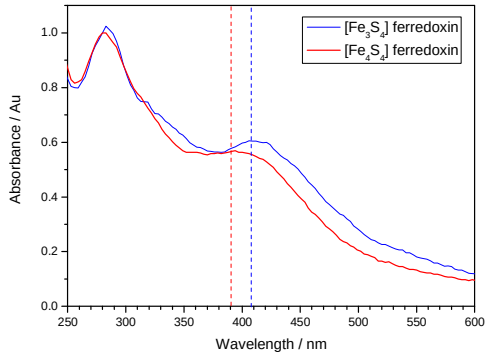

Figure 5.2: Normalized (according to the absorbance at 280 nm) UV-vis spectra of *P. furiosus* [Fe_3S_4] ferredoxin (blue line) and [Fe_4S_4] ferredoxin (red line). The dashed lines mark the adsorption maxima at 390 nm (red) and 408 nm (blue).

As the chromatograms and spectra from the anaerobic purification agree with the well-known protocols for aerobic purification, they are used for the subsequent studies without further characterization.

5.3 Electrochemical studies of *P. furiosus* [Fe_3S_4] ferredoxin

The electrochemical studies of [Fe_3S_4] ferredoxin serve as reference for the electrochemical studies of [$CoFe_3S_4$] ferredoxin. Redox signals observed in the presence of different buffers and different promoters under the conditions in the glove box were adressed. These studies are based on the previous studies on the protein in the Nanoscale Chemistry group [67]. Phosphate buffer was used in these studies since phosphate buffer is very suitable for the high-resolution studies of protein assembled on Au(111) that were also a part of that study. In the present study, use of Tris/HCl buffer is desired, since it is convenient to use the same buffer as for purification. Possible differences between results obtained from the two buffers were therefore checked. The effect of NaCl was also investigated, since traces of NaCl from the ion-exchange purification step can be present in the concentrated sample. Neomycin and cysteine were used as promoters as in previous experiments [67, 69].

5.3.1 Experimental

The buffer was changed to either 20 mM Tris/HCl, pH 8.0 or 5 mM phosphate buffer, pH 7.9 (prepared from K_2HPO_4 and KH_2PO_4) by reducing the volume in a Vivacell 70 and diluting ~50 times with the desired buffer. This was repeated three times. The concentrations of the final samples were determined by UV-vis spectrophotometry.

The EPG working electrode was polished and transferred into the glove box as described in chapter 4.3.2. The electrodes were mounted in the electrochemical cell containing 43 µM $[Fe_3S_4]$ ferredoxin in the desired buffer as also described in chapter 4.3.2.

For experiments with buffers containing NaCl, the sample in 20 mM Tris/HCl, pH 8.0 was diluted with appropriate amounts of 20 mM Tris/HCl, 0.5 M NaCl, pH 8.0 and 20 mM Tris/HCl, 1 M NaCl, pH 8.0. A titration with small amounts of NaCl was carried out by adding appropriate volumes of 43 µM $[Fe_3S_4]$ ferredoxin in 20 mM Tris/HCl, pH 8.0, 1 M NaCl to the non-NaCl containing solution of 43 µM $[Fe_3S_4]$ ferredoxin in 20 mM Tris/HCl, pH 8.0. The experiments were carried out at 27 °C.

Neomycin sulfate powder and L-cysteine powder were added to the solution during experiments without further purification by dissolution in a small volume of the protein solution and transferring this to the cell. Both promoters were used at 5 mM concentrations.

5.3.2 Results and discussion

No redox signals were observed in the absence of promoter, in agreement with previous results [67, 69]. A pair of well-defined redox peaks appears at similar potentials in both in phosphate buffer and in Tris/HCl buffer without NaCl upon addition of neomycin, Figure 5.3. Notably, when the experiment was carried out in Tris/HCl buffer with 0.5 M NaCl, there is no signal at this potential. There are some not-very-well defined broad peaks at lower potentials. This signal has some resemblance to the large oxygen signal observed for experiments carried out under aerobic conditions [67, 71] and might be due to trace amounts of oxygen in the glove box.

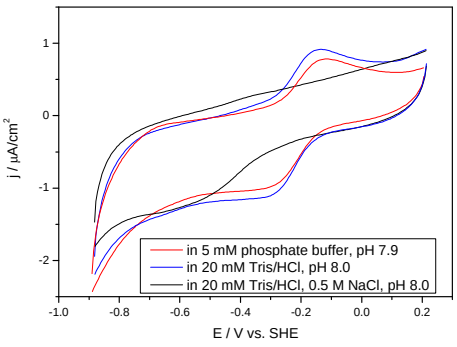

Figure 5.3: Cyclic voltammograms of 43 µM *P. furiosus* $[Fe_3S_4]$ ferredoxin with 5 mM neomycin in different buffers as indicated, scan rate = 5 mV/s.

The effect of NaCl was investigated further in a titration experiment in which NaCl was added to the protein solution during the experiment. The results of this experiment are shown in Figure 5.4. These voltammograms show that the peaks broaden and move apart even at very low NaCl concentrations. The protein signal has completely disappeared at 50 mM NaCl and the broad signal at lower potentials appears, suggesting that this signal is not due to oxygen, but more likely an effect of NaCl. From these results it is obvious that the redox properties of the protein are very sensitive towards NaCl.

P. furiosus ferredoxin is known to have different properties depending on the salt concentration. Hagen et. al. have suggested monomer/dimer interaction depending on the salt concentration, the dimeric form being present at c(NaCl) < 0.5 M. Results by other members of our research group suggest that it is more likely that salt changes the hydrodynamic radius of the protein [66]. Both effects could alter the properties of the protein, including the redox properties, significantly. One could imagine some kind of screening of the protein in the presence of salt, though Cl^- ions are already present in the solution at 0 mM NaCl due to the preparation of the buffer with HCl.

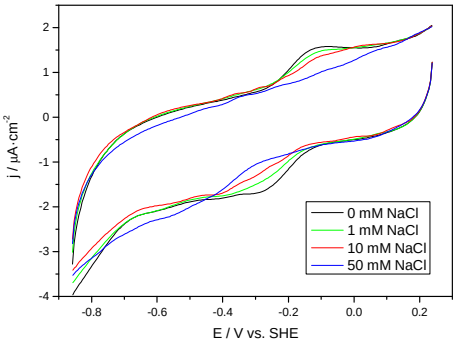

Figure 5.4: Cyclic voltammograms of 43 µM *P. furiosus* [Fe_3S_4] ferredoxin with 5 mM neomycin in 20 mM Tris/HCl, pH 8.0 + NaCl as indicated, scan rate = 5 mV/s.

Table 5.1: Redox parameters of *P. furiosus* [Fe_3S_4] ferredoxin in the presence of neomycin in different buffers at 5 mV/s. Potentials are given in mV vs. SHE. The results from previous studies within our research groups are given for comparison.

	E_a	E_c	$E^{0'}$	ΔE_p	$E_{p/2}$
5 mM phosphate buffer, pH 7.9	-126	-320	-223	194	99
20 mM Tris/HCl, pH 8.0	-146	-315	-231	169	87
Outside glove box, 5 mM phosphate buffer, pH 7.9 [67]	-136	-236	-186	100	

The parameters of the voltammograms in Figure 5.3 are given in Table 5.1 and compared with the results from the experiments outside the glove box [67]. The characteristics are similar for the two experiments carried out in the glove box, though the peak-peak separation is larger in phosphate buffer. The differences observed between the two buffer systems could arise from different buffer systems with slightly

different pH and different ionic strengths. The formal potentials are ~40 mV lower for these new experiments performed inside the glove box and the peak-peak separation is also significantly larger. The anodic peak potentials are similar, but the cathodic peak potential has shifted 80 mV to lower potentials.

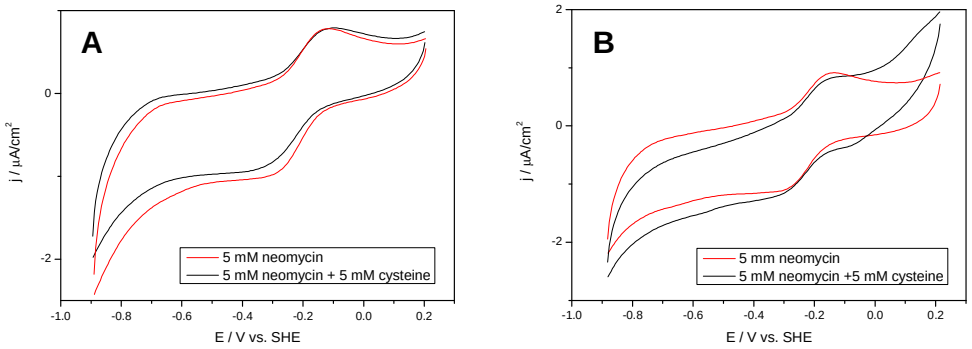

Figure 5.5: Cyclic voltammograms of 43 µM *P. furiosus* [Fe_3S_4] ferredoxin with neomycin and cystein as indicated in either A) 5 mM phosphate buffer, pH 7.9, or in B) 20 mM Tris/HCl, pH 8.0, scan rate = 5 mV/s.

A second redox pair has been observed for [Fe_3S_4] ferredoxin. Armstrong et. al. reported a two-electron transition redox couple at lower potentials [69]. The study by members of the Nanoscale Chemistry group revealed a one-electron redox-couple upon the addition of a second promoter with a carboxyl group, such as cysteine [67]. Since the present study primarily is based on the latter, it was attempted to add cysteine in order to promote the second redox transition. The voltammograms in Figure 5.5 show the results of this addition in both phosphate buffer and in Tris/HCl buffer. There is clearly no appearance of the second redox couple upon addition of cysteine in either case. In the previous study, the second redox couple was only observed at low scan rates, but was present as a well-defined pair of peaks at 5 mV/s [67, personal communication with J. Zhang]. In the present voltammograms, there are no indications of any redox transition in the lower potential window even at 5 mV/s.

The most significant difference between these experiments and the experiments in ref. 67 is the use of a Ag/AgCl reference electrode as opposed to a reversible hydrogen electrode in ref. 67. A different reference electrode was used presently, since it is not possible in the current setup to transfer a homemade reversible hydrogen electrode into the glove box. A commercially available Ag/AgCl electrode was therefore used. Recent experiments on other variants of *P. furiosus* ferredoxins in the Metalloprotein group [74] have suggested that leakage of Ag^+ from the reference electrode leads to formation of ferredoxin containing the [$AgFe_3S_4$] cluster. The presence of this cluster was proven by mass spectrometry, which was not available during the early studies presented in this chapter. It is reasonable, that incorporation of Ag^+ in the [Fe_3S_4] leads to the observed changes in the voltammograms, i.e. shift in cathodic peak potential and absence of the redox couple at lower potentials.

Another difference is that there was a significant amount of oxygen in the sample and

it was necessary to scan for several hours while flushing with Ar to remove oxygen contributions in the voltammograms in the experiments performed outside the glove box [67, 71]. This was not necessary when the experiments were performed in the glove box. It is possible that the differences observed arise from the long time exposure to oxygen during the electrochemical experiment. Armstrong et. al. observed changes in the voltammograms in form of attenuated peaks on continued cycling [69].

5.4 Electrochemical studies of *P. furiosus* [Fe_4S_4] ferredoxin

Similar to the electrochemical studies of the [Fe_3S_4] ferredoxin, the studies of [Fe_4S_4] serve as reference for the studies on [$CoFe_3S_4$] ferredoxin as well as the [Mo_4S_4] analogue. This work is a continuation of work in my M. Sc. project studying the [Fe_4S_4] ferredoxin under similar conditions as the published studies on [Fe_3S_4] ferredoxin [67]. The signal arising from [Fe_4S_4] ferredoxin was disturbed by a signal arising from oxygen that was removed by scanning for several hours under Ar flushing. The redox signal was also only stable at very low scan rates. It is likely that these results can be improved since the [Fe_4S_4] ferredoxin is sensitive to oxygen. The studies using the glove box therefore also serve as a check of the anaerobic conditions in the glove box. As for the [Fe_3S_4] ferredoxin the effects of different buffers and promoters were studied.

5.4.1 Experimental

Samples in either 20 mM Tris/HCl pH, 8.0 with or without 0.5 M NaCl or 5 mM phosphate buffer, pH 7.9 were prepared as described in chapter 5.3.1. The electrodes were prepared and mounted in the cell as described in chapter 4.3.2.

Neomycin sulfate powder and L-cysteine powder without further purification were added by dissolving in a small amount of protein solution and transferring this solution to the electrochemical cell and used as 5 mM concentrations.

Experiments were carried out at the working temperature in the glove box, i.e. ~27 °C.

5.4.2 Results and discussion

No redox-couples were observed in the absence of neomycin in agreement with other observations [31, 69, 71]. A well-defined pair of redox peaks appears upon addition of neomycin both in 20 mM Tris/HCl, pH 8.0 and 5 mM phosphate buffer, pH 7.9, Figure 5.6. Similar to the [Fe_3S_4] ferredoxin, the signal disappears in the presence of NaCl and is replaced by a broad peak similar to the peak observed for [Fe_3S_4] ferredoxin in the presence of NaCl. The salt effect on the [Fe_4S_4] ferredoxin was not investigated by a titration experiment, but it is assumed to follow a similar pattern.

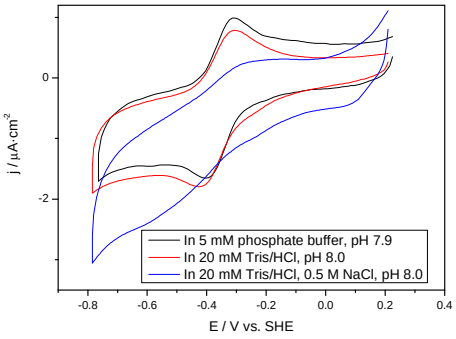

Figure 5.6: Cyclic voltammograms of 45 µM *P. furiosus* [Fe_4S_4] ferredoxin with 5 mM neomycin in different buffers as indicated, scan rate = 5 mV/s.

Table 5.2: Redox parameters of *P. furiosus* [Fe_4S_4] ferredoxin in the presence of neomycin in different buffers at 5 mV/s. Potentials are given in mV vs. SHE. The results from previous studies outside the glove box are given for comparison.

	E_a	E_c	$E^{0'}$	ΔE_p	$E_{p/2}$
5 mM phosphate buffer, pH 7.9	-319	-392	-356	73	56
20 mM Tris/HCl, pH 8.0	-306	-412	-359	106	68
Outside glove box, 5 mM phosphate buffer, pH 7.8 [71]	-341	-415	-378	74	

The parameters of the voltammograms in Figure 5.6 are given in Table 5.2 along with data from experiments outside the glove box [71]. The formal potentials are slightly higher in the new experiments inside the glove box and closer to the values obtained by Armstrong et. al. [69]. The signal to noise ratio in both buffers, though, is much better for the experiments inside the glove box and the signal is stable at significantly higher scan rates; up to 200 mV/s compared to maximum 20 mV/s for experiments performed outside the glove box, both in the experiments in my M. Sc. thesis [71] and in the result published by Armstrong et. al [69]. The signals to noise ratios are significantly better than any of the previously published voltammograms of the [Fe_4S_4] ferredoxin [31, 69, 70, 71] most likely due to less interference from oxygen. The formal potentials are very similar in phosphate buffer and Tris/HCl. The peak-peak separation is larger and the peaks broaden slightly in Tris/HCl, indicating that the reaction is slower in Tris/HCl.

The increased peak-peak separation, suggested to be caused by incorporation of Ag^+, observed for the [Fe_3S_4] ferredoxin in the previous section is not observed in the voltammograms of the [Fe_4S_4] ferredoxin. This suggests that the [Fe_4S_4] ferredoxin is stable in this system with the Ag/AgCl reference electrode and Ag^+ is incorporated in this cluster.

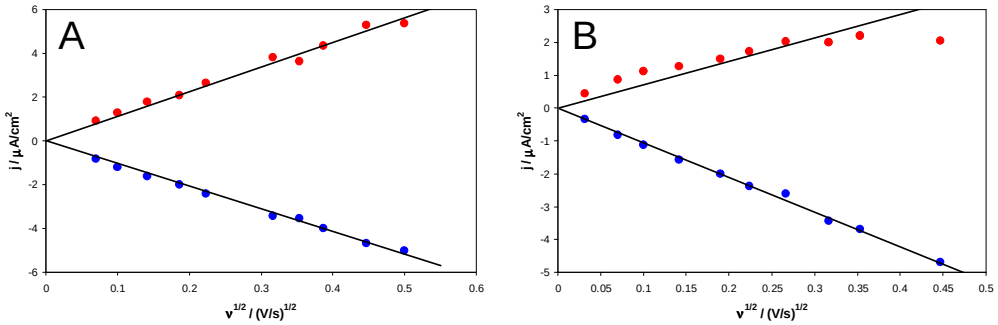

Figure 5.7: Peak current densities plotted versus the square root of the scan rate. A) In 5 mM phosphate buffer, pH 7.9, B) In 20 mM Tris/HCl, pH 8.0. ● = Anodic peak current density, ● = Cathodic peak current density.

The kinetic effects were studied by scanning at various scan rates. Figure 5.7 shows the peak current densities plotted versus the square root of the scan rate. The somewhat linear correlation is as expected for diffusion controlled systems. The average diffusion constants were determined from the slopes to $8.1 \cdot 10^{-7}$ cm^2/s in phosphate buffer and $5.6 \cdot 10^{-7}$ cm^2/s in Tris/HCl. The apparent rate constants were determined according to equation 4-7, chapter 4.1.3 to $1.1 \cdot 10^{-3}$ cm/s in phosphate buffer and $2.4 \cdot 10^{-4}$ cm/s in Tris/HCl buffer. According to these numbers, the protein diffuses more slowly and the rate of the electron transfer is also slower in Tris/HCl. The differences likely arise from the differences in ionic strength and pH between the Tris/HCl and phosphate buffer systems. The rate constants for the $[Fe_4S_4]$ have not been published previously, but the constants determined are in the range of what has been published for the $[Fe_3S_4]$ ferredoxin [67].
Addition of cysteine did not induce major changes in the voltammograms in neither of the buffers.

5.5 Electrochemical studies of ancient ferredoxins

5.5.1 Introduction

Other members of the Metalloprotein Group have carried out extensive studies on ancient ferredoxins. This section describes the electrochemical characterization of the proteins. The proteins will only briefly be presented here. Reference must be given to the Ph.D. theses of Signe Smedegaard Helt [66] and Hanne Nørgaard [75] for a detailed description of the previous characterization of the proteins. The work focuses on two proteins; one termed the last common ancestor (of iron-sulfur proteins), LCA ferredoxin, and one termed the origin of iron-sulfur proteins, Ori-ISP. Ori-ISP consists of a small peptide with four cysteine sites. The holo-protein is believed to form a dimer carrying two $[Fe_4S_4]$ clusters. Ori-ISP is extremely sensitive to oxygen and unstable. LCA ferredoxin can roughly be described as two Ori-ISP amino acid chains linked by a small peptide insertion forming a protein chain with eight cysteines and the protein is believed to carry two $[Fe_4S_4]$ clusters. A minor fraction of the protein carries one $[Fe_4S_4]$ cluster and one $[Fe_3S_4]$ cluster. LCA ferredoxin is more

stable than Ori-ISP, but is still very sensitive towards oxygen. Both LCA ferredoxin and Ori-ISP have overall negative charges.
The effect of different additives on the electrochemical properties of LCA ferredoxin was also tested in this study.

5.5.2 Experimental

The samples were prepared immediately before the electrochemical characterization by Hanne Nørgaard [10]. The samples of LCA ferredoxin were prepared either in 20 mM Tris/HCl, pH 8.0 or in 20 mM Tris/HCl, 0.5 M NaCl, pH 8.0. Ori-ISP was prepared in 20 mM Tris/HCl, 0.5 M NaCl, pH 8.0.
The electrodes were polished and mounted in the cell as described in chapter 4.3.2. Neomycin sulfate powder was added without further purification by dissolving in a small amount of protein solution and transferring this solution to the electrochemical cell. 5 mM concentrations were used.
The experiments were carried out at 27 °C.

5.5.3 Results and discussion

The concentration of LCA ferredoxin varied between 35 µM and 70 µM in the different experiments due to variations in the yields from purification that will not be discussed here. There were no differences between peaks observed at different protein concentrations.

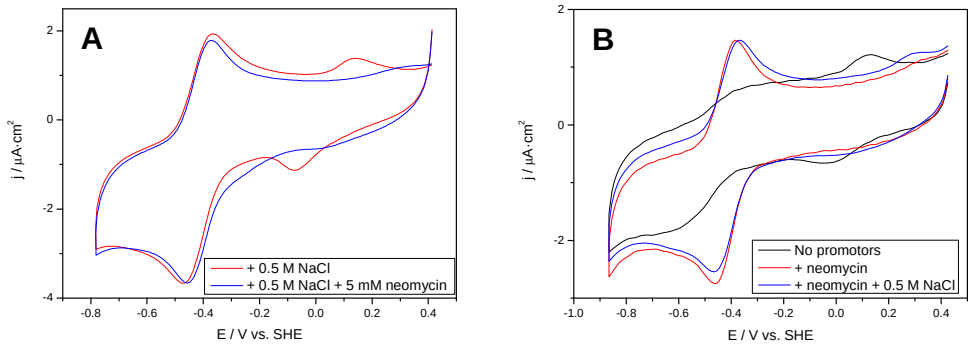

Figure 5.8: Cyclic voltammograms of LCA ferredoxin with/without neomycin and with/without NaCl as indicated in the figure legends. A) 53 µM, B) 35 µM, scan rate = 5 mV/s.

The voltammograms in the presence or absence of neomycin and with or without NaCl in the buffer are shown in Figure 5.8. They show some interesting effects. Two redox-couples appear in the voltammograms, a dominant signal at ~ -420 mV, and one broad signal at ~ 30 mV. The half peak widths of both redox couples suggest one-electron transfer. The signal at ~ -420 mV is attributed to the $[Fe_4S_4]^{+1/+2}$ redox couple and the redox couple at higher potentials is attributed to $[Fe_3S_4]^{0/+1}$. These results accord with the two-$[Fe_4S_4]$ cluster state of the protein being the predominant form and a minor fraction being the one-$[Fe_4S_4]$ cluster one-$[Fe_3S_4]$ cluster state. The ratio between the areas of the two sets of peaks do not, however, accord with the ratio

between the two forms determined from other methods [75], suggesting that the $[Fe_3S_4]$ cluster and the $[Fe_4S_4]$ cluster do not interact with the electrode surface in the same way. The redox parameters of the $[Fe_4S_4]$ signal are given in Table 5.3.

Table 5.3: Redox parameters of the $[Fe_4S_4]$ signal of LCA ferredoxin with and without neomycin and NaCl in 20 mM Tris/HCl, pH 8.0 at 5 mV/s. Potentials are given in mV vs. SHE.

	E_a	E_c	$E^{0'}$	ΔE_p
53 µM LCA ferredoxin + 0.5 M NaCl	-371	-466	-418	96
53 µM LCA ferredoxin + 0.5 M NaCl + 5 mM neomycin	-381	-454	-418	73
35 µM LCA ferredoxin + 5 mM neomycin	-385	-459	-422	75
35 µM LCA ferredoxin + 5 mM neomycin + 0.5 M NaCl	-376	-459	-418	84

The appearances of peaks with different promoters are very interesting in the perspective of the studies of *P. furiosus* $[Fe_3S_4]$ and $[Fe_4S_4]$ ferredoxin. The $[Fe_4S_4]$ signal is observed in the presence of either NaCl or neomycin or both. The $[Fe_3S_4]$ signal, however, is only present in the absence of neomycin and is independent of NaCl. That is, to my knowledge, the first observation of neomycin blocking an electrochemical signal. This is a very different behavior compared with the *P. furiosus* ferredoxins, where neomycin had to be present in the solution for any redox signals to appear and NaCl hindered the observed redox couples. Neomycin has been suggested to bind strongly to the *P. furiosus* ferredoxin [67]. It is reasonable that binding to a different protein with a different surface has a different effect and could block the electrochemical signal.

The voltammograms were recorded at various scan rates to study the kinetic effects of the $[Fe_4S_4]$ signal. The $[Fe_3S_4]$ signal is too weak and only stable at too low scan rates to study the kinetic effects. The plots in Figure 5.9 show the dependence of the peak current density of the $[Fe_4S_4]$ signal on the square root of the scan rate. When only neomycin is present, Figure 5.9B, both the cathodic and anodic peak currents densities show a linear dependency in the measured range. However, the dependence is not linear for the anodic peak at the highest scan rates when both neomycin and NaCl is present, Figure 5.9C, nor when only NaCl is present, Figure 5.9A. The dependency is different for the anodic and cathodic peaks in Figure 5.9A and Figure 5.9C.

The peak-peak separation is 75 mV and independent of the scan rate when only neomycin is added, indicating a reversible reaction where the reaction is too fast for the rate constant to be determined (cf. chapter 4.1.3). The rate constant when only NaCl is added and when both neomycin and NaCl are added were determined by first determining the average diffusion constants from the plots in Figure 5.9 and then using equation 4-7, chapter 4.1.3. The rate constant in the presence of only NaCl was determined to $1.2 \cdot 10^{-3}$ cm/s and the rate constant was $1.6 \cdot 10^{-3}$ cm/s in the presence of both neomycin and NaCl. These results indicate that neomycin promotes fast electron transfer, whereas NaCl slows down electron transfer. The electron transfer rate constants determined are in the same range as for the *P. furiosus* $[Fe_4S_4]$ ferredoxin.

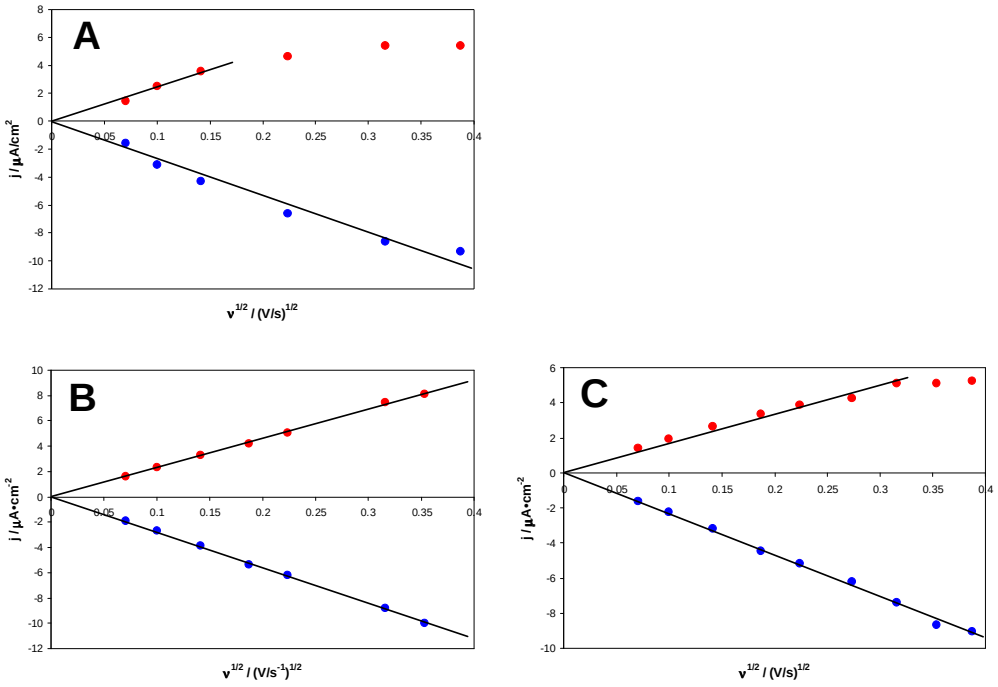

Figure 5.9: Peak current densities plotted versus the square root of the scan rate of LCA ferredoxin in 20 mM Tris/HCl. Conditions: A) 53 µM LCA ferredoxin + 0.5 M NaCl, B) 35 µM LCA ferredoxin + neomycin, C) 35 µM LCA ferredoxin + neomycin + 0.5 M NaCl. ● = Anodic peak current density, ● = Cathodic peak current density.

Ori-ISP was only studied in 20 mM Tris/HCl, 0.5 M NaCl, pH 8.0. The voltammograms with and without neomycin are shown in Figure 5.10. Figure 5.10A shows a very weak signal in the $[Fe_4S_4]^{+1/+2}$ range. Neomycin did not seem to have a promoting effect, rather the signal faded upon addition of neomycin. Figure 5.10B shows another signal at higher potentials. The signal at higher potentials is very large, broad, and asymmetric and the potentials change upon addition of neomycin.

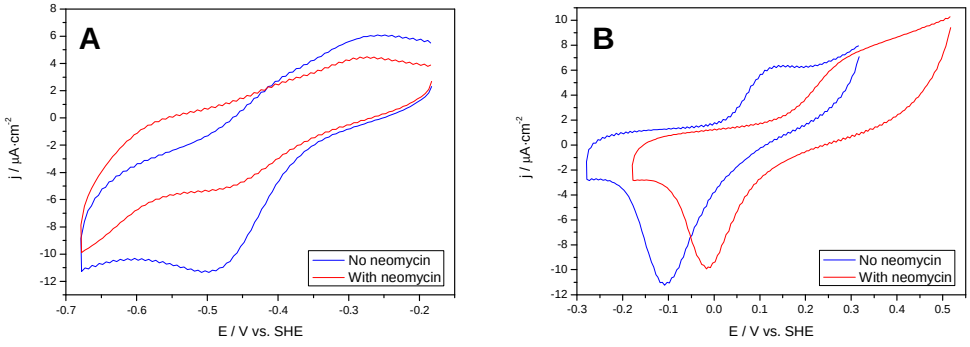

Figure 5.10: Cyclic voltammograms of 227 µM Ori-ISP in 20 mM Tris/HCl, pH 8.0 with and without neomycin as indicated A) in the lower potential window and B) in the higher potential window. Scan rate = 20 mV/s.

The color of the solution had changed after the experiments, questioning the integrity of the sample and the protein is most likely not stable towards the electrochemical conditions. The damping of the signal upon addition of neomycin could be due to

degradation of the protein and not an effect of neomycin. The signal at higher potentials could be due to oxidative degradation of the protein. Ori-ISP is an extremely sensitive protein, particularly towards oxidation [66, 75], rendering oxidative degradation probable.

5.6 Conclusion

Different ferredoxins have been investigated electrochemically under anaerobic conditions. The ferredoxins were studied in different buffers and the effect of promoters was tested.

Overall, the electrochemical setup in the glove box gave good redox signals. The signals for the *P. furiosus* $[Fe_4S_4]$ ferredoxin and the $[Fe_4S_4]$ LCA ferredoxin signal were well-defined and not very broad. The signal to noise ratio of the $[Fe_4S_4]$ ferredoxin is significantly better than for experiments outside the glove box. The $[Fe_3S_4]$ signals, however, were very broad and in the case of *P. furiosus* $[Fe_3S_4]$ ferredoxin particular the cathodic peak had shifted compared to previously published results. This is most likely due to incorporation of Ag^+ ions from the Ag/AgCl electrode into the cluster. Ag^+ ions did not seem to interfere with signals of the complete cuboidal $[Fe_4S_4]$ clusters. The current setup is therefore most appropriate for complete and stable clusters, but a leakage-free reference electrode would be desired for future experiments. The Ag/AgCl electrode used was also used for the experiments presented later in the report, since the incorporation of Ag^+ was only discovered recently.

The results illustrate that one has to be aware of factors such as salt and promoters when studying iron-sulfur proteins electrochemically. The buffer did not seem to have significant effect in the case of the *P. furiosus* ferredoxins and it was not tested for the LCA ferredoxin. Neomycin was necessary for any electrochemical signal of the *P. furiosus* ferredoxins, but blocked one of the signals from LCA ferredoxin. NaCl also has a huge effect on the signal as the *P. furiosus* signals disappeared in buffer with NaCl, but it seemed to promote slower electron transfer for LCA ferredoxin.

CHAPTER SIX

6 Studies of *Pyrococcus furiosus* $[CoFe_3S_4]$ Ferredoxin

6.1 Introduction

This chapter describes the synthesis, purification and characterization of *P. furiosus* ferredoxin with a heterometallic $[CoFe_3S_4]$ cluster.

The interest in iron-sulfur proteins with artificial heterometallic clusters is based on the enzymatic reactivity of heterometallic clusters. Moreover, the new class of heterometallic cuboidal clusters provides new means to explore the interactions between fragments of the cluster by investigating how incorporation of metals other than iron changes the properties of the iron-sulfur cluster and protein.

Synthesis of a $[CoFe_3S_4]$ cluster in *D. gigas* ferredoxin was the first reported formation of a synthetic, heterometallic cluster in a ferredoxin [37]. Since then the $[CoFe_3S_4]$ cluster has also been formed in *C. acidi urici* ferredoxin [76], aconitase [77] and *P. furiosus* ferredoxin [38]. The $[CoFe_3S_4]$ has thus been formed in more iron-sulfur proteins than any other of the new class of artificial heterometallic clusters in iron-sulfur proteins. The $[CoFe_3S_4]$ cluster in *P. furiosus* ferredoxin is of particular interest since Co is coordinated by the unusual aspartate ligand in this protein leading to differences in the EPR spectrum, and thereby differences in the electronic and magnetic properties, of this protein compared to the other $[CoFe_3S_4]$ ferredoxins [38].

In the previous study of the *P. furiosus* $[CoFe_3S_4]$ ferredoxin the protein was synthesized, desalted and studied with EPR spectroscopy and magnetic circular dichroism spectroscopy to establish the cluster type and magnetic properties of the cluster [38]. The protein was confirmed to exist in an EPR silent, diamagnetic $[CoFe_3S_4]^+$ state and an EPR active, paramagnetic $[CoFe_3S_4]^{2+}$ state. The midpoint potential of the transition between the two states was determined by EPR monitored redox titration. The reduced $[CoFe_3S_4]^+$ cluster was found to bind and release CN^- reversibly, whereas the oxidized $[CoFe_3S_4]^{2+}$ cluster broke down to the $[Fe_3S_4]$ cluster upon exposure to CN^-. In general, this study showed higher stability of the reduced cluster than the oxidized cluster [38].

This project includes the first multidisciplinary study of the *P. furiosus* $[CoFe_3S_4]$ ferredoxin with chromatographic purification, mass spectrometry, and electrochemical

characterization along with EPR spectrometry for comparison to previous studies.

6.2 Synthesis and purification of *P. furiosus* [$CoFe_3S_4$] ferredoxin

The protocol for synthesis of *P. furiosus* [$CoFe_3S_4$] ferredoxin was developed based on the previous reports on the formation of the [$CoFe_3S_4$] cluster in proteins [37, 38, 76, 77]. In these studies Co^{2+} was incorporated into the reduced [Fe_3S_4] ferredoxin. The excess of Co^{2+} to protein varies from 10 [38, 77] to 30 [37, 76]. In some of the reported procedures dithiothreitol, DTT, was added to the solution during incorporation of Co^{2+} [37, 76], while others add EDTA during the synthesis [38, 77]. The incubation time varies between 30 minutes and 12 hours. In all cases the incubation is followed by a desalting step and in some cases a crude ion-exchange step.
The protocol used in the present project was optimized with respect to time and DTT, but not with respect to EDTA.

6.2.1 Experimental

Synthesis without addition of DTT: All solutions were buffered with 20 mM Tris/HCl, pH 8.0 throughout the synthesis. A sample of 5 mg aerobically purified [Fe_3S_4] ferredoxin in 20 mM Tris/HCl, pH 8.0 was deoxygenated, sealed and transferred into the glove box. The sample was transferred to a round-bottomed flask and diluted to 2 ml. 215 µl 100 mM $Na_2S_2O_4$ (30 times excess) was added and the solution was incubated for 30 minutes for reduction of the [Fe_3S_4] ferredoxin. 6.3 mg of $Co(NO_3)_2 \cdot 6H_2O$ (30 times excess) was dissolved in 100 µl buffer and transferred to the round-bottomed flask and the resulting solution incubated for 4 hours with gentle stirring. The solution was then desalted on a PD-10 column equilibrated in 20 mM Tris/HCl, pH 8.0 by elution with the same buffer before loading on a Q Sepharose FF column. The column was washed with 2 CV 20 mM Tris/HCl, pH 8.0 and the protein eluded with 20 mM Tris/HCl, 0.5 M NaCl, pH 8.0 with gravity chromatography. The protein was then diluted 3 times and purified by HPLC (ÄKTAprime^{TM} plus) on a 20 mM Tris/HCl, pH 8.0 equilibrated 16/10 Source 30Q column. The protein was eluted by a linear gradient, 0.20 M NaCl to 0.35 M NaCl over 10 CVs, 6 ml/min. Collected fractions were concentrated using a Vivacell 70 with a 5000 MWCO membrane and UV-vis spectra recorded.
Synthesis with addition of DTT: The synthesis in the presence of DTT was carried out similarly to the synthesis without DTT, except that 1.1 mg DTT dissolved in 100 µl buffer (10 times excess) was added immediately before addition of $Co(NO_3)_2 \cdot 6H_2O$. The protocol for the purification was the same.

6.2.2 Results and discussion

There was no visible color chance upon addition of neither $S_2O_4^{2-}$ nor DTT in experiments where DTT was added. The color of the reaction mixture turned from brown to slightly greenish brown upon addition of Co^{2+}. There was no precipitation in the reaction flask. One brown band was eluted from the PD-10 column and no other

colored species were observed on this column. A brown band was also eluted from the Q Sepharose FF column, while another brown band remained on the column. In experiments without DTT, this band could be removed by washing the column in a weakly acidic solution with a small amount of H_2O_2. The band could not be removed when DTT had been used and the column had to be discarded.

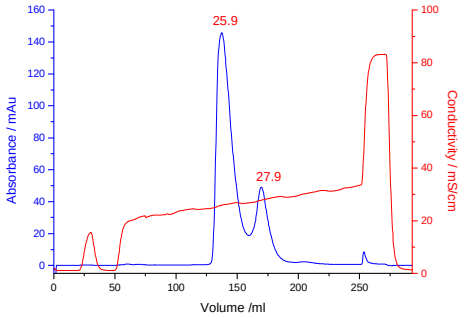

Figure 6.1: Chromatogram of purification of *P. furiosus* [$CoFe_3S_4$] ferredoxin on a 16/10 Source 30Q column when DTT was not added during the synthesis. The blue line indicates the absorption at 280 nm and the red line the conductivity gradient. The red numbers indicate the conductivities at the absorption maxima.

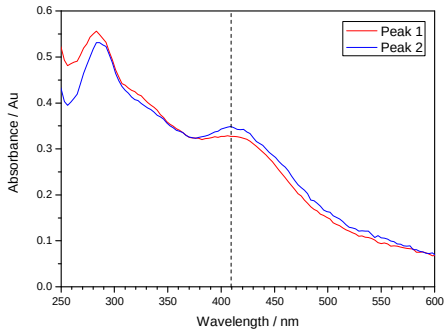

Figure 6.2: UV-vis spectra of the eluted peaks from the purification of *P. furiosus* [$CoFe_3S_4$] ferredoxin when DTT was not used. The sample identity is given in the legend. The dashed line marks the absorbance at 408 nm.

A chromatogram for the synthesis in the absence of DTT is shown in Figure 6.1. Two peaks are seen at conductivities similar to the purification of a mixture of [Fe_4S_4] and [Fe_3S_4] ferredoxin (chapter 5.2, Figure 5.1). The first and largest peak elutes at the same conductivity as [Fe_4S_4] ferredoxin and the second peak at the conductivities where [Fe_3S_4] ferredoxin elutes. The ratio of the second peak compared to the first peak increased when the reaction mixture was incubated for 3 hours or less, but the ratios did not change significantly for incubation times longer than 4 hours. 4 hours was therefore used in the protocol. Figure 6.2 shows spectra of the concentrated fractions from each peak. These are compared to the spectra of the [Fe_3S_4] and [Fe_4S_4] ferredoxins in chapter 5.2, Figure 5.2. The spectrum of the second peak shows the characteristic absorption maximum at 408 nm of the [Fe_3S_4] ferredoxin and these fractions are therefore attributed to [Fe_3S_4] ferredoxin. The spectrum of the first peak

is more flat in the 390-408 nm range extending the shoulder to higher wavelengths than the [Fe_4S_4] ferredoxin. The first peak is attributed to the [$CoFe_3S_4$] ferredoxin as confirmed by the characterization of the products in section 6.4.

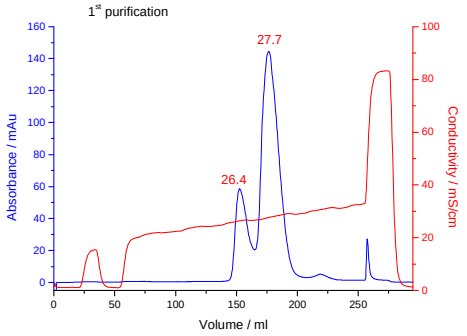

Figure 6.3: Chromatogram of purification of *P. furiosus* [$CoFe_3S_4$] ferredoxin on a 16/10 Source 30Q column when DTT was added during the synthesis. The blue line indicates the absorption at 280 nm and the red line the conductivity gradient. The red numbers indicate the conductivities at the absorption maxima.

The chromatogram in Figure 6.3 shows the purification when DTT was added during the synthesis. In this case the ratio between the two peaks is opposite that for experiments without DTT with the second peak being the largest. The spectra of the concentrated fractions are shown in Figure 6.4. The peak 1 spectrum is similar to the peak 1 spectrum in Figure 6.2 indicating that these two samples consist of the same species, suggested to be the [$CoFe_3S_4$] ferredoxin. The spectrum of peak 2, however, is very different without a peak or shoulder in the 390-408 nm range. The peak 2 spectrum is similar to the bleached spectra observed for reduced ferredoxins. This suggests that the main part of this peak is not oxidized [Fe_3S_4] ferredoxin as in the experiment without DTT, but instead arises from reduced species.

These chromatograms and UV-vis spectra suggest formation of the oxidized $[CoFe_3S_4]^{2+}$ cluster when the synthesis is carried out in the absence of DTT, but formation of the reduced $[CoFe_3S_4]^{+}$ cluster when the synthesis was carried out in the presence of DTT. The effects of reduction and oxidation were therefore tested as described below.

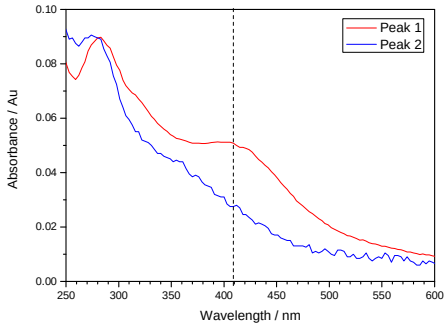

Figure 6.4: UV-vis spectra of the eluting peaks from the purification of *P. furiosus* [$CoFe_3S_4$] ferredoxin when DTT was used. The sample identity is given in the legend. The dashed line marks the absorbance at 408 nm.

6.3 Reduction and oxidation of *P. furiosus* [$CoFe_3S_4$] ferredoxin

Since the results of the purification suggested formation of either oxidized or reduced states of the [$CoFe_3S_4$], it was attempted to reduce and oxidize samples proposed to contain the different oxidation states of the [$CoFe_3S_4$] ferredoxin.

A peak 1 sample from synthesis without DTT, suggested in the previous section to contain oxidized $[CoFe_3S_4]^{2+}$ ferredoxin, was reduced with $S_2O_4^{2-}$. A peak 2 sample from the synthesis with addition of DTT, assumed to contain reduced $[CoFe_3S_4]^{+}$ ferredoxin, was oxidized in air.

6.3.1 Experimental

Reduction of [$CoFe_3S_4$] ferredoxin: A purified and concentrated sample of peak 1 fractions from the [$CoFe_3S_4$] ferredoxin synthesis was left in the glove box overnight. Half of the sample was reduced with 10 times excess of $Na_2S_2O_4$ and incubated for 1 hour before re-purification by HPLC as described above. The other half was re-purified without reduction as a reference.

The anaerobic chamber with an inlet for N_2 to add pressure to the Vivacell 70 was not available at the early stage in the project when the reduction experiment was carried out. The samples were instead concentrated by transferring the eluted fraction to the Vivacell 70 inside the glove box, taking the Vivacell 70 out of the glove box to add pressure and transferring the Vivacell 70 back to the glove box after concentration.

Oxidation of products from synthesis with DTT: Un-concentrated peak 2 fractions from the synthesis with DTT were transferred to a polypropylene tube which was then taken out of the glove box. The tube was opened to allow air into the tube, closed and turned up-side down a few times. The solution was oxidized for 30 minutes, and the tube turned every 5 minutes. The sample was then diluted twice with 20 mM Tris/HCl, pH 8.0 and re-purified according to the HPLC purification protocol.

The anaerobic chamber with the N_2 inlet was available for the oxidation experiment.

6.3.2 Results and discussion

The chromatograms in Figure 6.5 show the re-purification of peak 1 samples without (A) and with (B) reduction with $S_2O_4^{2-}$. Peak 1 as the main component in the chromatogram of the un-reduced sample, but a significant fraction of peak 2 is also present. The peak 2 fractions could either arise from the overlap of the two peaks in the previous purification or from breakdown of the assumed [$CoFe_3S_4$] ferredoxin in peak 1 to [Fe_3S_4] ferredoxin in peak 2 (discussed in section 6.5). After reduction, Figure 6.5B, peak 2 becomes the major component. This suggests that reduced [$CoFe_3S_4$] elutes in this peak too. This chromatogram has 2 additional peaks. One very sharp peak arising from $S_2O_4^{2-}$ appears early in the chromatogram and a small subsequent peak is observed after peak 2. The latter is suggested to arise from reduced [Fe_3S_4] ferredoxin. This pattern of eluting peaks after reduction was independent of whether the initial synthesis had been carried out in the absence or presence of DTT. The UV-vis spectrum of the reduced sample before re-purification is dominated by the $S_2O_4^{2-}$

spectrum and does not reveal much about the state of the proteins. It was not possible to measure the spectrum of the collected fractions after re-purification of the reduced sample, since the concentration of the eluted fractions was too low for the Nanodrop spectrophotometer and the sample seemed to be oxidized during the concentration in the Vivacell.

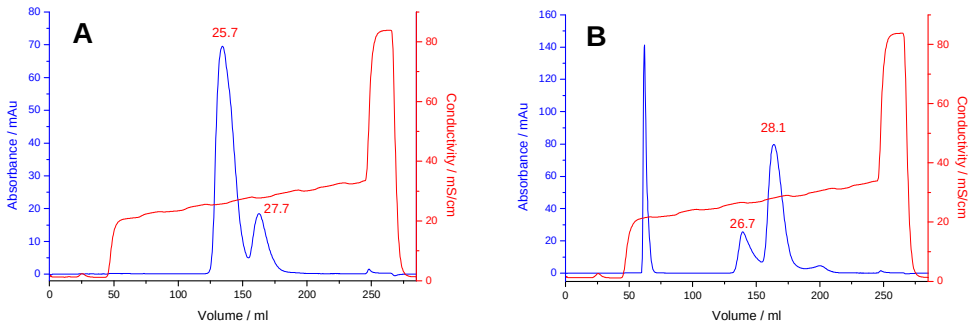

Figure 6.5: Chromatograms of re-purification of Peak 1 A) without reduction, B) after reduction with $S_2O_4^{2-}$. The blue lines indicate the absorption at 280 nm and the red lines the conductivity gradient. The red numbers indicate the conductivities at the absorption maxima.

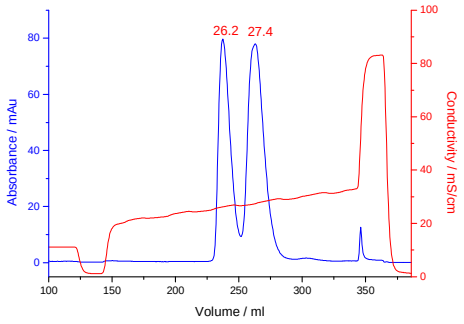

Figure 6.6: Chromatogram of re-purification of peak 2 after oxidation. The blue lines indicate the absorption at 280 nm and the red lines indicate the conductivity gradient. The red numbers indicate the conductivities at the absorption maxima.

The chromatogram after oxidation of peak 2 after synthesis in the presence of DTT (original chromatogram in Figure 6.3) is given in Figure 6.6. The chromatogram shows formation of the peak 1 species. The spectrum of these peak fractions was similar to the spectrum of peak 1 fractions in Figure 6.2 and Figure 6.4. This suggests that the bleached species eluting in the chromatogram of the purification after using DTT can be oxidized to form peak 1 species.

All in all the reduction and oxidation experiments along with the synthesis experiments suggest that peak 1 consist of oxidized [$CoFe_3S_4$] ferredoxin and peak 2 consist of oxidized [Fe_3S_4] ferredoxin when the synthesis is carried out in the absence of DTT, but also that peak 2 can contain some reduced [$CoFe_3S_4$] when the synthesis was carried out with DTT. The reduced [$CoFe_3S_4$] cannot be separated from [Fe_3S_4] ferredoxin and synthesis will therefore have to include an oxidation step when the synthesis is carried out with DTT to gain decent yields of pure [$CoFe_3S_4$] ferredoxin. It was therefore decided not to use DTT in the final protocol.

The molar absorptivity of [Fe_4S_4] ferredoxin, 17000 $M^{-1}\cdot cm^{-1}$ at 390 nm, was used for concentration estimations of peak 1 in the characterization studies. Peak 2 is treated as [Fe_3S_4] ferredoxin. The yield of [$CoFe_3S_4$] ferredoxin was 1.7 mg from 5 mg [Fe_3S_4] ferredoxin after purification and concentration when DTT was not used.

6.4 Mass spectrometric characterization of *P. furiosus* [$CoFe_3S_4$] ferredoxin

The purified products of the synthesis of [$CoFe_3S_4$] ferredoxin were characterized by mass spectrometry to confirm the synthesis of the desired heterometallic cluster. The [Fe_3S_4] ferredoxin used for the synthesis was also studied.
The mass spectrometric experiments were carried out in cooperation with Ph.D. student Maja Martic, who received the purified and concentrated samples and undertook the desalting procedure and the actual mass spectrometric measurements.

6.4.1 Experimental

Samples for mass spectrometry were prepared from concentrated samples of A) [Fe_3S_4] ferredoxin before incorporation of Co^{2+}, B) a sample containing peak 1, and C) a sample containing peak 2. The synthesis for the peak 1 and peak 2 samples was carried out without DTT. The purified products were analyzed without further oxidation or reduction.
The samples were desalted on Micro Bio-Spin columns (Bio-Rad) into 100 mM NH_4CH_3COO and diluted to 20 µM protein concentration with 100 mM NH_4CH_3COO.
Data acquisition and analysis were performed using a mass spectrometer with a nano-electrospray ionization source in negative ion mode and a time-of-flight analyzer (LCT Premier, Waters).

6.4.2 Results and discussion

When doing mass spectrometry of metalloproteins, one has to take into account the charge of the cluster, since the deconvolution programs for mass spectrometers assume that all charges arise from protonation or deprotonation. This assumption is often not correct for metalloproteins, since metal centres often are charges. It is therefore necessary to subtract or add the mass of protons to adjust the mass to the observed mass in the mass spectrum (see [78] for further details on this). Disulfide bridge cysteines also have to be taken into account since they are deprotonated, but not charged, thus giving an observed mass of 2.02 less than expected from standard molecular mass calculations. Table 6.1 gives the expected masses of *P. furiosus* ferredoxin with clusters of interest and an intact disulfide bridge.

Table 6.1: Expected masses of *P. furiosus* ferredoxin with an intact disulfide bridge and clusters of interest.

Cluster in *P. furiosus* ferredoxin:	Molar mass (g/mol)	Adjustment for charge on cluster	Expected observed mass in mass spectrum (g/mol)
$[Fe_3S_4]^0$	7460.86	-	7460.86
$[Fe_3S_4]^+$	7460.86	-1.01	7459.85
$[Fe_4S_4]^+$	7516.71	-1.01	7515.70
$[Fe_4S_4]^{2+}$	7516.71	-2.02	7514.69
$[CoFe_3S_4]^+$	7519.79	-1.01	7518.77
$[CoFe_3S_4]^{2+}$	7519.79	-2.02	7517.76

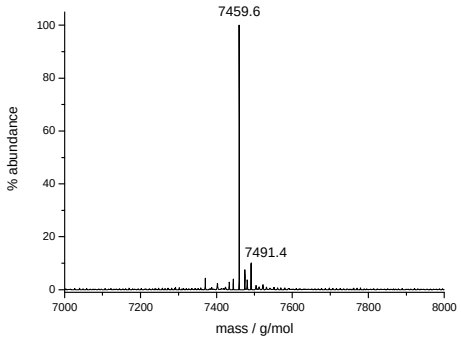

Figure 6.7: Mass spectrum of *P. furiosus* [Fe_3S_4] ferredoxin before incorporation of Co^{2+}. Protein concentration = 20 µM in 100 mM NH_4CH_3COO.

Figure 6.7 shows the mass spectrum of the sample of *P. furiosus* [Fe_3S_4] ferredoxin used for the synthesis. The observed mass of major part of the sample is 7459.6 g/mol confirming that this is indeed the $[Fe_3S_4]^+$ ferredoxin.

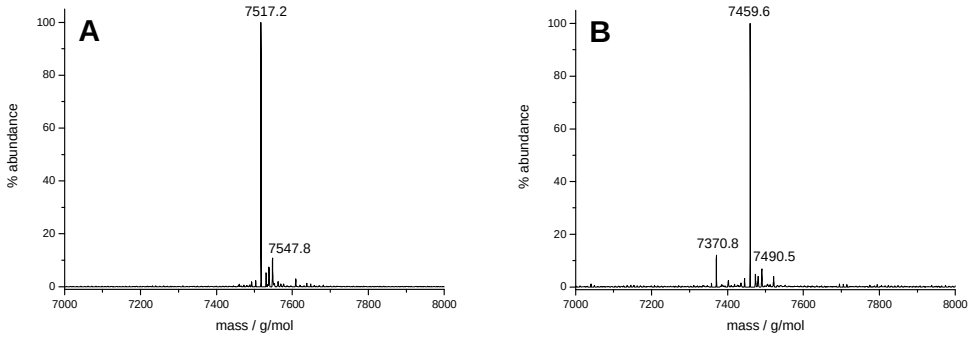

Figure 6.8: Mass spectra of A) the sample containing peak 1, B) the sample containing peak 2. Protein concentration = 20 µM in 100 mM NH_4CH_3COO in both cases.

The mass spectra of the products after the final purification are shown in Figure 6.8. The spectrum of the first peak is dominated by species with a mass of 7517.2 g/mol close to the expected mass of *P. furiosus* ferredoxin with a $[CoFe_3S_4]^{2+}$ cluster, supporting that this peak is indeed the oxidized [$CoFe_3S_4$] ferredoxin as assumed based on the chromatograms. There are no traces of [Fe_3S_4] or [Fe_4S_4] ferredoxin in this sample. The major peak in the mass spectrum of peak 2 has the same mass as the

$[Fe_3S_4]^+$ ferredoxin in Figure 6.7 indicating that this sample mainly consists of oxidized $[Fe_3S_4]$ ferredoxin.

The mass spectrometric analysis confirms that when the synthesis is carried out without DTT the two peaks in the chromatogram (Figure 6.1) consist of oxidized $[CoFe_3S_4]$ ferredoxin and $[Fe_3S_4]$ ferredoxin respectively. It is worth noticing that the protein is synthesized with the oxidized $[CoFe_3S_4]^{2+}$ cluster in this synthesis since the previously reported synthesis of the *P. furiosus* $[CoFe_3S_4]$ ferredoxin gave the reduced $[CoFe_3S_4]^+$ cluster as the product [38]. The previous synthesis was carried out at pH 6.3 in the presence of 2 mM $S_2O_4^{2-}$ and the protein was only purified by desalting to Tris/HCl, pH 7.8 with $S_2O_4^{2-}$ [38]. The continued presence of $S_2O_4^{2-}$ likely keeps the protein in the reduced state. The previous reports also state the $[CoFe_3S_4]^+$ ferredoxin is readily degraded to $[Fe_3S_4]^+$ ferredoxin upon oxidation without excess Co^{2+} [38]. This was not observed here, where the oxidized $[CoFe_3S_4]^{2+}$ ferredoxin seemed fairly stable (cf. the next section) and no $[Fe_3S_4]$ ferredoxin is observed in the mass spectrum of peak 1. It is not clear why the $[CoFe_3S_4]^{2+}$ ferredoxin synthesized here is more stable than what has been reported earlier.

The products from synthesis with addition of DTT were not characterized by mass spectrometry.

6.5 Stability studies of *P. furiosus* $[CoFe_3S_4]$ ferredoxin

The stability of the purified oxidized $[CoFe_3S_4]^{2+}$ ferredoxin towards different storage conditions and time was tested.

6.5.1 Experimental

Samples of purified $[CoFe_3S_4]^{2+}$ ferredoxin were stored in 20 mM Tris/HCl, pH 8.0 under different conditions as listed:

A) Un-concentrated, stored in the glove box overnight (16 hours).
B) Concentrated and stored in the glove box overnight (18 hours).
C) Concentrated, frozen in liquid N_2, stored at -20 °C overnight and thawed.
D) Concentrated and stored in the glove box for 3 days.

The stability was tested by UV-vis spectrophotometry and by re-purifying the samples by HPLC according to the procedure used in 6.2.1.

6.5.2 Results and discussion

The chromatograms of re-purification of the stored samples are shown in Figure 6.9 and the UV-vis spectra are shown in Figure 6.10. The spectra of the un-concentrated sample (A) are not shown since the concentration was too low too see anything in the UV-vis spectra. Chromatogram A and C have small peak 2 fractions suggesting that a small fraction of the protein is degraded to $[Fe_3S_4]$ ferredoxin during the storage and also during the re-purification and binding to the column. Peak 2 is larger in chromatogram B and even larger in D, suggesting that a considerable part of the $[CoFe_3S_4]$ ferredoxin is broken down to $[Fe_3S_4]$ ferredoxin when stored for 3 days, but also that

most of the sample still remains as [$CoFe_3S_4$] ferredoxin. The UV-vis spectra of the overnight-stored samples, B and C, does not change significantly, but the spectrum of sample D show a significant decrease in absorbance suggesting major changes as also indicated in the chromatogram.

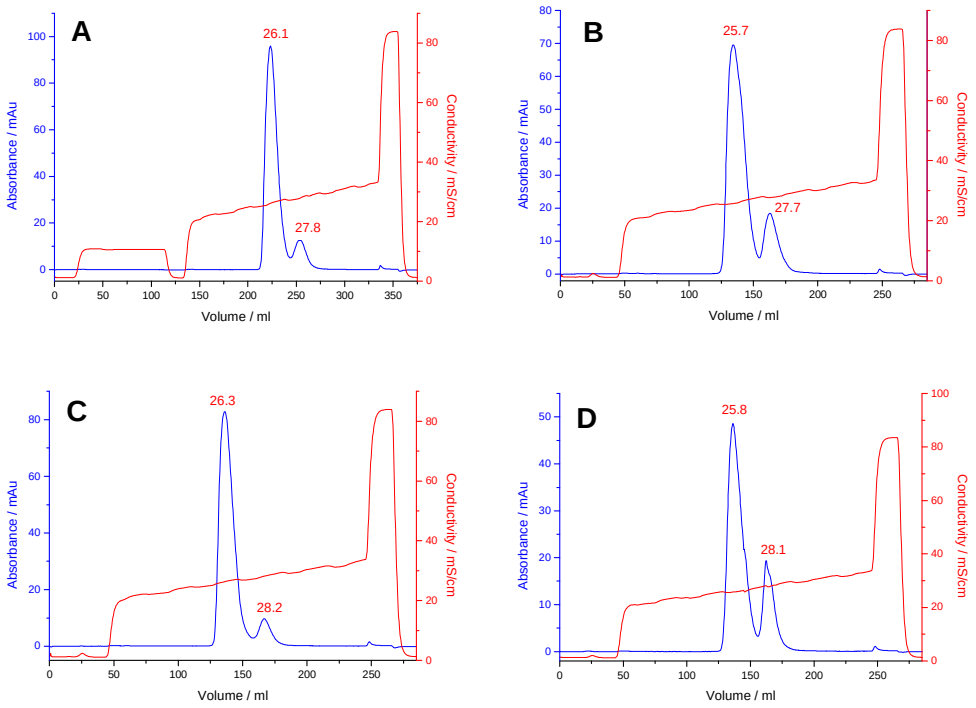

Figure 6.9: Chromatograms for re-purification of *P. furiosus* [$CoFe_3S_4$] ferredoxin after different storage conditions and time. A) Not concentrated, stored overnight in glove box, B) concentrated and stored in glove box overnight, C) concentrated, frozen and thawed, and D) concentrated and stored in the glove box for 3 days.

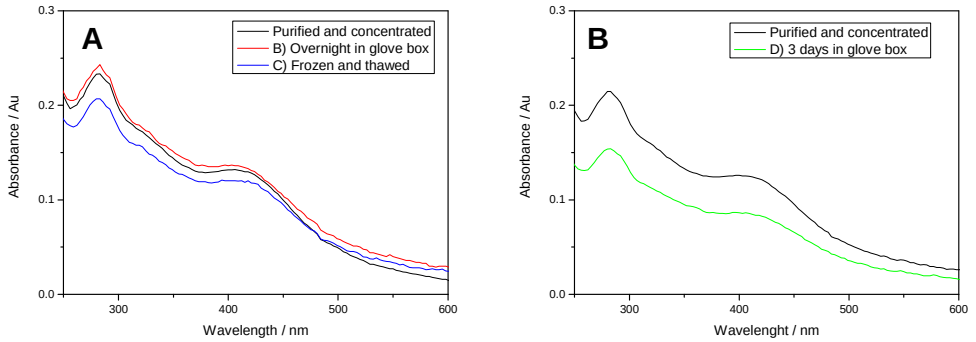

Figure 6.10: UV-vis spectra of [$CoFe_3S_4$] ferredoxin after different storage conditions as specified in the figure legends.

These studies show that 10-20 % of the [$CoFe_3S_4$] ferredoxin is broken down upon re-purification after storage overnight or after freezing and thawing. A more significant part of the protein has degraded after longer time storage. That means that one has to be aware of signs of [Fe_3S_4] ferredoxin in characterization experiments like electro-chemistry, where the experiments could not be carried out on the same day due to

time limitations. If the degradation of the cluster primarily occurs during the storage, one would expect to observe a contribution from [Fe_3S_4] ferredoxin in such characterization experiments. If the experiments do not show signs of [Fe_3S_4] ferredoxin, it suggests that the degradation mainly occurs during the re-purification and the interaction with the column material.

6.6 Electrochemical studies of *P. furiosus* [$CoFe_3S_4$] ferredoxin

The *P. furiosus* [$CoFe_3S_4$] ferredoxin was characterized electrochemically using the same setup described in chapter 4.3.2 and based on the previous studies of effects of buffers and promoters in chapter 5.
The results are compared to the previous determination of the redox potential by EPR-monitored redox titration by Finnegan et. al. [38].

6.6.1 Experimental

The electrochemical experiments were carried out the day following the purification.
The buffer of the purified protein sample was changed into 20 mM Tris/HCl, pH 8.0 by reducing the volume in a Vivacell 70 and diluting ~50 times with the desired buffer. This was repeated three times. The concentrations of the final samples were determined by UV-vis spectrophotometry.
The electrodes were polished, transferred into the glove box and mounted in the electrochemical cell as described in chapter 4.3.2.
Co^{2+} was added in the form of appropriate amounts of 20 mM Co^{2+}, prepared by dissolving $Co(NO_3)_2 \cdot 6H_2O$ in 20 mM Tris/HCl, pH 8.0 in experiments with excess Co^{2+}.
Neomycin sulfate powder was added to the solution without further purification by dissolving in a small volume of the protein solution and mixing this with the rest of the protein solution. Neomycin was used in 5 mM concentration.

6.6.2 Results and discussion

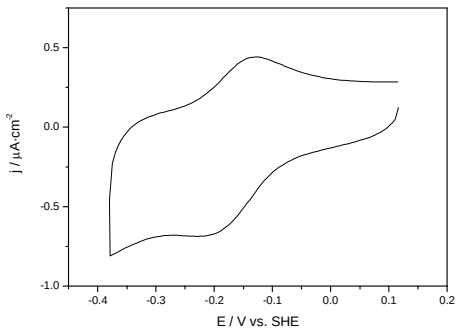

Figure 6.11: Cyclic voltammogram of 16 µM *P. furiosus* [$CoFe_3S_4$] ferredoxin in 20 mM Tris/HCl, pH 8.0 with 5 mM neomycin. Scan rate = 5 mV/s.

As for the *P. furiosus* [Fe_3S_4] and [Fe_4S_4] ferredoxins there was no electrochemical signal in the absence of neomycin. A well-defined redox pair appeared in the

voltammogram upon addition of neomycin as seen in Figure 6.11. The signal is attributed to the $[CoFe_3S_4]^{2+/+}$ redox couple. The voltammograms were stable up to 200 mV/s. The signal was also stable towards several cycles as the signal was similar at the start of the experiment and after several cycles at various scan rates.The redox parameters of the voltammogram at 5 mV/s are given in Table 6.2 and compared to the parameters of the $[Fe_3S_4]$ and $[Fe_4S_4]$ ferredoxin determined in chapter 5. The formal potential was determined to -177 mV vs. SHE, i.e. slightly lower than the potential determined from EPR monitored redox titration (-163 mV [38]). That is 182 mV higher than for the *P. furiosus* $[Fe_4S_4]$ ferredoxin under similar conditions (chapter 5.4), which is also the same difference between the redox potentials of the $[Fe_4S_4]$ and $[CoFe_3S_4]$ ferredoxin as determined by titration [38].

Table 6.2: Redox parameters of *P. furiosus* $[CoFe_3S_4]$ ferredoxin in the presence of neomycin in 20 mM Tris/HCl, pH 8.0 at 5 mV/s. The results from the studies of *P. furiosus* $[Fe_3S_4]$ and $[Fe_4S_4]$ ferredoxin in chapter 5 are given for comparison. Potentials are given in mV vs. SHE.

	E_a	E_c	$E^{0'}$	ΔE_p	$E_{p/2}$
$[CoFe_3S_4]$ ferredoxin in 20 mM Tris/HCl, pH 8.0	-140	-213	-177	73	63
$[Fe_3S_4]$ ferredoxin in 20 mM Tris/HCl, pH 8.0	-146	-315*	-231*	169	87
$[Fe_4S_4]$ ferredoxin in 20 mM Tris/HCl, pH 8.0	-306	-412	-359	106	68

*The cathodic peak potential of $[Fe_3S_4]$ ferredoxin was shifted, possibly due to incorporation of Ag^+ as discussed in chapter 5.3.

The formal potential has been reported to be close to the formal potential of *P. furiosus* $[Fe_3S_4]$ ferredoxin [38]. That is not observed when comparing these voltammograms to the voltammograms of *P. furiosus* $[Fe_3S_4]$ ferredoxin in chapter 5.3. As noted in chapter 5.3 the cathodic peak potentials of the $[Fe_3S_4]$ ferredoxin shifts, possibly due to incorporation of Ag^+, resulting in a lower formal potential and a large peak-peak separation. The large peak-peak separation is not observed for the $[CoFe_3S_4]$ ferredoxin. This confirms that the signal reported here does not arise from $[Fe_3S_4]$ ferredoxin from break-down of the $[CoFe_3S_4]$ cluster. This also suggests that Ag^+ does not replace Co^{2+} in the cluster indicating that the $[CoFe_3S_4]$ cluster is stable towards these experimental conditions.

The formal potential of the $[CoFe_3S_4]^{2+/+}$ redox couple cannot be directly compared to the formal potential of $[Fe_3S_4]$ ferredoxin determined in the same setup in chapter, due to the incorporation of Ag^+ in the $[Fe_3S_4]$ cluster observed for $[Fe_3S_4]$ ferredoxin. It is instead compared to the formal potential of $[Fe_3S_4]^{1+/0}$ redox couple in the previous study by members of the Nanoscale Chemistry group [67]. This potential, -186 mV vs. SHE, is close to the formal potential of the $[CoFe_3S_4]$ ferredoxin in Table 6.2. The results of previous reports suggest that the $[CoFe_3S_4]$ cluster can be rationalized as a Co^{2+} fragment coupled to a $[Fe_3S_4]^{0/-1}$ fragment [38, 39]. According to this, the $[Fe_3S_4]$ fragment cycle between two different redox couples in the $[CoFe_3S_4]$ and $[Fe_3S_4]$ ferredoxins. The $[Fe_3S_4]$ fragment between the $[Fe_3S_4]^0$ and $[Fe_3S_4]^-$ oxidation states in $[CoFe_3S_4]$ ferredoxin, while the $[Fe_3S_4]$ ferredoxin cycle between the $[Fe_3S_4]^+$ and $[Fe_3S_4]^0$ states. It is intriguing that the formal potentials of the $[CoFe_3S_4]$

and [Fe_3S_4] ferredoxins are so close if they arise from different [Fe_3S_4] redox couples. This suggests that insertion of Co^{2+} in the empty corner of the [Fe_3S_4] cluster stabilizes the reduced states on the cluster tremendously.

The formal potential of the [$CoFe_3S_4$] ferredoxin is 182 mV higher than the formal potential of the [Fe_4S_4] ferredoxin. The [Fe_4S_4] has also been rationalized as a $[Fe_3S_4]^{0/-}$ fragment coupled Fe^{2+}, similar to the model for other synthesized heterometallic cluster with non-iron heterometals [38]. According to this model and the observed formal potentials, incorporated of Co^{2+} stabilizes the reduced $[Fe_3S_4]^{-}$ significantly more than Fe^{2+} in the native [Fe_4S_4] ferredoxin. This is another interesting aspect of the ability of iron-sulfur clusters to tune the redox properties of relatively simple clusters.

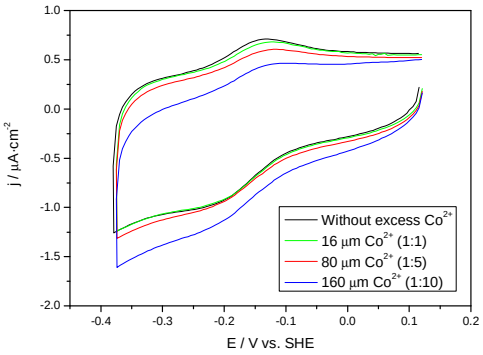

Figure 6.12: Cyclic voltammogram of 16 µM *P. furiosus* [$CoFe_3S_4$] ferredoxin in 20 mM Tris/HCl, pH 8.0 with 5 mM neomycin and excess Co^{2+} as indicated in the figure legend. Scan rate = 5 mV/s.

It was attempted to add Co^{2+} to the solution to see if this improved the already high stability of the electrochemical signal. The voltammograms after addition of excess Co^{2+} are shown in Figure 6.12. Excess Co^{2+} does not seem to have a positive effect, but rather an attenuating effect. The effect seems similar to the effect of NaCl on the voltammograms of *P. furiosus* [Fe_4S_4] and [Fe_3S_4] ferredoxins (see chapter 5).

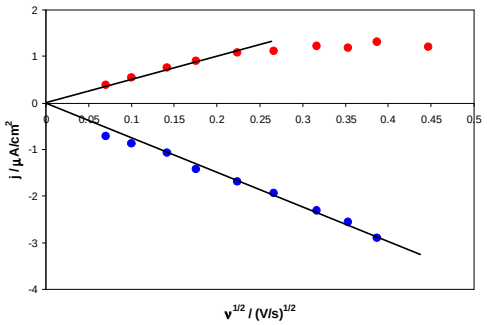

Figure 6.13: Peak current plotted versus the square root of the scan rate. ● = Anodic peak current density, ● = Cathodic peak current density. 16 µM *P. furiosus* [$CoFe_3S_4$] ferredoxin in 20 mM Tris/HCl, pH 8.0 with 5 mM neomycin and without excess Co^{2+}.

Figure 6.13 shows the peak current densities plotted versus the square root of the scan rate. The cathodic peak current varies linearly in the full scan range while the anodic

peak current only shows a linear dependence of the square root of the scan rate at lower scan rates and bends off at higher rates. This suggests a diffusion controlled system with different kinetics for the two electrode reactions. The two states could for example have different orientation on the electrode. The peak-peak separation was independent of the scan rate suggesting that the system is reversible and the rate constants for the electron transfer reaction could not be determined.

6.7 EPR spectroscopic studies of *P. furiosus* [$CoFe_3S_4$] ferredoxin

The purpose of the EPR spectroscopic studies was to compare the purified product of the synthesis to the previously published data on the [$CoFe_3S_4$] ferredoxin. The studies were also used to study the purity and as part of the stability studies.

The protein has been reported to be EPR active in the oxidized $[CoFe_3S_4]^{2+}$ state and EPR silent in the reduced $[CoFe_3S_4]^{+}$ state. The $[CoFe_3S_4]^{2+}$ cluster was observed to have a spin of ½ and the $[CoFe_3S_4]^{+}$ cluster spin $S = 1$ [38]. The spins were not further investigated in this study.

Samples for EPR measurements were prepared in our laboratories, and frozen and transported in liquid N_2. EPR spectra were measured at Delft University of Technology by Professor Wilfred R. Hagen during my visits to his laboratories.

6.7.1 Experimental

Three samples of [$CoFe_3S_4$] ferredoxin were prepared for EPR spectroscopy.

A) A sample of purified $[CoFe_3S_4]^{2+}$ ferredoxin
B) A sample of "re-oxidized" [$CoFe_3S_4$] ferredoxin. This sample was prepared from the collected fractions of reduced $[CoFe_3S_4]^{+}$ ferredoxin in Figure 6.5B. The sample was presumably oxidized during the up-concentration in the Vivacell 70 outside the glove box.
C) A sample of reduced $[CoFe_3S_4]^{+}$ ferredoxin. This sample was prepared by reduction of a fraction of sample A with $S_2O_4^{2-}$.

The samples were frozen, stored and shipped in liquid N_2 and the spectra were measured at 20-30 K under cooling with liquid He.

The instrumentation and data analysis software are described in chapter 4.3.3.

6.7.2 Results and discussion

The EPR spectra of the oxidized $[CoFe_3S_4]^{2+}$ ferredoxin are shown in Figure 6.14. The spectrum in the wide range (A) has two features; a main signal centred at $g = 1.9$ and a broad peak at $g \approx 5.15$ arising from Co^{2+}. The main signal is shown in a narrower field range in Figure 6.14B with a simulation. The spectrum is simulated with *g*-values 1.937, 1.8515 and 1.8511. Eight hyperfine lines arise from interactions with Co^{2+} ($I = 7/2$). They were simulated with metal hyperfines 50, 8 and 8 gauss, widths of 18, 65 and 65 and *A*-strain with asymmetries in W_z of $B = -0.07$ and $C = -0.03$. The spectrum looks very similar to the spectrum reported previously [38] with similar parameters, though the simulation indicates a slightly more axial geometry.

The differences are so small that they can be attributed to the slightly different experimental conditions and it is concluded to be the same species as previously synthesized.

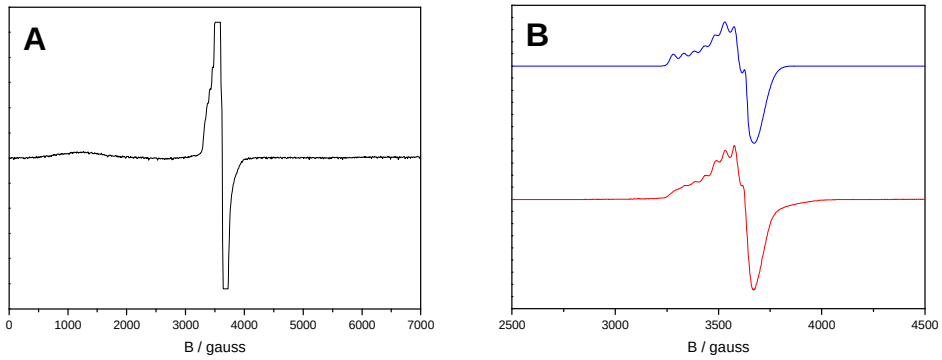

Figure 6.14: EPR spectra of 825 µM $[CoFe_3S_4]^{2+}$ ferredoxin in 20 mM Tris/HCl, pH 8.0, T = 30 K. A) Wide field range, ν = 9.3939 GHz, P = 4 dB, M = 6.3, G = $1.6 \cdot 10^5$. B) Narrower field range. Red trace: experimental, ν = 9.3938 GHz, P = 10 dB, M = 6.3, G = $1.6 \cdot 10^4$. Blue trace: simulation.

The spectra of the re-oxidized sample in Figure 6.15 shows the same features as the "original" oxidized sample, but the intensity is ~10 times smaller. This corresponds to the lower concentration of the protein. The spectrum shows no indications of either reduced or oxidized [Fe_3S_4] ferredoxin, indicating that the Co-containing protein is relatively stable and does not break down during the re-oxidation. The Co^{2+}-signal is still present. Finnegan et al. have also oxidized the protein aerobically, but in the presence of excess Co^{2+} to avoid oxidative degradation. According to the spectra of the re-oxidized sample in Figure 6.15, it is not necessary to add excess Co^{2+} to avoid degradation to [Fe_3S_4] ferredoxin during oxidation.

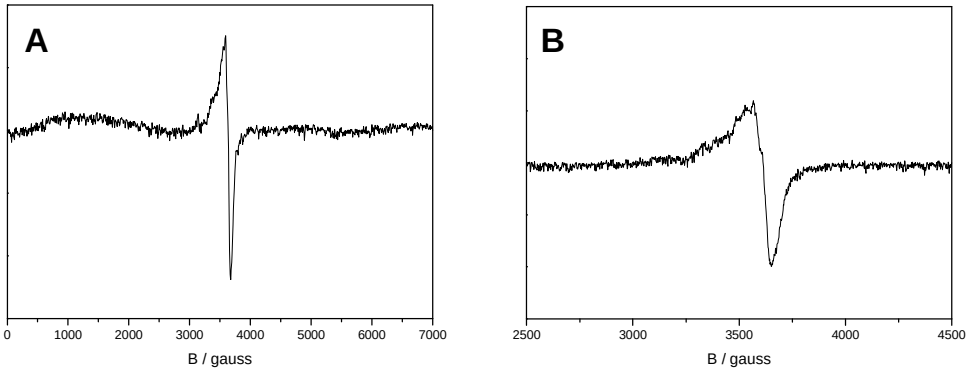

Figure 6.15: EPR spectra of 90 µM re-oxidized $[CoFe_3S_4]^{2+}$ ferredoxin in 20 mM Tris/HCl, pH 8.0, T = 30 K. A) Wide field range, ν = 9. 3919 GHz, P = 4 dB, M = 6.3, G = $1.6 \cdot 10^5$. B) Narrower field range. ν = 9.3938 GHz, P = 4 dB, M = 6.3, G = $1.6 \cdot 10^4$.

Figure 6.16 shows the spectrum of the reduced $[CoFe_3S_4]^+$ ferredoxin under similar experimental conditions as for the spectrum of the oxidized protein in Figure 6.14 as well as a comparison of the two spectra. The spectrum shows the same features as the oxidized spectrum, but the signal intensity is much, much lower. That indicates trace

amounts of oxidized $[CoFe_3S_4]^{2+}$ ferredoxin, suggesting that the reduction was not complete. As expected the signal from Co^{2+} has the same intensity. There is no signal from reduced $[Fe_4S_4]^{+}$ confirming that no trace amounts of $[Fe_4S_4]$ ferredoxin are eluted with the $[CoFe_3S_4]^{2+}$ ferredoxin in the purification.

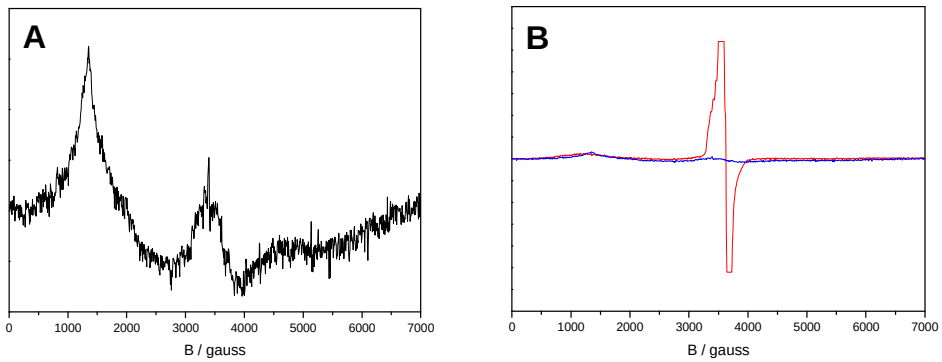

Figure 6.16: A) EPR spectrum of 825 µM reduced $[CoFe_3S_4]^{+}$ ferredoxin in 20 mM Tris/HCl, pH 8.0, T = 24 K, ν = 9.3933 GHz, P = 4 dB, M = 6.5, G = $1.6 \cdot 10^5$. B) Comparison of EPR spectra of reduced (blue trace) and oxidized (red trace) $[CoFe_3S_4]$ ferredoxin, experimental conditions given in this caption and the caption of Figure 6.14.

These studies have shown that the synthesized and purified $[CoFe_3S_4]^{2+}$ ferredoxin is similar to the previous studied protein and stable towards a reduction-oxidation cycle. None of the spectra showed any indications of $[Fe_3S_4]$ or $[Fe_4S_4]$ ferredoxin, proving that the $[CoFe_3S_4]$ ferredoxin is pure and does not break down during the experiments.

6.8 Conclusions

The *P. furiosus* ferredoxin with the heterometallic $[CoFe_3S_4]$ cluster has been synthesized and purified and characterized with mass spectrometry, electrochemistry and EPR spectroscopy.

The synthesis was carried out both without and with DTT added during the synthesis. The products of the purification when DTT was not used were confirmed by mass spectrometry to be a main fraction consisting of $[CoFe_3S_4]^{2+}$ ferredoxin and a smaller fraction of $[Fe_3S_4]^{+}$ ferredoxin. Mass spectrometry showed pure samples confirming good separation in the purification. When the synthesis was carried out with DTT a significant yield of reduced $[CoFe_3S_4]^{+}$ ferredoxin eluted with $[Fe_3S_4]^{+}$ ferredoxin and it was necessary to add a step for oxidation of $[CoFe_3S_4]^{+}$ ferredoxin to $[CoFe_3S_4]^{2+}$ ferredoxin for reasonable yields of pure $[CoFe_3S_4]$ ferredoxin. DTT was therefore not used in the optimized synthesis. Experiments with reduction with $S_2O_4^{2-}$ and oxidation in air showed changes in elution conductivity upon change in redox state of the cluster. The synthesis of the $[CoFe_3S_4]$ ferredoxin was confirmed with EPR spectroscopy. These studies also confirmed the redox state and purity of the synthesized product.

The oxidized $[CoFe_3S_4]^{2+}$ ferredoxin is the final product of these experiments, whereas the reduced $[CoFe_3S_4]^{+}$ ferredoxin has been the previously reported stable

product. The $[CoFe_3S_4]^{2+}$ ferredoxin has been reported to be unstable and readily break down to $[Fe_3S_4]$ ferredoxin in the absence of excess Co^{2+}. It did, however, seem rather stable in the present studies.

One well-defined pair of redox peaks was detected in the electrochemical characterization of *P. furiosus* $[CoFe_3S_4]$ ferredoxin in homogeneous solution at a graphite electrode in the presence of neomycin. The redox-couple was assigned to the $[CoFe_3S_4]^{2+/+}$ redox couple. The formal potential was determined to -177 mV versus SHE which accords with previous results. The reaction followed a reversible diffusion-controlled relation. Addition of excess Co^{2+} did not improve the electrochemical signal, but rather damp it.

This has been the first multidisciplinary study of the *P. furiosus* $[CoFe_3S_4]^{2+}$ ferredoxin including a detailed chromatographic study, confirming the synthesis of the desired product and characterizing the *P. furiosus* $[CoFe_3S_4]$ ferredoxin with mass spectrometry and EPR spectroscopy as well as electrochemistry.

CHAPTER SEVEN

7 Sulfonation of *Pyrococcus furiosus* Ferredoxin

7.1 Introduction

This chapter presents the procedure for sulfonation and purification of sulfonated *P. furiosus* ferredoxin. Mass spectrometric characterization of the sulfonated protein is also presented.

Sulfonation of ferredoxin and purification of the sulfonated protein is a step on the way to synthesis of the molybdenum-sulfur analogue of *P. furiosus* ferredoxin. As noted in chapter 3.4 the molybdenum-sulfur cluster cannot be incorporated into the protein by self-assembly and is therefore incorporated into the apo-protein (chapter 9). The apo-protein requires stabilization by sulfonation until the incorporation of the molybdenum-sulfur cluster.

The apo-protein is formed by eliminating the iron-sulfur cluster from the protein by addition of a weak acid as described in the next section. The native disulfide bridge is also broken by this procedure. That leaves five free cysteine thiolates which are likely to form disulfide bonds or react with oxygen. The thiolates of the apo-protein are therefore protected by sulfonation where sulfite groups are bonded to the thiolates. The sulfite protection groups are formed by addition of sulfite and 2-nitro-5-thiosulfobenzoate (NTSB) in the presence of urea [1]. The sulfite protection groups are later removed immediately before incorporation of the molybdenum-sulfur cluster as described in chapter 9.3.

The procedure for sulfonation and purification of sulfonated protein has been developed by other members of the Metalloprotein Chemistry Group. The sulfonated protein is very stable and the sulfonation and purification can be carried out under aerobic conditions [79].

7.2 Sulfonation and purification of sulfonated *P. furiosus* ferredoxin

7.2.1 Experimental

80-100 mg lyophilized *P. furiosus* ferredoxin was dissolved in 5 ml water and 2.2 ml

20% HCOOH was added. The solution was heated to 90 °C for ~30 minutes until the brown color was very faint. The solution was transferred to a beaker with 14.4 g urea with a small volume of water. The urea was dissolved with stirring and 1.13 g Na_2SO_3 was added. The pH of the solution was adjusted to 8.0 with NaOH before adding 8 ml 400 mM NTSB (prepared as described in [79]). The resulting orange solution was stirred for 3 hours at room temperature and at 4 °C overnight.

The solution was desalted by loading 6 ml pr. run on a HiPrep 26/10 Desalting column (ÄKTA^{TM} purifier 100) equilibrated in 0.15 M NH_4HCO_3. The sulfonated protein was eluted in the same buffer and the protein-containing fractions collected. The buffer was exchanged to 20 mM Tris/HCl, pH 8.0 by reducing the volume in a stirred Amicon cell with a YM-3 membrane (Millipore) and diluting 10 times with Tris/HCl, pH 8.0.

The desalted, sulfonated ferredoxin was purified by ion-exchange. The solution was divided into 6 portions which were purified separately on a 16/10 Source 30Q column (ÄKTA^{TM} purifier 100) equilibrated with 20 mM Tris/HCl, pH 8.0. The sulfonated protein was purified using a 20-48 % linear gradient of 20 mM Tris/HCl, 1 M NaCl, pH 8.0 over 10 CV.

The solution was desalted by ultrafiltration in a stirred Amicon cell with a YM-3 membrane (Millipore) and dilution with 0.15 M NH_3HCO_3. This was repeated three times. The resulting solution was diluted to 0.1 M NH_4HCO_3 with water, frozen as a thin film in a round-bottomed flask in an ethanol/water bath at -20 °C and lyophilized overnight. The lyophilized protein was stored in small tubes at -20 °C.

7.2.2 Results and discussion

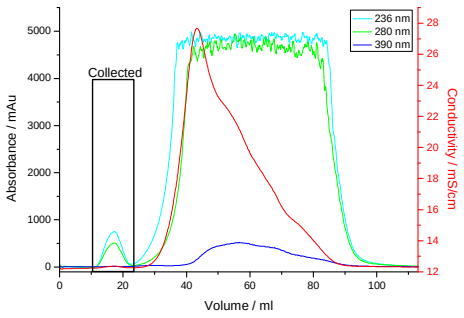

Figure 7.1: Chromatogram of desalting of sulfonated *P. furiosus* ferredoxin on a HiPrep 26/10 Desalting column. The turquoise, green and blue line indicates the absorption at 236, 280 and 390 nm, respectively, and the red line the conductivity. The collected fractions are marked.

A chromatogram for the desalting of sulfonated *P. furiosus* ferredoxin and the collected fractions is shown in Figure 7.1. The protein-containing peak from the desalting of the sulfonated *P. furiosus* ferredoxin is very small compared to the other peaks in the chromatogram, implying that other compounds are present in the solution. From the chromatogram the separation does, however, seem sufficient based on the baseline separation of peaks in the chromatogram. The other peaks are assigned

to the highly adsorbing modification reagents, primarily NTSB. The reagents stain the column yellow/orange and cannot be removed from the column even after cleaning with 0.1 M HCl and 1 M NaCl. A column dedicated to this purpose was therefore used.

Figure 7.2 shows a chromatogram of the ion-exchange purification of the sulfonated *P. furiosus* ferredoxin. The fractions containing the main peak are collected without the shoulder. The sulfonated *P. furiosus* ferredoxin has been found to elute in this peak by previous members of the Metalloprotein Chemistry Group. The identity of the protein was studied further below.

Typical yields were in the range of 90 mg from 100 mg holo-ferredoxin corresponding to approximately 90% (mol/mol).

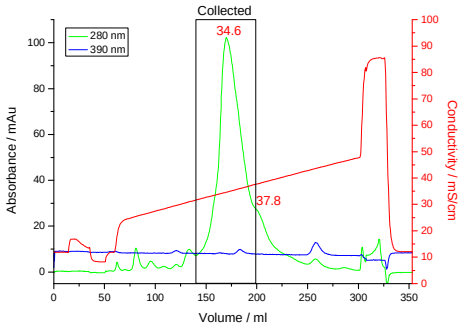

Figure 7.2: Chromatogram of purification by ion-exchange of sulfonated *P. furiosus* ferredoxin on a 16/10 Source 30Q column. The green and blue line indicates the absorption at 280 and 390 nm, respectively, and the red line the conductivity gradient. The red numbers indicate the conductivities at the absorption maxima. The collected fractions are marked.

7.3 Mass spectrometric characterization of sulfonated *P. furiosus* ferredoxin

The mass spectrometric experiments were carried out in cooperation with Ph.D. student Maja Martic, who received the purified and concentrated samples and undertook the desalting procedure and the actual mass spectrometric measurements.

7.3.1 Experimental

The sample for mass spectrometry was prepared by dissolving a small amount of lyophilized sulfonated ferredoxin in water. The samples were desalted on Micro Bio-Spin columns (Bio-Rad) into 100 mM NH_4CH_3COO and diluted to 20 µM protein concentration with 100 mM NH_4CH_3COO.

Data acquisition and analysis were performed using a mass spectrometer with a nano-electrospray ionization source in negative mode and a time-of-flight analyzer (LCT Premier, Waters).

7.3.2 Results and discussion

The calculated mass of the sulfonated *P. furiosus* ferredoxin with all 5 cysteines protected by sulfite groups is 7567.4 g/mol. It is not necessary to take charges into

account for this protein, since there is no metal centre and all charges arise from protonation and deprotonation as assumed by the deconvolution program.

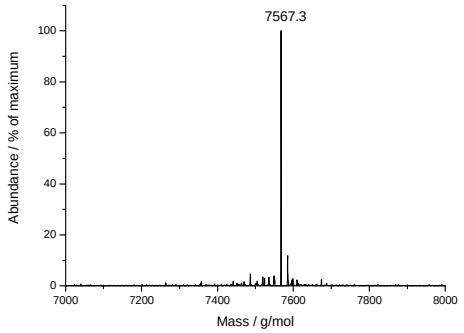

Figure 7.3: Mass spectrum of sulfonated *P. furiosus* ferredoxin. Protein concentration = 20 µM in 100 mM NH_4CH_3COO.

The mass spectrum of the sulfonated protein is shown in Figure 7.3. The spectrum almost exclusively has a single species with mass 7567.3 g/mol. This confirms the identity of the sample as the sulfonated *P. furiosus* ferredoxin. The absence of any significant other peaks suggests the sample is very pureand that the sulfonated protein is stable towards lyophilization.

7.4 Conclusions

Sulfonated *P. furiosus* ferredoxin was synthesized and purified according to in-house protocols and high yields were obtained. The mass spectrum confirms all five cysteines in the protein have been sulfonated and demonstrates the high purity of the lyophilized protein.

CHAPTER EIGHT

8 Studies of Molybdenum-Sulfur Clusters

8.1 Introduction

This chapter describes the synthesis and EPR spectroscopic characterization of the cuboidal molybdenum-sulfur cluster $[Mo_4S_4(H_2O)_{12}]^{5+}$. This cluster has attracted interest based on the catalytic properties and the structural similarities to iron-sulfur clusters as described in chapter 3. The main purpose for synthesis of $[Mo_4S_4(H_2O)_{12}]^{5+}$ in this project is the use for incorporation in *P. furiosus* ferredoxin (chapter 9). The EPR spectroscopic characterization of the cluster serves as a reference for the studies on the molybdenum-sulfur analogue of *P. furiosus* ferredoxin in chapter 9.8.

Several procedures have been developed for the synthesis of $[Mo_4S_4(H_2O)_{12}]^{5+}$, most of which involve a preliminary step with synthesis of other molybdenum-sulfur complexes. $[Mo_3S_4(H_2O)_{12}]^{4+}$ is the major side product in the syntheses and the double cube, $[Mo_7S_8(H_2O)_{18}]^{8+}$, a minor side product [5]. In this project $[Mo_4S_4(H_2O)_{12}]^{5+}$ was synthesized from $(NH_4)_2MoS_4$ or by reduction of $[Mo_3S_4(H_2O)_9]^{4+}$ according to the procedures of Shibahara et. al. [55, 80]. $[Mo_3S_4(H_2O)_{12}]^{4+}$ was synthesized either by other members of the Metalloprotein Chemistry group or as a side product. $(NH_4)_2MoS_4$ was synthesized by the method of McDonald et. al. [81].

EPR spectra of the $[Mo_4S_4]$ cluster core have been published previously. Sykes et. al. have published EPR spectra of the EDTA ligated cluster, $[Mo_4S_4(edta)_2]^{3-}$ [82] , and aqua complex, $[Mo_4S_4(H_2O)_{12}]^{5+}$ [83], both at very low temperatures. In this chapter, temperature effects on the spectrum of $[Mo_4S_4(H_2O)_{12}]^{5+}$ were studied. The cluster enriched in ^{95}Mo was also synthesized and studied in order to study possible hyperfine interaction effects.

8.2 Synthesis and purification of $[Mo_4S_4(H_2O)_{12}]Cl_5$

The complex enriched in ^{95}Mo was synthesized in one experiment. Published procedures were scaled down and are be described here. The procedures for purification of $[Mo_4S_4(H_2O)_{12}]^{5+}$ and drying as $[Mo_4S_4(H_2O)_{12}]Cl_5$ are also described. The same purification and drying procedures were used for larger scale syntheses.

8.2.1 Experimental

Synthesis of $(NH_4)_2{}^{95}MoS_4$: 1 g of ^{95}Mo-enriched MoO_3 was dissolved in 10 ml 25% NH_4OH and 3 ml water. This solution was bubbled with H_2S for 4 hours until the color of the solution remained unchanged dark red. H_2S was generated in a Kipp generator from FeS and HCl. The mixture was then heated to 60 °C for 30 minutes in a water bath, while maintaining a slow stream of H_2S. A solution of $FeCl_3$ was used as trap for excess H_2S. The dark red mixture was then cooled on ice for an hour to form crystals. The resulting red/brown crystals of $(NH_4)_2MoS_4$ were filtered and washed with $(CH_3)CHOH$ and $(CH_3CH_2)_2O$ (since the crystals dissolve in water and CH_3CH_2OH) and dried *in vacuo* before weighing.

Synthesis of $[Mo_4S_4(H_2O)_{12}]^{5+}$ from $(NH_4)_2MoS_4$: 1.8 g of the ^{95}Mo enriched $(NH_4)_2MoS_4$ was dissolved in 60 ml water. To this was added under vigorous stirring $NaBH_4$ (1.8 g dissolved in 24 ml ice-cold water) and 121 ml 6 M HCl by alternately adding 4 ml of each and adding the rest of the HCl solution at the end (BH_4^- and HCl have to be added slowly to avoid explosive H_2 formation). The resulting brown suspension was heated to 90 °C and bubbled with air for two hours. After cooling to room temperature the solution was filtered by gravity giving a dark green solution.

Purification and drying of $[Mo_4S_4(H_2O)_{12}]^{5+}$ (performed under Ar bubbling): The solution was bubbled with Ar and the purification was performed under Ar. The solution was diluted ~10 times with water and loaded onto a Dowex 50W-X2 column equilibrated and deoxygenated with 0.5 M HCl. The column was washed with copious amounts of 0.15 M H_2SO_4 followed by elution of the green $[Mo_3S_4(H_2O)_9]^{4+}$ with 0.25 H_2SO_4. $[Mo_4S_4(H_2O)_{12}]^{5+}$ was eluted with 0.6 M H_2SO_4. The collected $[Mo_4S_4(H_2O)_{12}]^{5+}$ was diluted 5 times with water and loaded onto another Dowex 50W-X2 column for re-purification. After loading, the column was washed with copious amounts of 0.25 M HCl followed by washing with 0.5 M HCl. $[Mo_4S_4(H_2O)_{12}]^{5+}$ was eluted with 1.5 M HCl. The product was then concentrated by diluting 4 times, loading onto a small Dowex 50W-2X column and eluting with a small volume of 5 M HCl. The concentration was determined by UV-vis spectrophotometry and the concentrated solution dried on a vacuum line.

8.2.2 Results and discussion

Synthesis of $(NH_4)_2MoS_4$: The procedure for $(NH_4)_2MoS_4$ synthesis was altered slightly from the published procedure [81]. The published procedure uses MoO_4^{2-} in the form of $Na_2MoO_4{\cdot}2H_2O$ as the starting material, but MoO_3 is used here since ^{95}Mo enriched MoO_3 is commercially available. Since MoO_4^{2-} is formed when MoO_3 is dissolved in alkaline solutions [48], this should not have any significance. The observations during the synthesis agreed with observations for experiments by other people in our lab following the originally published procedure. The color of solution turned from colorless over orange and red to very dark red during bubbling with H_2S and red crystals started to form after ~2 hours of bubbling. Figure 8.1 shows the UV-vis spectrum of a few of the crystals dissolved in water. The spectrum confirms the

identity of the product with peaks at 241, 316 and 416 nm. There were no signs of $MoOS_3^{2-}$ impurities in the spectrum [81]. The yield was 1.8 g $(NH_4)_2MoS_4$ corresponding to 99% (mol/mol) conversion from MoO_3. All the synthesized $(NH_4)_2MoS_4$ enriched in ^{95}Mo was used in the next step for synthesis of $[Mo_4S_4(H_2O)_{12}]^{5+}$.

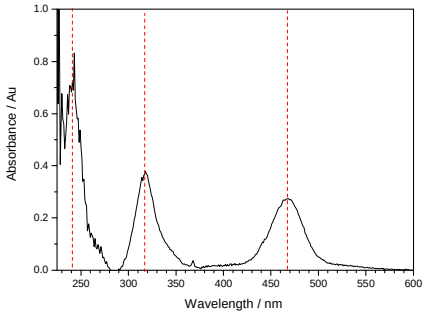

Figure 8.1: UV-vis spectrum of $(NH_4)_2MoS_4$ crystals dissolved in water. The dashed, red lines mark the adsorption at 241, 316, and 467 nm, respectively.

Synthesis and purification of $[Mo_4S_4(H_2O)_{12}]^{5+}$ from $(NH_4)_2MoS_4$: The crucial part of scaling down the procedure for synthesis was strong shortening of air-bubbling time. With bubbling for more than four hours, there was almost no yield of $[Mo_4S_4(H_2O)_{12}]^{5+}$, but almost exclusively formation of the incomplete cuboidal cluster, $[Mo_3S_4(H_2O)_9]^{4+}$. Bubbling for two hours with heating was found to be optimal. After the first crude purification the yields were 315 ml 1.16 mM $[Mo_3S_4(H_2O)_9]^{4+}$ in 0.25 M H_2SO_4 and 135 ml 428 µM $[Mo_4S_4(H_2O)_{12}]^{5+}$, respectively. The yield of the incomplete cluster is still much higher than the complete cuboidal cluster, in agreement with the previously published procedure [55]. ^{95}Mo-enriched $[Mo_3S_4(H_2O)_9]^{4+}$ was stored at 4 °C for other uses. There was no $[Mo_3S_4(H_2O)_9]^{4+}$ in the second purification step, indicating good separation in the first step and no breakdown of $[Mo_4S_4(H_2O)_{12}]^{5+}$. The complex was eluted in 5 ml 5 M HCl to a concentration of 4.97 mM (25 µmol in total) in the final concentration step.

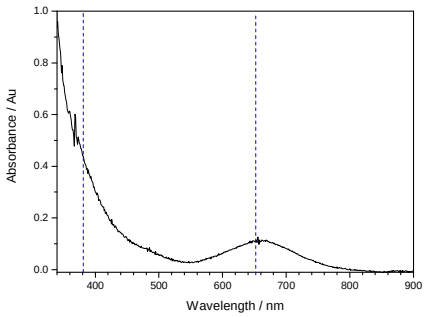

Figure 8.2: UV-vis spectrum of purified $[Mo_4S_4(H_2O)_{12}]^{5+}$ after final concentration in 5 M HCl after 20 times dilution. The dashed blue lines mark the shoulder at 380 nm and the peak at 647 nm, respectively.

A spectrum of the final sample after 20 times dilution is shown in Figure 8.2. $[Mo_4S_4(H_2O)_{12}]^{5+}$ has a characteristic shoulder at 380 nm and a peak at 647 nm [5]. The yield of $[Mo_4S_4(H_2O)_{12}]Cl_5$ was 35.1 mg after drying.

8.3 EPR spectroscopic Studies of $[Mo_4S_4(H_2O)_{12}]^{5+}$

The EPR spectroscopic characterization of $[Mo_4S_4(H_2O)_{12}]^{5+}$ serves as reference for the studies of the molybdenum-sulfur analogue of *P. furiosus* ferredoxin, chapter 9.8. These measurements were performed by Prof. W. R. Hagen at Delft University of Technology during my visits in his laboratories.

8.3.1 Experimental

Solutions of $[Mo_4S_4(H_2O)_{12}]^{5+}$, both natural Mo isotopic distribution and ^{95}Mo-enriched, in 4 M HCl were transferred to EPR tubes and frozen, stored and transported in liquid N_2.

EPR spectra were measured at different temperatures. Measurements at 100 K were carried out with N_2 cooling and measurements at 40 K and 12.5 K were carried out with He cooling. The instrumentation and software are described in chapter 4.3.3.

8.3.2 Results and discussion

The EPR spectrum of $[Mo_4S_4(H_2O)_{12}]^{5+}$ with the natural abundance of Mo isotopes at 12.5 K is shown in Figure 8.3. The spectrum could be fit by a simulation based on the *g*-values 1.778, 2.447 and 2.543. The lines are very broad, but can be simulated with *g*-strain effects $W_{xx} = 0.070$, $W_{yy} = 0.085$, $W_{zz} = 0.075$. Some broadening could be due to interactions between clusters since the concentration is very high compared to the previously published spectra. Sykes et. al. observed broadening of the lines in high concentrations [82]. The spectrum has an additional signal at $g \sim 1.9$ (3500 gauss), discussed further below, and a broad, not-simulated line at $g = 2.17$ (~3150 gauss). The other *g*-values accord with the reported values for $[Mo_4S_4(H_2O)_{12}]^{5+}$ [83]. The value of g_x is very different from the value of the EDTA-ligated cluster [82], 2.31.

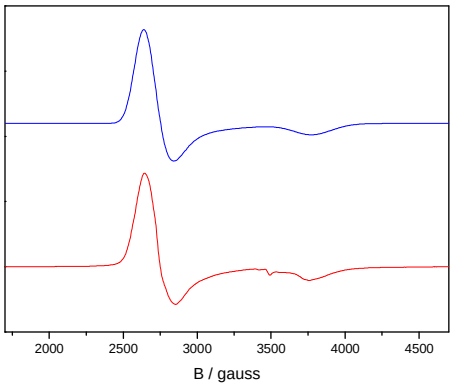

Figure 8.3: Red trace: EPR spectrum of 4.76 mM $[Mo_4S_4(H_2O)_{12}]^{5+}$, natural abundance, in 4 M HCl, T = 12.5 K, ν = 9.3993 GHz, P = 16 dB, M = 8, G = 10^3. Blue trace: simulated spectrum.

The field range of the published spectrum of $[Mo_4S_4(edta)_2]^{3-}$ [82] is not wide enough to include a line at $g = 1.77$. The reported g_x line is a weaker signal. We speculate that the reported spectrum of $[Mo_4S_4(edta)_2]^{3-}$ is measured in a too narrow field range and that a line would appear in the range of the here reported g_x line. We further speculate

that the reported g_x line at 2.31, which is weak, corresponds to the not-simulated line at g = 2.17 in the spectrum presented here. This suggestion could be either confirmed or excluded by measuring the spectrum of $[Mo_4S_4(edta)_2]^{3-}$ in a wider field range. Such studies were, however, beyond the limitations of this project. None of the previously reported spectra include simulations.

The previously published spectra do not show the signal near 3500 gauss. These other spectra were recorded at slightly lower temperature, *i.e.* 10 K [82] and 3.8 K [83] whereas the spectra presented here were recorded at 12.5 K, suggesting that this signal could be temperature-dependent. The spectrum was therefore recorded at different temperatures, Figure 8.4. The figure shows that the spectrum indeed changes with temperature. As the temperature is increased the signal near g = 1.9 also increases and the "normal" previously published signal decreases. This indicates that the signal at g = 1.9 arises from an excited state that is more occupied at higher temperatures. The experimental parameters are different in the three spectra and the intensities can therefore not be directly compared. Both signals are clear at 40 K.

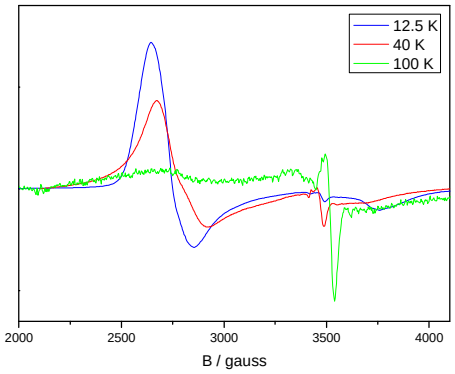

Figure 8.4: EPR spectra of 4.76 mM $[Mo_4S_4(H_2O)_{12}]^{5+}$, natural abundance, in 4 M HCl at different temperatures as indicated. 12.5 K) ν = 9.3993 GHz, P = 16 dB, M = 8, G = 10^3; 40 K) ν = 9.3986 GHz, P = 12 dB, M = 5, G = $6.3 \cdot 10^4$; 100 K) ν = 9.3964 GHz, P = 0 dB, M = 5, G = $1.25 \cdot 10^5$.

Figure 8.5 shows the EPR spectrum $[Mo_4S_4(H_2O)_{12}]^{5+}$ (red trace) in the field range near g = 1.9. The signal was fit by a simple simulation (blue trace) based on the g-values 1.96, 1.935 and 1.925, widths 7, 7, 10 and with hyperfine splittings of 40, 50, 25 from an I = 5/2 spin with an abundance of 25 % (*i.e.* the natural abundance of ^{95}Mo and ^{97}Mo). The simple simulation program could not take into account both the natural abundance of ^{95}Mo and ^{97}Mo, interacting Mo-atoms and g-strain effects, which is why the fit is not very good. It does, however, illustrate the hyperfine interaction effects in this signal. The g-values and hyperfine splittings are comparable values for octahedral $Mo(V)O_6$ sites in polymolybdates [84, 85] and bound to protein [86]. There should, however, not be any Mo(V) in this sample and the nature of this signal is therefore not fully understood.

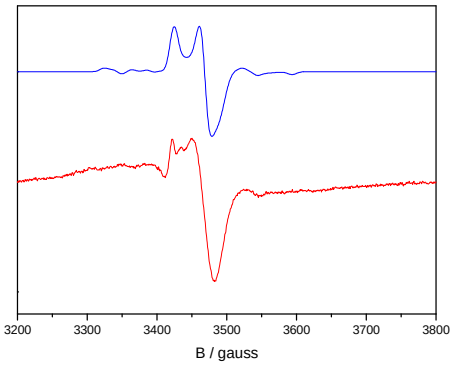

Figure 8.5: Red trace: EPR spectrum of 4.76 mM $[Mo_4S_4(H_2O)_{12}]^{5+}$, natural abundance, in 4 mM HCl near g = 1.9. T = 100 K, ν = 9.3965 GHz, P = 12 dB, M = 5, G = $3.2 \cdot 10^5$. Blue trace: simulated spectrum.

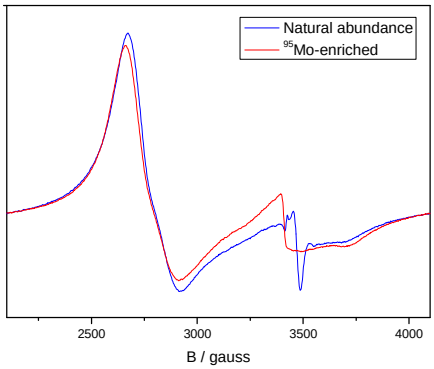

Figure 8.6: EPR spectra of $[Mo_4S_4(H_2O)_{12}]^{5+}$, natural abundance and enriched in ^{95}Mo as indicated in the legend, in 4 M HCl, T = 40 K. Natural abundance: 4.76 mM, ν = 9.3986 GHz, P = 12 dB, M = 5, G = $6.3 \cdot 10^4$. ^{95}Mo-enriched: 4.78 mM, ν = 9.3972 GHz, P = 12 dB, M = 5, G $6.3 \cdot 10^4$.

The spectrum of $[Mo_4S_4(H_2O)_{12}]^{5+}$ enriched in ^{95}Mo is shown in Figure 8.6 (red trace) compared to the spectrum of the cluster with natural abundance distribution of Mo isotopes. The main "normal" signal is similar in the two spectra, but there are changes in the "excited state" signal near 3500 gauss. The *g*-values of this part of the signal the have shifted to higher values (lower field values) and the spectrum is broader. The broadening can be reasoned by more abundant hyperfine splitting in the enriched cluster with higher abundance of Mo atoms with nuclear spin. Enrichment in ^{95}Mo does not, however, have a significant effect on the main signal. A spectrum of the enriched cluster in the narrower field range was not measured.

The spectrum of ^{95}Mo-enriched $[Mo_4S_4(H_2O)_{12}]^{5+}$ was also recorded at 12.5 K. As shown in Figure 8.7 it showed the same temperature dependence as $[Mo_4S_4(H_2O)_{12}]^{5+}$ with natural distribution of Mo isotopes.

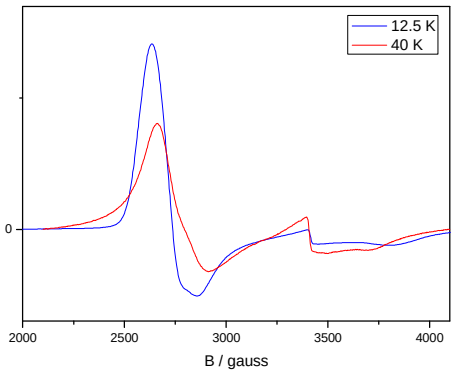

Figure 8.7: EPR spectra of 4.78 mM ^{95}Mo-enriched $[Mo_4S_4(H_2O)_{12}]^{5+}$ in 4 M HCl at different temperatures as indicated. 12.5 K) ν = 9.3971 GHz, P = 16 dB, M = 8, G = 10^3. 40 K) ν = 9.3972 GHz, P = 12 dB, M = 5, G = $6.3 \cdot 10^3$.

8.4 Conclusions

The syntheses of $[Mo_4S_4(H_2O)_{12}]^{5+}$ were carried out according to protocols based on published procedures. The small scale synthesis of the ^{95}Mo-enriched complex went through the synthesis of $(NH_4)_2MoS_4$, which was easily scaled down, However, it was necessary to reduce the incubation time significantly in the second step for reasonable yields. The spectra were in agreement with reported spectra.

The EPR signal of $[Mo_4S_4(H_2O)_{12}]^{5+}$ proved to be temperature dependent. At the lowest temperatures the dominant signal was in agreement with previously published low-temperature spectra. A signal arising from an unprecedented excited state was observed at higher temperatures. This signal had hyperfine interactions. The low-temperature signal did not change significantly for the ^{95}Mo-enriched $[Mo_4S_4(H_2O)_{12}]^{5+}$, but the excited-state signal broadened due to the more abundant hyperfine splitting in the enriched cluster.

CHAPTER NINE

9 Studies of the Molybdenum-Sulfur Analogue of *Pyrococcus furiosus* Ferredoxin

9.1 Introduction

This chapter describes the studies of the molybdenum-sulfur analogue of *P. furiosus* ferredoxin where the iron-sulfur cluster of the protein is replaced with a $[Mo_4S_4]$ cluster. In this project the protein was synthesized and the detailed characterization of the new protein was initialized. The basis for the replacement of the iron-sulfur cluster with a molybdenum-sulfur cluster is presented in chapter 3.

The first attempt to introduce a $[Mo_4S_4]$ cluster into an iron-sulfur protein was performed by T. C. Sow [87]. This work proved the successful incorporation of a $[Mo_4S_4]$ entity in recombinant *D. gigas* apo-ferredoxin resulting in four discrete species. The designed molybdenum-sulfur protein was proposed to cycle between three different oxidation states and bind exogenous ligands such as DTT.

Members of the Metalloprotein Chemistry Group have continued the work on molybdenum-sulfur analogues of iron-sulfur proteins. This has included further studies of the incorporation of $[Mo_4S_4]$ in *D. gigas* ferredoxin as well as in other iron-sulfur proteins [71, 88, 89, 90, 91]. The work so far has focused on the synthesis of molybdenum-sulfur analogues of the simple electron transferring iron-sulfur proteins, ferredoxins and HiPIPs, and development of procedures for purification. The next goal is detailed characterization of the new proteins.

The starting point of this project is based on the procedure for synthesis, purification and preliminary characterization of the molybdenum-sulfur analogue of *P. furiosus* ferredoxin has been developed through multiple stages by several people of the Metalloprotein Chemistry Group. This will be described in the following section.

9.2 Preliminary studies of the molybdenum-sulfur analogue of *P. furiosus* ferredoxin

Unlike iron-sulfur clusters, the molybdenum-sulfur cluster cannot be incorporated in the ferredoxin by self-assembly. The molybdenum-sulfur analogue is instead formed

by adding previously prepared $[Mo_4S_4]$ cluster complex (see chapter 8) to the apo-protein. As described in chapter 7 the apo-protein is protected by sulfite-groups in the stable storable form. The strategy for the synthesis is shown in Figure 9.1. The protocol for the bottom half of the figure with the synthesis and purification of the molybdenum-sulfur analogue is carried out anaerobically and has been developed and optimized by several people before this work, most significantly by Rinette Drewsen in her M.Sc. project [90] and Hajnalka Baratne-Jankovics during her postdoctoral stay in the Metalloprotein Chemistry Group [91]. This protocol was the starting point for the present work and the results of this procedure will briefly be described here.

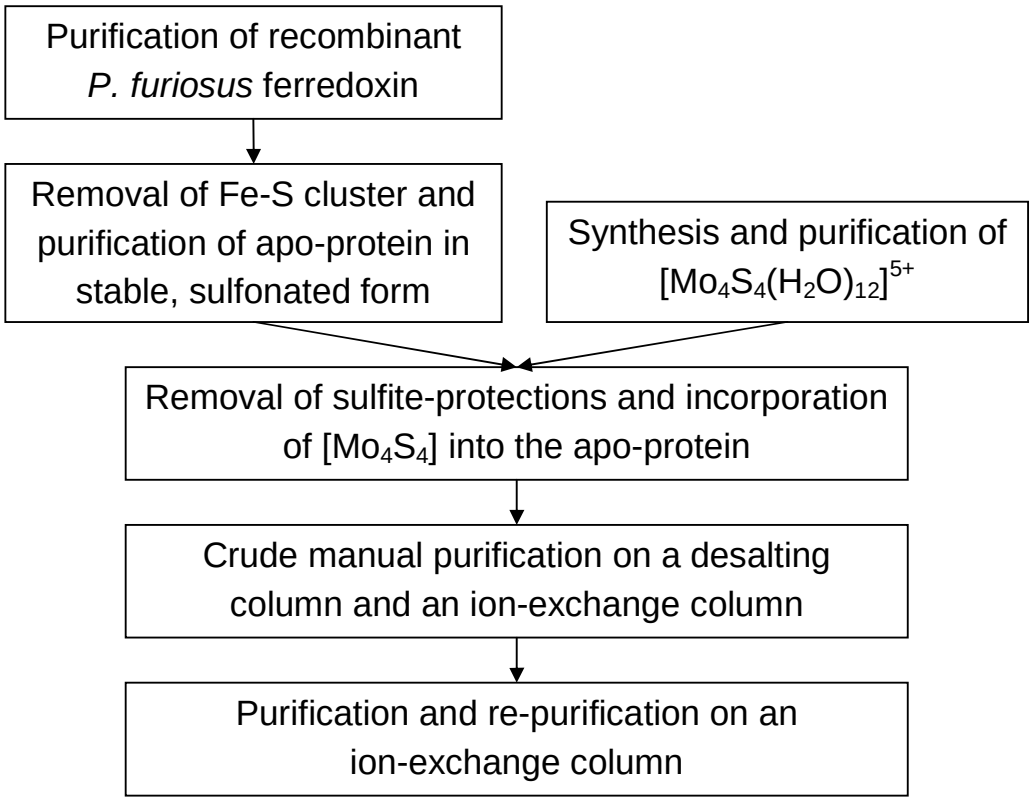

Figure 9.1: Strategy for synthesis and purification of the molybdenum-sulfur analogue of *P. furiosus* ferredoxin.

The bottom half of Figure 9.1 has to be carried out anaerobically since the molybdenum-sulfur analogue is sensitive towards oxygen. All the work carried out before the present project was carried out under flushing with Ar. The protocol was developed for 60 mg sulfonated *P. furiosus* ferredoxin. The sulfite-protection groups were removed with 20 times molar excess DTT and the molybdenum-sulfur cluster was incorporated by addition of 4 times molar excess $[Mo_4S_4(H_2O)_{12}]Cl_5$. The mixture was purified by desalting and crude ion-exchange before HPLC purification. The same protocol was used in this project, except the work was carried out in a glove box. The detailed procedures are described in section 9.3.1. The HPLC purification consists of two steps: an initial ion-exchange on a ResourceQ column, called Resource 1, and a re-purification step on the same column and by the same procedure, called Resource 2.

Representative results of the HPLC purification outside the glove box are shown in Figure 9.2. The chromatogram of Resource 1 has one main peak with shoulders on both sides and a series of subsequent peaks in the 280 nm curve. The 380 nm curve only has significant absorption in the main peak fractions. These fractions were collected and re-purified. The chromatogram of resource 2 is dominated by a peak absorbing at both 280 and 380 nm at ~23.5 mS/cm overlapping with a shoulder at ~22.5 also absorbing at both wavelengths. Both the peak and the shoulder were collected and it was not attempted to separate the two. There are some other smaller shoulders surrounding the peak in the chromatogram, none of which absorb at 380 nm. These were not collected and further analyzed.

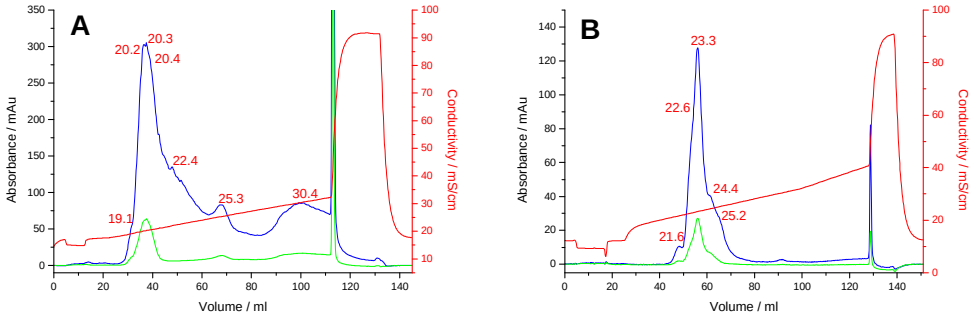

Figure 9.2: Chromatograms of the purification of the molybdenum-sulfur analogue of *P. furiosus* ferredoxin on a ResourceQ column. A) Resource 1, B) Resource 2. The green and blue lines indicate the absorption at 280 and 380 nm, respectively, and the red line the conductivity gradient. The red numbers indicate the conductivities at the absorption maxima.

Preliminary mass spectrometric characterization has confirmed that collected fractions do indeed consist of *P. furiosus* ferredoxin with the $[Mo_4S_4]$ bound. The results indicate that additional water and buffer molecules are bound to the protein, suggesting that these occupy the extra ligand sites in the molybdenum-sulfur analogue [89, 90]. These results were, however, not conclusive. The later eluting peaks in the first purification (at ~30mS/cm) were proved to consist of apo-ferredoxin. The purified protein is very unstable even when kept under Ar and in tubes sealed with rubber septa.

9.3 Introducing synthesis and purification of the molybdenum-sulfur analogue of *P. furiosus* ferredoxin to anaerobic chambers

In this project the work on the molybdenum-sulfur analogue is carried out in the glove box to increase the stability of the protein. The purpose of the first experiments was to see if and how the glove box conditions changed the outcome of the synthesis and purification and whether the protocol had to be adjusted. These experiments were carried out according to the previously developed protocol. The program for HPLC purification was slightly changed: the gradient was shortened and the slope was flattened. This was done to provide better separation of the species of interest without prolonging the time for each run.

9.3.1 Experimental

Synthesis: 60 mg lyophilized sulfonated protein was dissolved in 10 ml 100 mM Tris/HCl, pH 8.5 with gentle stirring. 24.7 mg DTT (20 times molar excess) dissolved in 200 µl 100 mM Tris/HCl, pH 8.5 was added to the protein and the solution was incubated for 90 minutes. A solution with 29 mg $[Mo_4S_4(H_2O)_{12}]Cl_5$ (4 times molar excess) dissolved in 20 µl 1 M HCl and diluted with 380 µl water was prepared and added dropwise to the protein solution and incubated for 60 minutes.
Crude purification: The brown solution (10.6 ml) was filtered through a 0.45 µm filter and loaded onto two 19 ml Sephadex G25 columns equilibrated with 100 mM Tris/HCl, 0.05 M NaCl, pH 8.5. The protein was eluted with the same buffer and loaded directly onto a 5.5 ml DE52 column equilibrated with 100 mM Tris/HCl, 0.05 M NaCl, pH 8.5. The column was first washed with 2 CV of the same buffer, followed by elution of the dark protein solution with 20 mM Tris/HCl, 0.3 M NaCl, pH 8.5.
Purification and re-purification on HPLC: The sample was diluted 2 times with 20 mM Tris/HCl, pH 8.0 split in 2 portions (*i.e.* two Resource 1 runs) and loaded onto a 6 ml ResourceQ column equilibrated with 20 mM Tris/HCl, 0.1 M NaCl, pH 8.0 on HPLC (ÄKTAprime™ plus). The protein was purified using a linear gradient of NaCl from 0.15 M to 0.30 M in 16 CV, 6 ml/min. The collected fractions from each run were diluted 2 times with 20 mM Tris/HCl, pH 8.0, split in 2 again (*i.e.* four Resource 2 runs in total) and re-purified on the same column with the same gradient.
In some experiments the solution was left overnight in the glove box between the crude purification and the HPLC purification; in other experiments everything was done in one (long) day.

9.3.2 Results and discussion

Figure 9.3 and Figure 9.4 shows the chromatograms of Resource 1's and Resource 2's after one of the initial syntheses in the glove box. The purification was carried out on the same day as the synthesis in this example. The two Resource 1 chromatograms, Figure 9.3, both show the same features as the Resource 1 chromatogram in Figure 9.2A with one major peak followed by several peaks and shoulders. However, the two chromatograms in Figure 9.3 are not identical even though they stem from one solution that has just been split in two purifications. The conductivity of the eluting species changes with ~1 mS/cm between the two purifications. The main peak is collected from these purifications.
In the Resource 2 chromatograms in Figure 9.4 the collected fractions from Resource 1 splits up in two overlapping peaks. One peak with overlapping shoulders was observed in the studies outside the glove box. The observation of separable peaks could arise from the flatter gradient in the experiments inside the glove box increasing the resolution of the purification. The conductivity at the eluting peaks varies between the four runs as was observed for the Resource 1 purifications. The conductivity at the elution is also increased from the Resource 1 runs and the Resource 2 runs. A signifi-

cant variation between the ratios of the two peaks is seen when between different synthesis experiments and also within some of the other experiments (not shown here).

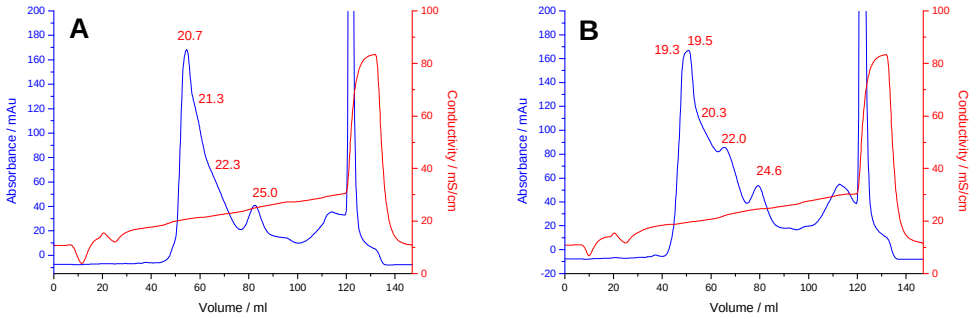

Figure 9.3: Chromatograms of Resource 1 purifications of the molybdenum-sulfur analogue of *P. furiosus* ferredoxin on a ResourceQ column in the initial studies in the glove box. A) 1st run, B) 2nd run. The blue line indicates the absorption at 280, and the red line the conductivity gradient. The red numbers indicate the conductivities at the absorption maxima.

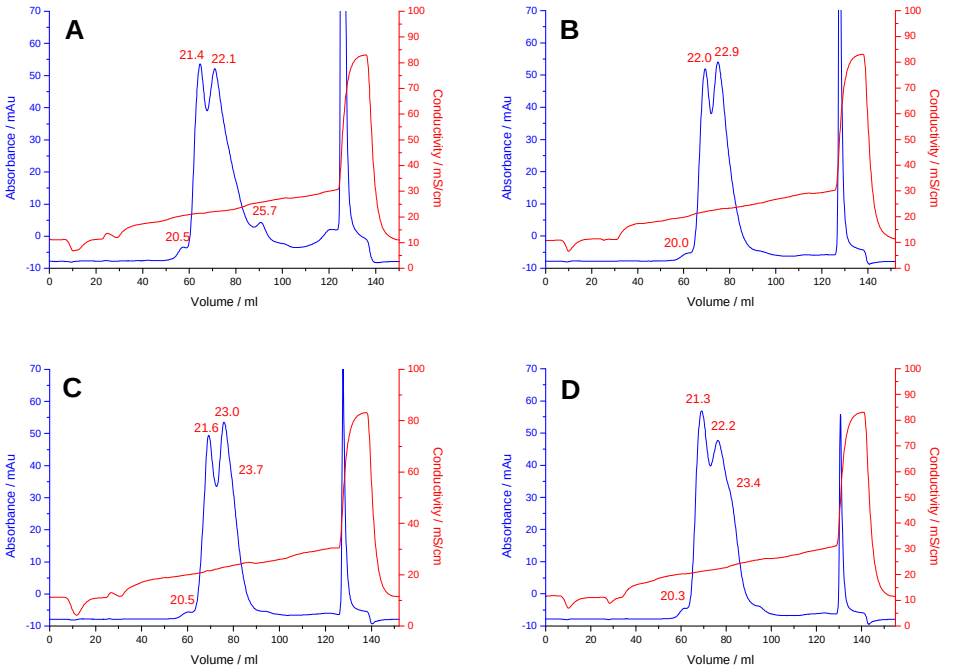

Figure 9.4: Chromatograms of Resource 2 purifications of the molybdenum-sulfur analogue of *P. furiosus* ferredoxin on a ResourceQ column. A and B) Re-purifications from Figure 9.3A, C and D) re-purifications from Figure 9.3B. The blue line indicates the absorption at 280, and the red line the conductivity gradient. The red numbers indicate the conductivities at the absorption maxima.

These observations suggest changes in the sample between the two purifications and that something happens during the time that elapses between Resource 1 and Resource 2 that induces some "delay time"-dependent variations in Resource 2 chromatograms. That could suggest that the two peaks arise from two closely related species with time-dependent interconversion between the two forms. This was further studied by investigating the stability of the purified samples and the effect of "delay time" on

the purifications as described in the next section.

In the following sections fractions from the first eluting peak in the Resource 2 chromatogram is referred to as peak 1 and peak 2 refers to the second eluting peak.

9.4 Studies of stability and interconversion of purified species of the molybdenum-sulfur analogue of *P. furiosus* ferredoxin

Experiments were set up where the time between the first HPLC purification and the second purification was varied systematically. This was done to study the effect of this "delay time" on the ratio of the two species in the chromatogram. The purified species were also re-purified to investigate the degree of re-arrangement or break down of the purified species.

9.4.1 Experimental

The synthesis and crude purification was carried out as described in section 9.3.1 and the same program for HPLC purification was used. The time between the purifications was the only factor changed.

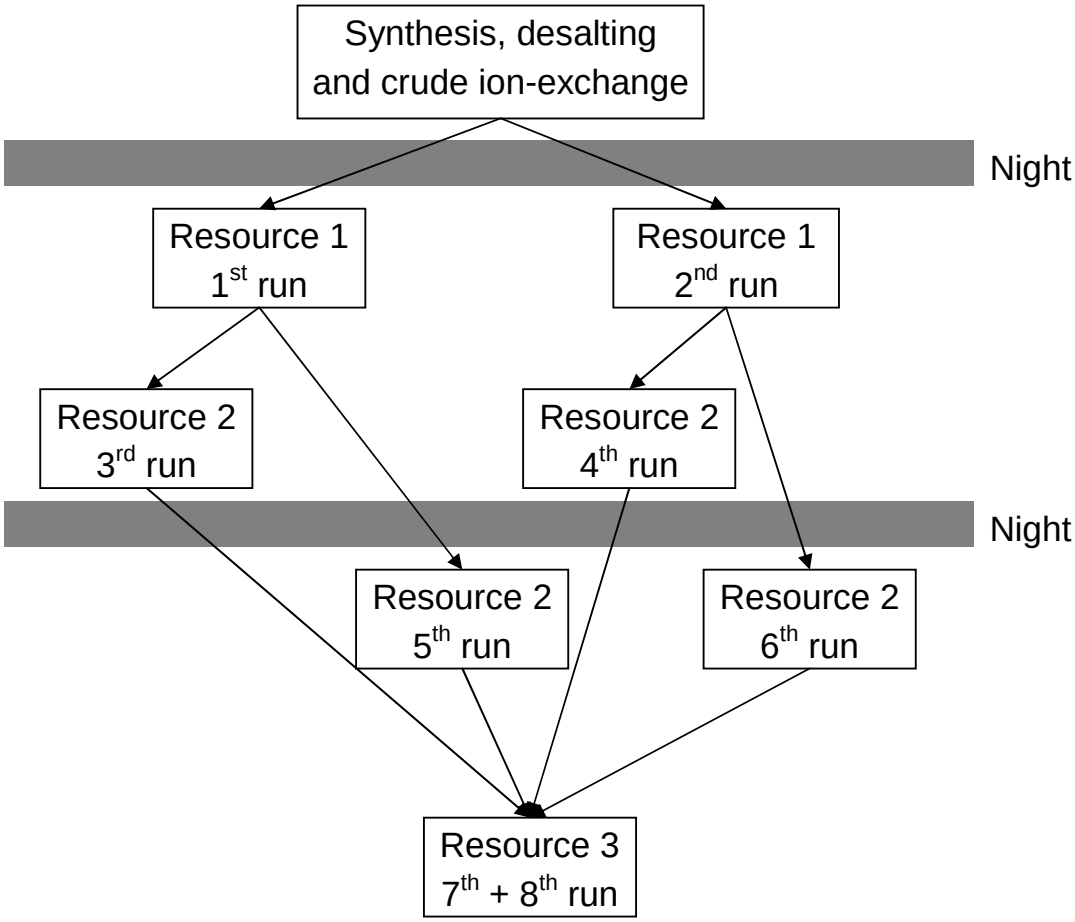

Figure 9.5: Flowchart of the purification and re-purification of the molybdenum-sulfur analogue of *P. furiosus* ferredoxin in Experiment 1.

Experiment 1: The purifications in this experiment were setup as shown in the flow-chart in Figure 9.5. The Resource 2 purifications were carried out either immediately

after the Resource 1 purifications or after waiting overnight. Resource 3 represents a third HPLC purification step in which the purified fractions from Resource 2 are re-purified. In this experiment, a small volume of peak 1 fractions from each run was mixed and re-purified in the 7th run and a small volume of peak 2 fractions was re-purified in the 8th run. The grey bars mark when the samples were stored overnight in the glove box. This experiment was carried out twice. It was also attempted to delay one of the Resource 1 runs one more day (i.e. keeping half of the collected volume after the crude ion-exchange in the glove box for 2 nights before the 2nd Resource 1 run).

Experiment 2: This experiment was run similar to Experiment 1, but instead of mixing a small volume of each peak from all runs in the Resource 3 re-purifications, Resource 3 was the re-purification of the full samples from one purification run. The purified samples of peak 1 and peak 2 were kept overnight in the glove box between the Resource 2 and Resource 3 purifications.

Experiment 1 was carried out in the Labstar 50 glove box while experiment 2 was carried out in the anaerobic system from Coy Laboratories (see chapter 4.3.1 for description of the anaerobic chambers).

9.4.2 Results and discussion

Experiment 1: The chromatograms of Resource 1 purifications are very similar to the chromatograms in Figure 9.5 in all purifications and they are not shown here. The chromatograms of Resource 1 runs did not change after storage in the glove box for another 24 hours and do therefore not depend on the storage time.

The chromatograms of the Resource 2 runs are shown in Figure 9.6. The chromatograms in A and B were recorded a few hours after the Resource 1 runs, while the chromatograms in C and D were carried out the following day. The tendency observed in this and the other experiments like this was that the ratio of peak 1 compared to peak 2 increases with longer incubation time. From the chromatograms shown it is most evident by comparing B and D that are re-purifications from the same Resource 1 run. This suggests more predominant conversion to peak 1 than peak 2 with longer delay time.

These observations indicate that the crudely purified sample is stable, but that changes occur after the first HPLC purification step. After the first HPLC purification, the collected species stabilize to the two forms eluting as peak 1 and peak 2 and more of the protein stabilizes as the peak 1 species with time.

The conductivities of the peaks vary slightly between the four chromatograms. A small volume of peak 1 samples from all four purifications was therefore mixed and a small volume of the peak 2 samples was mixed. The two mixed samples were re-purified to check 1) whether peak 1 and peak 2, respectively, arise from the same species in all runs, 2) whether there is further interconversion between the 2 species, and 3) whether they re-arrange inter yet other forms. The chromatograms of the re-purifications are shown in Figure 9.7. Both re-purifications show one sharp peak veri-

fying that the mixed fractions do indeed consist of the same species. The chromatogram of re-purification of peak 1, Figure 9.7A, has some subsequent shoulders that could arise from peak 2 species probably stemming from the overlap of the two peaks in the Resource 2 purification. There are no indications of further interconversion or re-arrangement of the species purified in Resource 2 based on these purifications. The conductivity of the eluting peaks has increased compared to the Resource 2 runs.

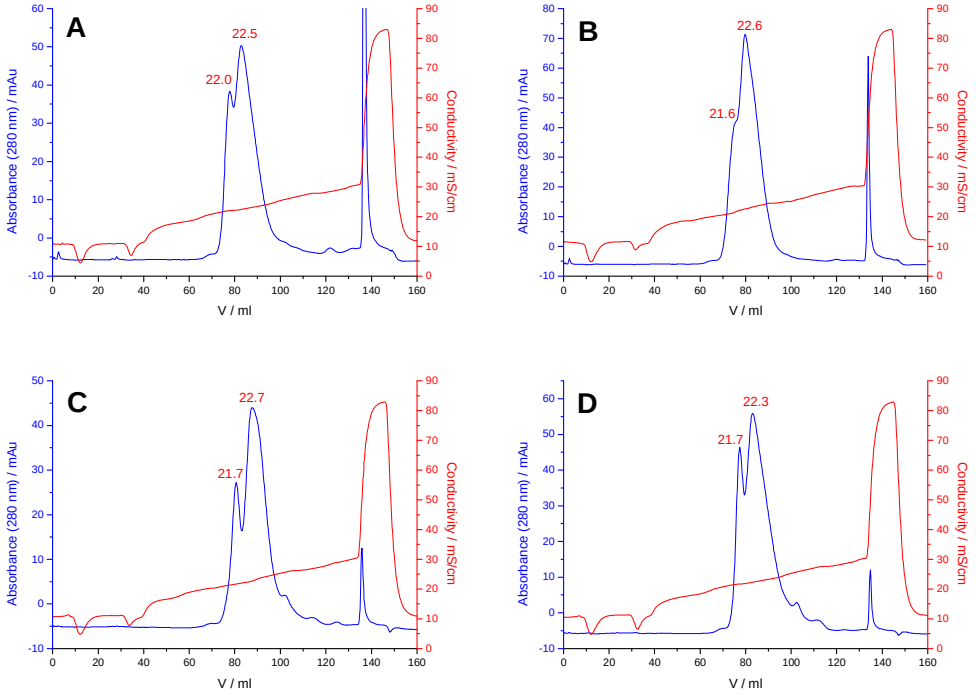

Figure 9.6: Chromatograms of Resource 2 purifications of the molybdenum-sulfur analogue of *P. furiosus* ferredoxin on a ResourceQ column in Experiment 1. A) 3rd run, from 1st run, 2.5 hours delay, B) 4th run, from 2nd run, 2.5 hours delay, C) 5th run, from 1st run, 24 hours delay, and D) 6th run, from 2nd run, 24 hours delay. The run numbers refer to the flowchart in Figure 9.5. The blue line indicates the absorption at 280, and the red line the conductivity gradient. The red numbers indicate the conductivities at the absorption maxima.

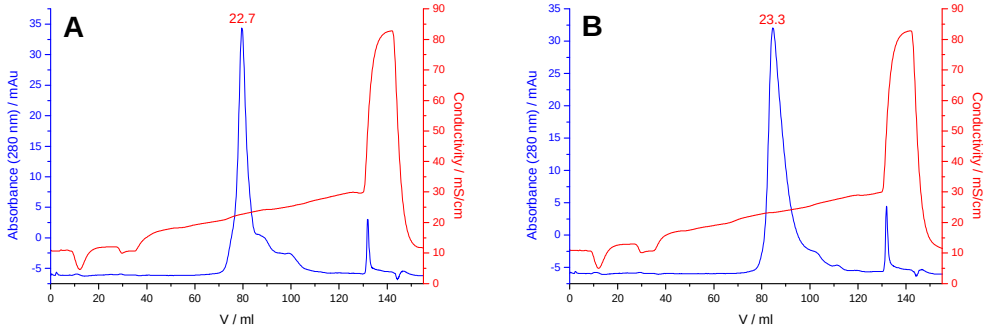

Figure 9.7: Chromatograms of Resource 3 purifications of the molybdenum-sulfur analogue of *P. furiosus* ferredoxin on a ResourceQ column in Experiment 1, re-purification of chromatograms in Figure 9.6. A) Re-purification of peak 1 samples, 7th run. B) Re-purification of peak 2 fractions, 8th run. The blue line indicates the absorption at 280 and the red line the conductivity gradient. The red numbers indicate the conductivities at the absorption maxima.

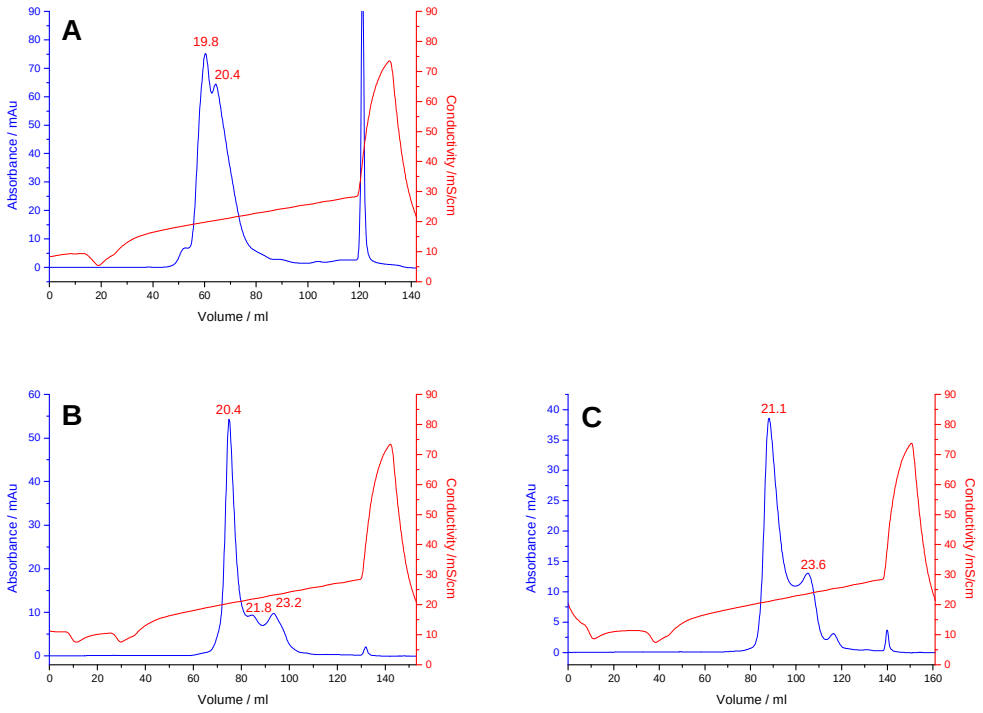

Figure 9.8: Chromatograms of one Resource 2 purification and Resource 3 purifications of the molybdenum-sulfur analogue of *P. furiosus* ferredoxin on a ResourceQ column in Experiment 2. A) Resourse 2 run corresponding to 4th run, B) Resource 3, re-purification of peak 1 collected from A, and C) Resource 3, re-purification of peak 2 collected from A. The blue line indicates the absorption at 280 and the red line the conductivity gradient. The red numbers indicate the conductivities at the absorption maxima.

Experiment 2: The chromatograms of one Resource 2 run and the re-purifications of the peaks collected in this purification are shown in Figure 9.8. In this experiment there are some subsequent smaller peaks and shoulders after the main peaks, especially in the re-purification of peak 2 in Figure 9.8C where a significant peak arises. That indicates some instability of the peak 2 species. This was not observed in Experiment 1 and the differences could be an effect of the different anaerobic systems. It is plausible that the stability of the purified samples is very sensitive towards factors like temperature and trace amounts of oxygen that vary in the different experiments and depend on the anaerobic system used. The subsequent peaks in the re-purification of peak 1 in Figure 9.8B are likely to arise from overlap of the peaks, but could also be due to re-arrangements influenced by the same factors as peak 2.

There is a variation in the conductivity of the eluting peaks between different experiments. However, in all experiments the same tendency towards increased conductivity in each purification step, both from Resource 1 to Resource 2 and from Resource 2 to Resource 3, is observed. The change in conductivity is usually in the range of 1-2 mS/cm in each step. Conductivity variations could be due to small variations in pH in different buffer preparations, since variations in pH would change the charge of the protein. However, the same buffer preparation is normally used within one experiment so pH variations can only explain variations between different experiments and not

the systematic increase between each step within one experiment. An explanation for this effect could be that less and less of the material that binds strongly to the column in the sample the further one gets in the purification, since it is separated from the protein sample. Strongly binding material could push the lighter binding protein out of the column earlier by making the column effectively shorter since less column material is available to bind the protein.

The ratio between the two peaks vary between ~30% and ~70% of either species from experiment to experiment, but the ratio of the peak 1 species to peak 2 species always increases with longer delay time. The ratio in each experiment can be explained by small variations in temperature, trace amounts of oxygen and variations in pH in different buffer preparations.

Overall these results indicate that the protein exists in two closely related forms represented by peak 1 and peak 2 that can be separated in the second purification step. The ratio between the two forms depends on the experimental conditions, but more of the protein always stabilizes as the peak 1 species with longer delay time. Along with the results of experiment 2, this suggests that the peak 1 species is the more stable of the two forms.

Several possible differences between the two forms can be suggested:

A) Different redox states – As seen for the [$CoFe_3S_4$] ferredoxin, the reduced and oxidized forms elute as two different peaks that can be separated. However, in other experiments with reduced and oxidized *P. furiosus* ferredoxin, *e.g.* the [$CoFe_3S_4$] ferredoxin in chapter 6.3, the conductivity difference between the two peaks was slightly larger than what is observed here.

B) Protonation/deprotonation of ligands/amino acids – Different protonation state of acidic/basic ligands or amino acids would change the net charge of the protein. However, since the experiments are carried out at constant pH, the protonation equilibrium should not change. If this was the difference between the two states, the equilibrium should therefore be re-established after separation leading to a splitting to two peaks in the re-purification. That was not observed and this scenario is therefore not considered likely.

C) Different exogenous ligands on the cluster – The preliminary mass spectrometric characterization has not been conclusive. It points to water as the predominant ligand, but also suggests binding of buffer molecules, possibly as ligands to the cluster. One could also imagine Cl^- ions as ligands to the molybdenum-sulfur cluster. The two species could arise from different ligand environments that re-arranges during the purification with one of the states, the one corresponding to peak 1, being more stable, but the stability depending on the experimental conditions.

D) Buffer molecules binding to the protein – As written above, the mass spectrometric analysis suggested binding of buffer molecules to the protein, but it is not clear whether these were bound as ligands to the cluster or bound to the peptide chain.

Different ligands and molecules bound to the protein would lead to different masses and they could also be charged. Thereby they can change the net charge of the protein and lead to elution at different conductivities. Such differences could therefore cause the observed differences between peak 1 and peak 2 in the chromatograms. The differences between the two forms were addressed as part of the further characterization.

Typical yields were ~400 µM, 0.5 ml (0.2 µmol) of peak 1 and ~200 µM, 0.5 ml (0.1 µmol) of peak 2 from one synthesis. Typically, a given characterization experiment was carried out on freshly prepared products of a given synthesis. That is, 60 mg (8 µmol) of sulfonated protein was used every time giving molar yields of 2.5% of peak 1 and 1.25% of peak 2. The work on the molybdenum-sulfur analogue is therefore very expensive in protein.

The chromatograms looked similar when the synthesis and purification was carried out with the ^{95}Mo-enriched $[Mo_4S_4(H_2O)_{12}]^{5+}$. These samples were used as part of the EPR spectroscopic characterization (see section 9.8).

9.5 UV-vis spectroscopy of the molybdenum-sulfur analogues of *P. furiosus* ferredoxin

The molar absorption coefficients were determined by determination of molybdenum content by inductively coupled plasma mass spectrometry (ICP-MS). ICP-MS was recorded by Ph.D. student Anders C. Raffalt.

9.5.1 Experimental

Purified peak 1 and peak 2 samples were concentrated in a Vivacell 70 with a MWCO 5000 membrane inside the anaerobic chamber. The UV-vis spectra of the concentrated samples in 20 mM Tris/HCl, pH 8.0 were recorded.

The concentrated samples were hydrolyzed in 1 M HNO_3 and diluted with water and 0.1 M HNO_3 (0.1 M HNO_3 in the final samples) to appropriate concentrations. These were roughly estimated based on the molar absorption coefficients determined by T. C Sow for the molybdenum-sulfur analogue of *D. gigas* ferredoxin [87].

ICP-MS was measured on the diluted samples on an ELAN 6000 (Perkin Elmer) mass spectrometer in the Analytical Chemistry Group at Department of Chemistry, DTU.

9.5.2 Results and discussion

The products obtained after the second HPLC purification are only slightly colored. The color cannot be seen in collected fractions after the purification, but is only visible after up-concentration. Both peak 1 and peak 2 samples have a weak grey-purple color.

The UV-vis spectra of concentrated peak 1 and peak 2 samples are shown in Figure 9.9. Both species have a characteristic shoulder at 360 nm and the spectrum of peak 1 also reveal a feature in the 500-600 nm range. The absorption of peak 2 was too low to detect such a feature with reasonable accuracy. Peak 2 has a much larger A(280

nm):A(360 nm) ratio than peak 1 (5 for peak 1, 22 for peak 2). This is much lower than the ratios observed for the native *P. furiosus* ferredoxins in Figure 5.2, chapter 5.2 (A(280):A(408) = 1.65 for $[Fe_3S_4]$ ferredoxin, A(280):A(380) = 1.78 for the $[Fe_4S_4]$ ferredoxin). These numbers support the much weaker color of the molybdenum-sulfur analogue compared to the native ferredoxins, which have a strong brown color.

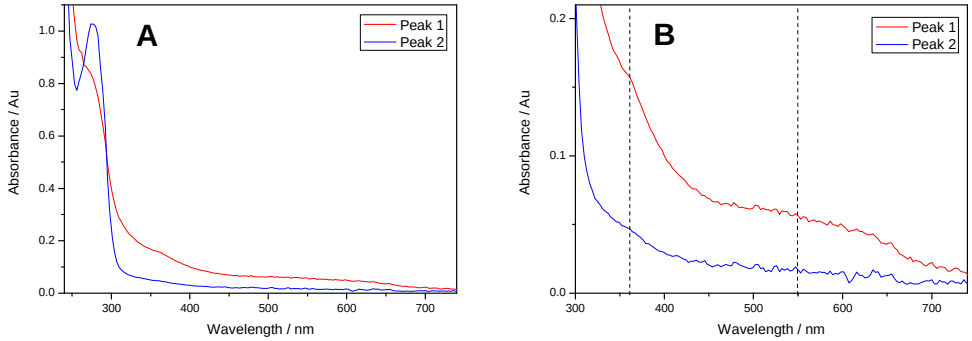

Figure 9.9: UV-vis spectra of the two species of the molybdenum-sulfur analogue of *P. furiosus* ferredoxin as indicated. A) In the full wavelength range and B) Above 300 nm. The dashed line mark the absorption at 360 and 550 nm, respectively.

Table 9.1: Molar absorption coefficients of the two molybdenum-sulfur analogue species of *P. furiosus* ferredoxin per $[Mo_4S_4]$ cluster.

	Molar absorption coefficients per $[Mo_4S_4]$ cluster / $M \cdot cm^{-1}$		
	280 nm	360 nm	550 nm
Peak 1	$35 \cdot 10^3$	$7.04 \cdot 10^3$	$2.52 \cdot 10^3$
Peak 2	$250 \cdot 10^3$	$11.5 \cdot 10^3$	-

Table 9.2: Molar absorption coefficients of the molybdenum-sulfur analogue species of *D. gigas* ferredoxin per $[Mo_4S_4]$ cluster [87].

	Molar absorption coefficients per $[Mo_4S_4]$ cluster / $M^{-1} \cdot cm^{-1}$	
	350 nm	600 nm
Species A	6860	1260
Species B	8740	1605
Species C	7105	1050
Species D	10165	2685

The molar absorption coefficients of the two species of molybdenum-sulfur analogues were determined from the molybdenum concentrations by assuming four molybdenum atoms (*i.e.* one $[Mo_4S_4]$ cluster) per protein. The absorption coefficients determined are given in Table 9.1. The absorption coefficients are in the same range as the absorption coefficients for the molybdenum-sulfur analogue of *D. gigas* ferredoxin (listed in Table 9.2, [87]). The determination of absorption coefficients was carried

out twice with agreeing results. Typically, concentration determinations were based on the absorption at 360 nm, since the signal to noise ratio at 550 was too low.

9.6 Attempts to characterize the molybdenum-sulfur analogues of *P. furiosus* ferredoxin with mass spectrometry

Since the preliminary mass spectrometric studies of the molybdenum-sulfur analogue were not conclusive and possibly carried out on a mixture of species, it was attempted to characterize the two species purified in this project with mass spectrometry. This would potentially confirm the incorporation of the $[Mo_4S_4]$ cluster and give insights as to the ligand environment of the cluster.

The mass spectrometric measurements were carried out in corporation with Ph.D. student Maja Martic who did the desalting and the mass spectrometric measurements.

9.6.1 Experimental

Purified samples of peak 1 and peak 2 were concentrated separately in a Vivacell 70 with a 5000 MWCO membrane. The concentration was determined by UV-vis spectrophotometry using the absorption coefficients determined above.

The samples were desalted on Micro Bio-Spin columns (Bio-Rad) into either water, 100 mM NH_4CH_3COO or 100 mM NH_4CH_3COO/NH_4OH, pH 8.0 and diluted with the same solution to 20µM protein concentration.

Data acquisition and analysis were performed using a mass spectrometer with a nano-electrospray ionization source in negative ion mode and a time-of-flight analyzer (LCT Premier, Waters).

9.6.2 Results and discussion

The molar mass of the *P. furiosus* ferredoxin with an incorporated $[Mo_4S_4]$ cluster is 7679 g/mol. This mass should be adjusted for the extra ligands binding to the cluster (eight additional ligand sites compared to the $[Fe_4S_4]$ cluster) and for the charge on the cluster.

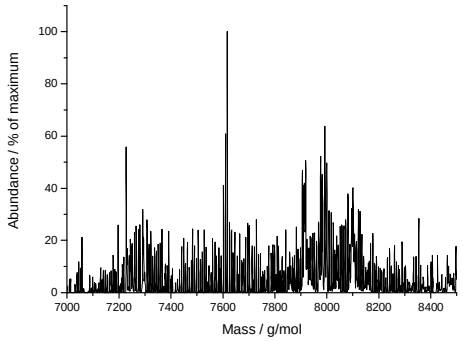

Figure 9.10: Mass spectrum of peak 1. Protein concentration = 20 µM in 100 mM NH_4CH_3OO/ NH_4OH, pH 8.0.

Figure 9.10 shows the best achieved mass spectrum of a peak 1 sample. The noise

level in the spectrum is very high indicating no dominant species and it is not possible to conclude anything about the protein composition from the spectrum. The noise level in measured mass spectra of peak 2 was worse than the showed spectra of peak 1.
The high degrees of noise indicate that the protein breaks down in the process, either during desalting, the handling before assembling the capillary in the mass spectrometer where the protein is exposed to oxygen, or in the electrospray. It was attempted to stabilize the protein in different solutions, but that did not optimize the spectra. Further optimization of the mass spectra was beyond the time limitations of this project.

9.7 Attempts at electrochemical characterization of the molybdenum-sulfur analogues of *P. furiosus* ferredoxin

It was attempted to characterize the molybdenum-sulfur analogue of *P. furiosus* ferredoxin to investigate possible redox-chemistry of the new protein.

9.7.1 Experimental

Several attempts were made to characterize the molybdenum-sulfur analogue in different buffers. The purified protein was concentrated in a Vivacell 70 with a 5000 MWCO. In some experiments the concentrated protein solution was diluted with 20 mM Tris/HCl, pH 8.0 without removal of trace amounts of NaCl. This was done to prevent loss of protein during the buffer change. It was also attempted to dilute the solution with 20 mM Tris/HCl, pH 8.0, 0.1-0.5 M NaCl for electrochemistry. The solution was concentrated and diluted 50 times with 20 mM Tris/HCl, pH 8.0 3 times to remove trace amounts of NaCl in another experiment. The protein concentration was determined with UV-vis spectrophotometry.
The electrodes were polished and transferred into the glove box and mounted in the electrochemical cell as described in chapter 4.3.2. Neomycin sulfate powder and L-cysteine powder were added to the solution during experiments without further purification by dissolution in a small volume of the protein solution and transferring this to the cell. Both promoters were used at 5 mM concentrations.

9.7.2 Results and discussion

The attempts to characterize the molybdenum-sulfur analogue of *P. furiosus* ferredoxin electrochemically were unsuccessful. Voltammograms like the ones shown in Figure 9.11 were observed. Such voltammograms are similar to blank voltammograms. The observations were independent of the NaCl concentration. It was attempted to carry out the experiments both in the presence and absence of neomycin and cysteine and neither of the additives promoted a redox-signal in the present setup.
It is apparent that the molybdenum-sulfur analogues do not interact redox-actively with the working electrode used under the conditions used in this project. It was not attempted to use the phosphate buffer system that was tested for the $[Fe_3S_4]$ and $[Fe_4S_4]$ ferredoxins in chapter 5, since these proteins did not show any significant dif-

ferences between Tris/HCl and phosphate buffer. Changing the buffer system could, however, be an approach to reach a redox signal. Other working electrodes could also be tried to test if the molybdenum-sulfur analogues interact with these electrodes. Another approach could be to stabilize the protein by cooling. The current setup does not allow cooling, since the glove box did not have a cooling system installed and ice melted very quickly due to the lack of humidity control in the glove box.

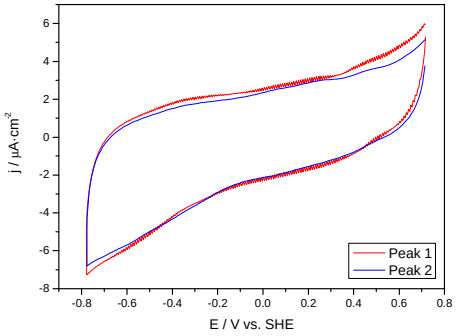

Figure 9.11: Cyclic voltammograms of the two species of molybdenum-sulfur analogues of *P. furiosus* ferredoxin as indicated in the figure in 20 mM Tris/HCl, pH 8.0, 0.1 M NaCl with 5 mM neomycin, 20 mV/s. Peak 1) 50 µM, peak 2) 25 µM.

9.8 EPR spectroscopic characterization of the molybdenum-sulfur analogues of *P. furiosus* ferredoxin

The molybdenum-sulfur analogues of *P. furiosus* ferredoxin have not been studied with EPR spectroscopy previously. The EPR spectroscopic characterization was introduced in this project.

The EPR spectroscopic characterization of $[Mo_4S_4(H_2O)_{12}]^{5+}$ in chapter 8.3 serve as reference for the studies of the molybdenum-sulfur analogue of *P. furiosus* ferredoxin. Assuming that the same oxidation states of the cluster are accessible for the aqueous complex and for the protein-bound cluster, the molybdenum-sulfur analogue is expected to be EPR active in the 5+ oxidation state, but EPR silent in surrounding 4+ and 6+ oxidation states.

Samples for EPR measurements were prepared in our laboratories and frozen and shipped in liquid N_2. EPR spectra were measured at Delft University of Technology by Professor Wilfred R. Hagen during my visits to his laboratories.

9.8.1 Experimental

EPR samples of purified and concentrated samples of peak 1 and peak 2 were prepared. No additives or mediators were added to these samples before freezing.

EPR-monitored redox titrations were carried out on purified samples of peak 1 and peak 2 samples, respectively, as described in chapter 4.3.3. Titrations were also carried out on samples synthesized with the ^{95}Mo-enriched $[Mo_4S_4]$ cluster.

The samples were frozen, stored and shipped in liquid N_2 and the spectra were measured at different low temperatures under cooling with liquid He. The instrumen-

tation and data analysis software are described in chapter 4.3.3.

9.8.2 Results and discussion

The samples of both peak 1 and peak 2 without addition of mediators were both EPR silent. That suggests that both peaks carry the molybdenum-sulfur in EPR silent oxidation states.

EPR-monitored redox titrations were carried out to study the proteins at other, potentially EPR active, oxidation states. A non-radical signal was observed to build up and disappear in the reductive titration of both peak 1 and peak 2. The spectra at 40 K are shown in Figure 9.12. Both spectra are disturbed by radical signals, particularly the peak 2 spectrum which corresponds to a lower potential, where the radicals are more abundant. Both species show similar features. The variations in the details between the spectra of the two species will described further below. The signal to noise ratio is low in the peak 2 spectra throughout the experiments and the more detailed analysis is therefore focused on the peak 1 spectra.

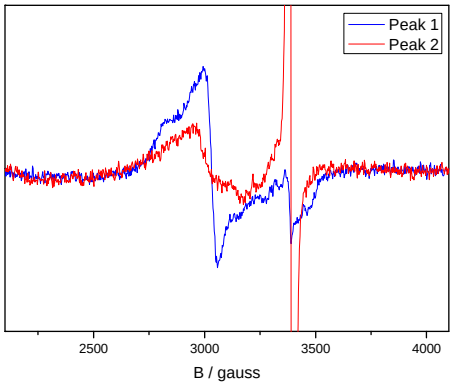

Figure 9.12: EPR spectra of the molybdenum-sulfur analogues of *P. furiosus* ferredoxin, natural abundance. Blue trace: Peak 1, 54 µM, E = -173 mV, ν = 9.3938 GHz. Red trace: Peak 2, 12 µM, E = -270, ν = 9.4058 GHz. T = 40 K, P = 12 dB, M = 8, G = $8 \cdot 10^5$.

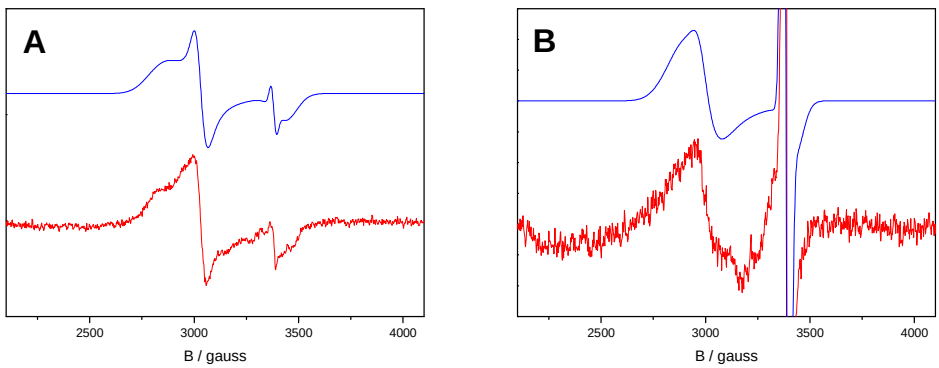

Figure 9.13: EPR spectra of the molybdenum-sulfur analogues of *P. furiosus* ferredoxin, natural abundance, with simulations. A) Peak 1. Red trace: experimental, 54 µM, E = -173 mV, ν = 9.3938 GHz, T = 40 K, P = 12 dB, M = 8, G = $8 \cdot 10^5$. Blue trace: simulation. B) Peak 2. Red trace: experimental, 12 µM, E = -270, ν = 9.4058 GHz, T = 40 K, P = 12 dB, M = 8, G = $8 \cdot 10^5$. Blue trace: simulation.

The spectra of peak 1 and peak 2 in Figure 9.12 are shown with simulated spectra in Figure 9.13A and Figure 9.13B, respectively. Both spectra are simulated with a non-radical protein spectrum and a weighted radical signal at g = 2.002. The peak 1 protein signal (Figure 9.13A) was simulated with g-values 1.967, 2.230 and 2.377 and g-strain effects of W_{xx} = 0.035, W_{yy} = 0.022, W_{zz} = 0.075 and W_{yz} = 0.015. The peak 2 protein signal (Figure 9.13B) was simulated with g-values 1.977, 2.242 and 2.362 and g-strain effects of W_{xx} = 0.025, W_{yy} = 0.045, W_{zz} = 0.070 and W_{yz} = 0.030.

Table 9.3: *g*-values of $[Mo_4S_4]$ clusters in the molybdenum-sulfur analogue species of *P. furiosus* ferredoxin and in the EDTA and aqua complexes.

	g_x	g_y	g_z
Peak 1	1.967	2.223	2.377
Peak 2	1.977	2.242	2.362
$[Mo_4S_4(H_2O)_{12}]^{5+}$ (chapter 8.3)	1.778	2.447	2.543
$[Mo_4S_4(edta)_2]^{3-}$ [82]	2.31	2.52	2.61

The g-values for peak 1 and peak 2 are listed in Table 9.3 along with the values of the inorganic complexes. The two spectra have the same features with only small variations in the parameters. The biggest differences are the larger g_z-value and less pronounced W_{yy} g-strain effect in the peak 1 spectrum. This makes the g_y and g_z lines more distinguishable for peak 1. Both protein spectra show resemblances to the spectrum of $[Mo_4S_4(H_2O)_{12}]^{5+}$ (Figure 8.3, chapter 8.3) and it is therefore inferred that this signal arises from the protein bound $[Mo_4S_4]$ cluster in the 5+ oxidation state. The spectra are more rhombic than the $[Mo_4S_4(H_2O)_{12}]^{5+}$ spectrum and the g_z-line is distinguishable from the g_y-line. The g_x-line is overlapped by the radical signal, but closer to the g_y- and g_z-lines than observed for $[Mo_4S_4(H_2O)_{12}]^{5+}$ making the protein spectra narrower than the spectrum of the aqueous complex. The narrower spectra are suggested to be an effect of the protein "screening" the molybdenum-sulfur cluster from the surroundings. The spectrum of the EDTA-ligated complex [82] is also narrower than the aqueous complex (chapter 8.3 and [83]) and it can be envisaged that similar screening effects arise from the hexadentate, enclosing EDTA-ligands and the protein amino acid chain wrapping in the cluster, the protein screening being more effective than the EDTA screening. The differences between the peak 1 and peak 2 spectra could arise from slightly different ligand environment as variations in the g-values between the $[Mo_4S_4]$ entity with H_2O and EDTA as ligands are also observed [82, 83].

The spin was quantified as described in chapter 4.2.5 nd suggested ½ spin per moleule This is the same spin as determined for $[Mo_4S_4(H_2O)_{12}]^{5+}$ [44] confirming $[Mo_4S_4]^{5+}$ as the source for the observed signal.

The peak 1 spectrum was measured at very low temperature as well and similar sigals appeared at 12.5 K and 40 K. In contrast to what was observed for $[Mo_4S_4(H_2O)_{12}]^{5+}$ (Figure 8.4, chapter 8.3), no additional signal build up at higher temperatures other than the signal observed at 12.5 K. These results suggest no occupation of EPR active

excited states in the temperature range tested.

The intensities of the spectra in the titration experiments with these signals were determined by double integration and subtraction of the intensity of the radical signal. All the spectra in each titration were recorded under the same conditions, but the protein concentration varied with the added volume of the $Na_2S_2O_4$ solution. The intensities at different potentials are plotted in Figure 9.14 with fitted curves according to the equation for a two-step reduction with an EPR active intermediate, Table 4.1, chapter 4.2.4. As stated above, the observed signal is attributed to the $[Mo_4S_4]^{5+}$ cluster. The cluster is assumed to be in the EPR silent $[Mo_4S_4]^{6+}$ state at higher potentials and is reduced to the also EPR silent $[Mo_4S_4]^{4+}$ state when further reduced.

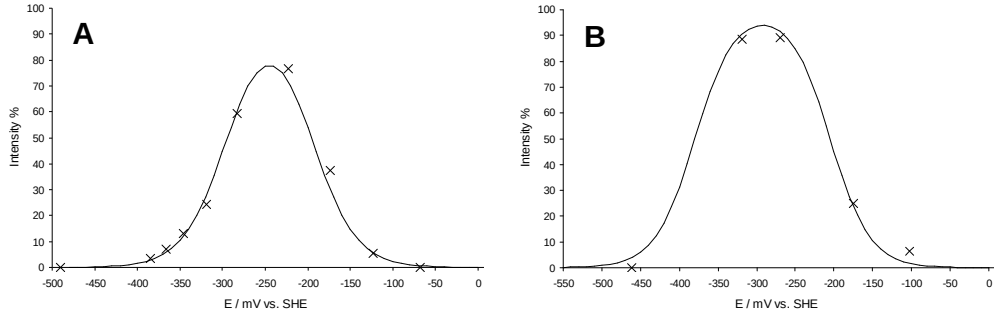

Figure 9.14: Titration data and fitted curves of the molybdenum-sulfur analogues of *P. furiosus* ferredoxin. x = Experimental data, line = fitted curve. A) Titration of peak 1, B) titration of peak 2.

Table 9.4: Formal potentials of fitted titration curves of the molybdenum-sulfur analogues of *P. furiosus* ferredoxin. Potentials given in mV vs. SHE.

	$E^{0'}{}_1$ ($[Mo_4S_4]^{5+/6+}$)	$E^{0'}{}_2$ ($[Mo_4S_4]^{4+/5+}$)
Peak 1	-195	-295
Peak 2	-205	-380

The formal potentials of the fitted curves in Figure 9.14 are given in Table 9.4. The potentials of both curves are too close for all the protein to be in the $[Mo_4S_4]^{5+}$ state as equilibrium with the reduced $[Mo_4S_4]^{4+}$ state or oxidized $[Mo_4S_4]^{6+}$ state will be established in stead of full conversion to $[Mo_4S_4]^{5+}$. The curves therefore never reach 100% intensity which corresponds to an all-$[Mo_4S_4]^{5+}$ containing sample. There is some uncertainty for the peak 2 curve since it is based on only very few data points and the spectra have a low signal-to-noise ratio making it difficult to determine the intensity precisely. It does, however suggest slightly different formal potentials for the peak 2 species, especially for the $[Mo_4S_4]^{4+/5+}$ redox couple where the intensity of peak 2 is close to the maximum at potentials where the intensity of peak 1 is decreased significantly (at approximately -325 mV versus SHE). The formal potentials are lower than the formal potentials of the aqua complex as well as the EDTA-ligated cluster, chapter 3.3 [44]. The potentials of the two redox transitions of both peak 1 and peak 2 are also closer than for the aqua and EDTA complexes. This indicates an interesting

tuning of the potentials by the protein.

The molybdenum-sulfur analogues were also studied with oxidative titrations. The EPR spectra for these titrations were dominated by the signal for $[Fe(CN)_6]^{3-}$, but an additional weak signal like the one shown in Figure 9.15 was observed in some samples. This signal did not appear systematically or build up as the potentials were increased. It was only observed at potentials between ~250 mV and ~420 mV versus SHE, but not observe for all samples in this range. The occurrence of the signal in different samples seemed random.

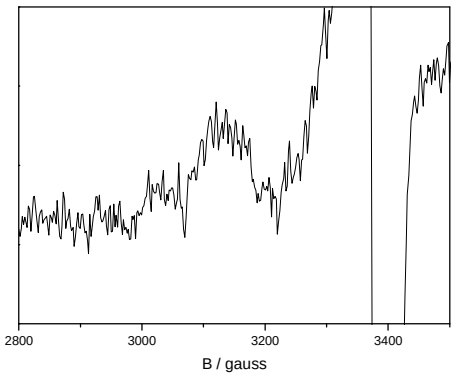

Figure 9.15: EPR spectrum of the molybdenum-sulfur analogues of *P. furiosus* ferredoxin at higher potentials. Peak 2, 10 µM, E = 353 mV, T = 40 K, ν = 9.3908 GHz, P = 12 dB, M = 8, G = $8 \cdot 10^5$.

The source of this signal was not known. It was suggested to arise from further oxidation of the EPR silent protein-bound $[Mo_4S_4]^{6+}$ cluster. Two sources for the signal can be envisaged: 1) Oxidative degradation of the cluster and formation of new paramagnetic species, or 2) Further oxidation of $[Mo_4S_4]^{6+}$ to a "super-oxidized" 7+ state. The 7+ state has not been identified previously, but the highly charged cluster could possibly be stabilized by the negatively charged protein. It is also possible that the 7+ state is an intermediate in the oxidative degradation. When the aqueous $[Mo_4S_4(H_2O)_{12}]^{6+}$ complex is oxidized further than the 6+ state, it breaks down to $[Mo_3S_4(H_2O)_9]^{4+}$ and a monomeric Mo(V) which is believed to dimerize spontaneously to a dimeric Mo(V). This break down suggestively goes through a $[Mo_4S_4]^{7+}$ state [44]. Both of these final degradation products, the $[Mo_3S_4]^{4+}$ and the dimeric Mo(V), are diamagnetic. It can, however, be envisaged that the paramagnetic monomeric Mo(V) or $[Mo_4S_4]^{7+}$ states can persist when bound to the protein. The seemingly random observation of the signal could suggest that the signal arises from momentarily "trapped" paramagnetic intermediates and that the occurrence of these species depends strongly on the potential, the stabilization time of the potentials and the time until the sample was frozen in liquid N_2.

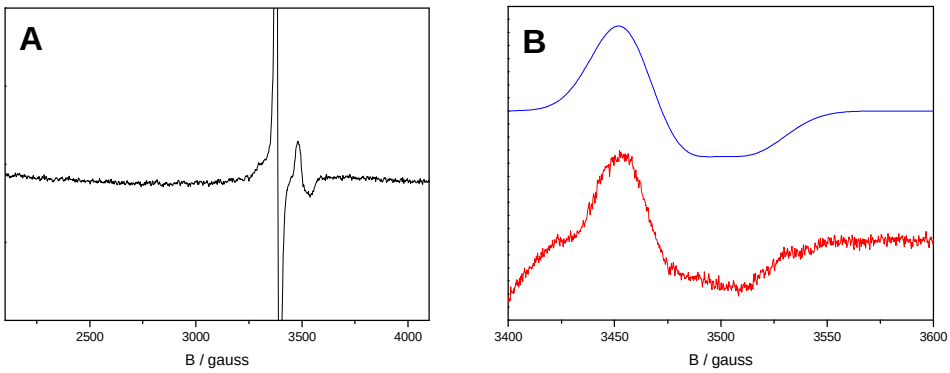

Figure 9.16: EPR spectrum after oxidation and re-reduction of the molybdenum-sulfur analogue of *P. furiosus* ferredoxin. Peak 1, "48 µM", E = -282 mV, T = 40 K. A) Wider field range, ν = 9.4009 GHz, P = 12 dB, M = 8, G = 8·10^5. B) Narrower field range. Red trace: ν = 9.4011 GHz, P = 12 dB, M = 8, G = 1.25·10^6. Blue trace: simulation.

The signal was further studied by reducing oxidized samples to see if the signal at lower potentials assigned to $[Mo_4S_4]^{5+}$ can be re-established. This re-reduction was not carried out as a titration, the solution was merely reduced to a potential where the $[Mo_4S_4]^{5+}$ would be present and a sample was taken out at this potential and frozen. Spectra of samples reduced to -282 mV versus SHE are shown in Figure 9.16. A signal appears in the 1.93 range and was simulated with *g*-values 1.943, 1.939 and 1.91. This signal is very different from the $[Mo_4S_4]^{5+}$ spectrum and renders the stabilization of $[Mo_4S_4]^{7+}$ at higher potentials improbable. The nature of the signal is not known. One possibility is that the signal arises from reduction of degradation products. The oxidized incomplete cuboidal $[Mo_3S_4(H_2O)_9]^{4+}$ is diamagnetic and EPR silent. To our knowledge, the reduced $[Mo_3S_4(H_2O)_9]^{3+}$ has not been studied with EPR. Such a study was not carried out in this project and it is therefore not possible to compare the observed spectrum to the spectrum of $[Mo_3S_4(H_2O)_9]^{3+}$ or other reduced degradation products.

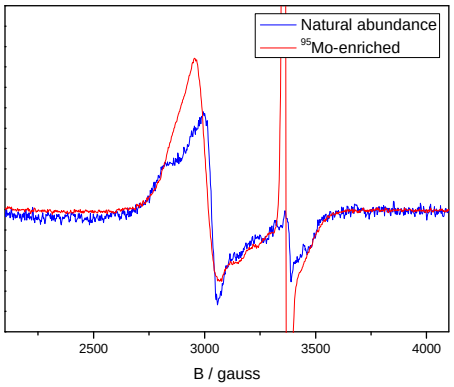

Figure 9.17: EPR spectra of the molybdenum-sulfur analogue of *P. furiosus* ferredoxin natural abundance and enriched in ^{95}Mo as indicated, adjusted for concentration difference. Natural abundance: 54 µM, E = -173 mV, ν = 9.3938 GHz. ^{95}Mo-enriched: 193 µM, E = -346 mV, ν = 9.3968 GHz. P = 12 dB, M = 8, G = 8·10^5, T = 40 K.

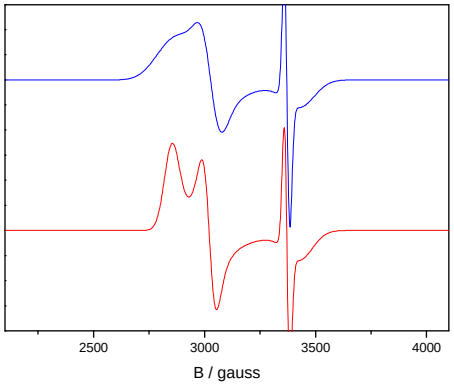

Figure 9.18: Illustration of the effect of weak hyperfine interactions on EPR spectra. The red trace shows the simulated spectrum with similar *g*-values as determined for the natural abundant spectrum in Figure 9.13A without hyperfine interactions or *g*-strain effects. The blue trace shows the same simulation with hyperfine splittings of 8, 8 and 20 from four Mo atoms with nuclear spin 2.5. *g*-strain effects were not simulated in this case since the simulation program does not allow simulation of both hyperfine interactions and *g*-strain effects.

The spectrum of the molybdenum-sulfur analogue with the ^{95}Mo-enriched cluster is shown in Figure 9.17 compared to the cluster with the natural abundance of Mo isotopes. The intensity of the radical signal is different in the two spectra since they are recorded on samples of different potentials. No distinct hyperfine lines appear upon enrichment, but the observed lines are broader. Such broadening can be an effect of hyperfine interactions with small hyperfine splittings where the lines are indistinguishable from one another as illustrated in Figure 9.18, which shows simulations of the spectrum with and without weak hyperfine interactions from four Mo atoms. These simulations are not perfect, since the simulation programs do not allow simulation of both hyperfine and *g*-strain effects at the same time. The simulations do, however, illustrate how weak hyperfine interactions can cause broadening such as observed in the EPR spectrum of the ^{95}Mo-enriched protein in Figure 9.17. These results indicate that the $[Mo_4S_4]$ cluster is indeed incorporated in the protein.The EPR spectroscopic studies suggest that both peak 1 and peak 2 species stabilize multiple oxidation states, with one state being EPR active. The EPR active state is attributed to protein carrying the $[Mo_4S_4]^{5+}$ cluster and the spectra of the ^{95}Mo-enriched protein confirm this suggestion.

The studies give some insights to the possible differences between the two species listed on page 82. Since the two untreated samples of peak 1 and peak 2 were both EPR silent, they are suggested not to exist in the $[Mo_4S_4]^{5+}$ oxidation state as purified. These results suggest that the protein is purified in one of the EPR silent $[Mo_4S_4]^{4+}$ or $[Mo_4S_4]^{6+}$ oxidation states. A difference in two charges should lead to a larger difference in conductivity than what is observed in the chromatograms in section 9.4. Different oxidation states are therefore ruled out as the difference between the two species. The spectra of the two species in the $[Mo_4S_4]^{5+}$ state show the same features, though small differences are observed. The differences between the two spectra could

arise from differences in the ligand environment. They suggest therefore that different exogenous ligands separate the peak 1 and peak 2 species. It is, however, not possible to identify the exogenous ligands based on these studies.

It is interesting that the results suggest stabilization of three oxidation states i.e. the 4+, 5+ and 6+ states. Ferredoxins normally only stabilize two oxidation states, the 1+ and 2+ states, of the $[Fe_4S_4]$ cluster and the cluster decomposes when oxidized further in ferredoxins. The 3+ state is only stabilized in HiPIPs. It is therefore surprising and very interesting that the *P. furiosus* ferredoxin seems to stabilize three oxidation states of the $[Mo_4S_4]$ cluster. The only iron-sulfur proteins known to stabilize the $[Fe_4S_4]$ cluster in three different oxidation states are the Fe-protein in *Azotobacter vinelandii* nitrogenase [24] and in the activator of 2-hydroxyglutaryl-CoA dehydratase from *Acidaminococcus fermentans* [25].

9.9 Conclusions

The molybdenum-sulfur analogue of *P. furiosus* ferredoxin has been synthesized and studied using chromatography, UV-vis spectrophotometry and EPR spectroscopy. Mass spectrometric and electrochemical characterization were also attempted.

The incorporation of the non-natural molybdenum-sulfur cluster into an iron-sulfur protein provides new insights in the understanding of iron-sulfur proteins and molybdenum-sulfur cluster complexes. The ability of the *P. furiosus* ferredoxin to incorporate the molybdenum-sulfur cluster not only demonstrates the flexibility of the ferredoxin, but also expands the research area of the chemical properties of molybdenum-sulfur clusters. The characterization of the new molybdenum-sulfur protein provides insights to the abilities of iron-sulfur proteins to tune the properties of the metal centers as well as insights to how to tune the properties of molybdenum-sulfur clusters.

The molybdenum-sulfur analogue was synthesized and purified based on previously prepared protocols adapted to preparation of the molybdenum-sulfur protein in a glove box. The purification of the molybdenum-sulfur protein inside the glove box disclosed two chromatographic peaks from separable species, termed peak 1 and peak 2, in the second purification step. The ratio between the two peaks varies between different experiments, but also within one experiment suggesting some interconversion between the two species. They are, however, stable after separation. The two peaks are suggested to arise from two closely related species, with peak 1 as the most stable form. The molar absorption coefficients were determined at 360 nm to $7.04 \cdot 10^3$ $M^{-1}cm^{-1}$ for peak 1 and $11.5 \cdot 10^3$ $M^{-1}cm^{-1}$ for peak 2 from UV-vis spectra and determination of the molybdenum content.

The incorporation of the molybdenum-sulfur cluster was confirmed by EPR spectroscopy, where a spectrum with the same features as the spectrum of $[Mo_4S_4(H_2O)_{12}]^{5+}$ was observed upon reductive titration. The signal was observed to build up and decrease suggesting 3 available oxidation states; the 4+, 5+ and 6+ oxidation states. The redox potentials of the two redox transitions were determined by fitting to

Nernstian curves to -195 mV and -295 mV versus SHE for peak 1 and -205 mV and -380 mV versus SHE for peak 2. Both peak 1 and peak 2 are suggested to carry the $[Mo_4S_4]$ cluster in the same EPR silent oxidation state, since non-treated samples of the purified samples were EPR silent. Based on the small differences in the spectra of the two peaks the two species are suggested to differ by different ligand environments. The spectra of the molybdenum-sulfur analogue with the ^{95}Mo-enriched cluster showed no distinct hyperfine interaction lines, but the observed broadening could be explained by weak hyperfine interactions from four interacting molybdenum atoms, thus confirming the incorporation of the intact $[Mo_4S_4]$ entity in the protein. The cluster seemingly breaks down upon oxidative titration.

CHAPTER TEN

10 Concluding Remarks

This thesis has presented studies on two artificial metalloproteins designed from iron-sulfur proteins as well as studies on iron-sulfur proteins that serve as reference for the new proteins. The two new metalloproteins were designed by incorporating non-natural metals in the metal center of the *P. furiosus* ferredoxin, thereby synthesizing a protein with a heteromtallic $[Fe_3CoS_4]$ cluster and a protein with a $[Mo_4S_4]$ cluster. The new proteins were purified and characterized by multiple techniques, including cyclic voltammetry and EPR spectroscopy.

The *P. furiosus* $[Fe_3S_4]$ and $[Fe_4S_4]$ ferredoxins were studied by cyclic voltammetry to establish the optimal conditions for electrochemical characterization of these and related proteins. The optimized conditions were used in the studies of the two artificial proteins.

The $[CoFe_3S_4]$ ferredoxin was synthesized and purified in the oxidized $[CoFe_3S_4]^{2+}$ state which proved to be stable under the presented conditions. The synthesis and high purity of the $[CoFe_3S_4]^{2+}$ ferredoxin was confirmed by mass spectrometry and EPR spectroscopy. The protein is redox active as confirmed both by reduction and oxidation experiments and by cyclic voltammetry. One well-defined pair of redox peaks appeared in cyclic voltammetry assigned to the $[CoFe_3S_4]^{2+/+}$ redox couple with a formal potential of -177 mV.

The anaerobic purification of the ferredoxin with an incorporated $[Mo_4S_4]$ cluster revealed two closely related species. Incorporation of the intact molybdenum-sulfur cluster was confirmed by EPR spectroscopy after reductive titration, which also suggested that the incorporated cluster is stable in three oxidation states. The two redox potentials of the transitions between the three oxidations states were determined from the titration curves. The EPR spectra of the two purified species suggest that the difference between them is variations in the ligand environment.

10.1 Outlook

This project includes the first multidisciplinary study of the *P. furiosus* $[CoFe_3S_4]$ ferredoxin and this protein is now very well-characterized. The next step is to start thorough investigations of the abilities of the protein to bind exogenous ligands and catalyze interesting chemical reactions. Such studies would be very intriguing and

support the potential of heterometallic clusters in iron-sulfur proteins in the design of new biologically based catalytic systems.

The molybdenum-sulfur analogue of *P. furiosus* ferredoxin is still in the initial characterization phase. Most pressing is the need to establish both the binding of the cluster to the protein and the ligand on the eight extra ligand sites. Such studies could be intriguing since the EPR spectra suggest variations in the ligands on the cluster. Information on the ligands and the binding to the protein could be obtained from crystal structure determinations, which do, however, require special advanced and expensive equipment as the protein is sensitive towards oxygen. Once the ligand environments are established, further characterization would include control of the exogenous ligands and exploration of the substrate binding and catalytic properties of the new protein.

Longer term studies would include detailed characterization of the molybdenum-sulfur analogue of HiPIPs and incorporation of the molybdenum-sulfur cluster into more complicated iron-sulfur proteins such as aconitase. Such studies would both substantiate the nature of the new class of molybdenum-sulfur proteins and could increase the understanding of the factors that determine the functions of iron-sulfur proteins. Also interesting would be incorporation of heterometallic [MMo_3S_4] clusters into iron-sulfur proteins. Such efforts hold exiting perspectives for new dimensions in metalloprotein design.

Bibliography

1) D. Ghosh and V. L. Pecoraro; Probing metal-protein interactions using a *de novo* design approach; *Curr. Opin. Chem. Biol.*; 2005; 9; 97-103.
2) D. E. Benson, M. S. Wisz and H. W. Hellinga; The development of new biotechnologies using metalloprotein design; *Curr. Opin. Biotechnol.*; 1998; 9; 370-376.
3) J. C. Fontecilla-Camps, P. Amara, C. Cavazza, Y. Nicolet and A. Volbeda; Structure-function relationships of anaerobic gas-processing metalloenzymes; *Nature*; 2009; 460; 814-822.
4) W. Fu, J. Telser, B. M. Hoffman, E. T. Smith, M. W. W. Adams, M. G. Finnegan, R. C. Conover and M. K. Johnson; Interaction of Tl^+ and Cs^+ with the $[Fe_3S_4]$ Cluster of *Pyrococcus furiosus* Ferredoxin: Investigation by Resonance Raman, MCD, EPR and ENDOR Spectroscopy; *J. Am. Chem. Soc.*; 1994; 116; 5722-5729.
5) R. Hernandez-Molina and A. G. Sykes; Chalcogenide-bridged cuboidal clusters with M_4Q_4 (M = Mo, W; Q = S, Se, Te) Cores; *J. Chem. Soc., Dalton Trans.*; 1999; 3137-3148.
6) J. Meyer; Iron-sulfur protein folds, iron-sulfur chemistry, and evolution; *J. Biol. Inorg. Chem.*; 2008; 13; 157-170.
7) H. Sticht and P. Rösch; The structure of iron-sulfur proteins; *Prog. Biophys. Mol. Biol.*; 1998; 70; 95-136.
8) H. Beinert, R. H. Holm and E. Münck; Iron-Sulfur Clusters: Nature's Modular, Multipurpose Structures; *Science*; 1997; 277; 653-659.
9) D. Bentrop, F. Capozzi and C. Luchinat; Iron-Sulfur Proteins; in Handbook on Metalloproteins; ed.: I. Bertini, A. Sigel and H. Sigel; 2001; Dekker; New York.
10) H. Beinert; Iron-sulfur proteins: ancient structures, still full of surprises; *J. Biol. Inorg. Chem.*, 2000; 5; 2-15.
11) W. Kaim and B. Schwederski; Bioinorganic Chemistry: Inorganic Elements in the Chemistry of Life, An Introduction and Guide; 1994; John Wiley & Sons Ltd; Stuttgart.
12) K. Fukuyama; Ferredoxins containing one [4Fe-4S] center; in Handbook of

Metalloproteins, ed: A. Messerschmidt, R. Huber, T. Poulos and K. Wieghardt; 2001; John Wiley & Sons, New York.

13) G. Wächtershäuser; From volcanic origins of chemoautotrophic life to Bacteria, Archaea and Eukarya; *Phil. Trans. R. Soc. B*; 2006; 361; 1787-1808.
14) M. R. Edwards; From a soup or a seed? Pyritic metabolic complexes in the origin of life; *Trends Ecol. Evol.*; 1998; 13; 178-181.
15) J. L. H. Busch, J. L. Breton, B. M. Bartlett, F. A. Armstrong, R. James and A. J. Thomson; [3Fe-4S] ↔ [4Fe-4S] cluster interconversion in *Desulfovibrio africanus* ferredoxin III: properties of an Asp^{14}→Cys mutant; *Biochem. J.*; 1997; 323; 95-102.
16) P. R. Gardner, I. Raineri, L. B. Epstein and C. W. White; Superoxide Radical and Iron Modulate Aconitase Activity in Mammalian Cells; *J. Biol. Chem.*; 1995; 270; 13399-13405.
17) A. Liu and A. Gräslund; Electron Paramagnetic Resonance Evidence for a Novel Interconversion of $[3Fe\text{-}4S]^{+}$ and $[4Fe\text{-}4S]^{+}$ Clusters with Endogenous Iron and Sulfide in Anaerobic Ribonucleotide Reductase Activase *in Vitro*; *J. Biol. Chem.*; 2000; 275; 12367-12373.
18) T. Glaser, I. Bertini, J. J. G. Moura, B. Hedman, K. O. Hodgson and E. I. Solomon; Protein Effects on the Electronic Structure of the $[Fe_4S_4]^{2+}$ Cluster in Ferredoxin and HiPIP; *J. Am. Chem. Soc.*; 2001; 123; 4859-4860.
19) C. W. Carter Jr., J. Kraut, S. T. Freer, R. A. Alden, L. C. Sieker, E. Adman and L. H. Jensen; A Comparison of Fe_4S_4* Clusters in High-Potential Iron Protein and in Ferredoxin; *Proc. Nat. Acad. Sci. USA*; 1972; 69; 3526-3529.
20) C. W. Carter Jr.; High potential iron sulfur proteins; in Handbook of Metalloproteins, ed: A. Messerschmidt, R. Huber, T. Poulos and K. Wiegehardt; 2001; John Wiley & Sons, New York.
21) A. Dey, F. E. Jenney Jr., M. W. W. Adams, E. Babini, Y. Takahashi, K. Fukuyama, K. O . Hodgson, B. Hedman and E. I. Solomon; Solvent Tuning of Electrochemical Potentials in the Actice Sites of HiPIP Versus Ferredoxin; *Science*; 2007; 318; 1464-1468.
22) H. A. Heering, Y. B. M. Bulsink, W. R. Hagen, and T. E. Meyer; Influence of Charge and Polarity on the Redox Potentials of High-Potential Iron-Sulfur Proteins: Evidence for the Existence of Two Groups; *Biochemistry*; 1995; 34; 14675-14686.
23) E. Babini, M. Borsari, F. Capozzi, L. D. Eltis and C. Luchinat; Experimental evidence for the role of buried polar groups in determining the reduction potentials of metalloproteins: the S79P variant of *Chromatium vinosum* HiPIP; *J. Biol. Inorg. Chem.*; 1999; 4; 692-700.
24) S. J. Yoo, H. C. Angove, B. K. Burgess, M. P. Hendrich and E. Münck; Mössbauer and Integer-Spin EPR Studies and Spin-Coupling Analysis of the $[4Fe\text{-}4S]^{0}$ Cluster of the Fe Protein from *Azotobacter vinelandii* Nitrogenase; *J. Am. Chem. Soc.*; 1999; 121; 2534-2545.

25) M. Hans, W. Buckel and E. Bill; Spectroscopic evidence for an all-ferrous [4Fe–4S]0 clusterin the superreduced activator of 2-hydroxyglutaryl-CoA dehydratase from *Acidaminococcus fermentans*; *J. Biol. Inorg. Chem.*; 2008; 13; 563-574.

26) G. Fiala and K. O. Stetter; *Pyrococcus furiosus* sp. nov. represents a novel genus of marine heterotrophic archaebacteria growing optimally at 100 °C; *Arch. Microbiol.*; 1986; 145; 56-61.

27) S. Aono, F. O. Bryant and M. W. W. Adams; A Novel and Remarkably Thermostable Ferredoxin from the Hyperthermophilic Archaebacterium *Pyrococcus furiosus*; *J. Bacteriol.*; 1989; 171; 3433-3439.

28) P. J. Silva, E. C. D. van den Ban, H. Wassink, H. Haaker, B. de Castro, F. T. Robb and W. R. Hagen; Enzymes of hydrogen metabolism in *Pyrococcus furiosus*; *Eur. J. Biochem.*; 200;0267; 6541-6551.

29) R. C. Conover, A. T. Kowal, W. Fu, J.-B. Park, S. Aono, M. W. W. Adams and M. K. Johnson; Spectroscopic Characterization of the Novel Iron-Sulfur Cluster in *Pyrococcus furiosus* Ferredoxin; *Jour. Biol. Chem.*; 1990; 265; 8533-8541.

30) M. S. Nielsen, P. Harris, B. L. Ooi and H. E. M. Christensen; The 1.5 Resolution Crystal Structure of $[Fe_3S_4]$-Ferredoxin from the Hyperthermophilic Archaeon *Pyrococcus furiosus*; *Biochemistry*; 2004; 43; 5188-5194.

31) M. N. Hasan, P. L. Hagedoorn and W. R. Hagen; *Pyrococcus furiosus* ferredoxin is a functional dimer; *FEBS Letters*; 2002; 531; 335-338.

32) M. N. Johannessen, M. S. Nielsen, B. L. Ooi, H. E. M. Christensen and P. Harris; In preparation.

33) ViewerLite 4.2, Copyright © 2001 Accelrys Inc.

34) A. Volbeda and J. C. Fontecilla-Camps; Structure-function relationship of nickel-iron sites in hydrogenase and a comparison with the active sites of other nickel-iron enzymes; *Coord. Chem. Rev.*; 2005; 249; 1609-1619.

35) Volbeda and J. C. Fontecilla-Camps; Structural bases for the catalytic mechanism of Ni-containing carbon monoxide dehydrogenases; *Dalton Trans.*; 2005; 5; 3443-3450.

36) Dance; The Hydrogen Chemistry of the FeMo-co Active Site of Nitrogenase; *J. Am. Chem. Soc.*; 2005; 127; 10925-10942.

37) Moura and J. J. G. Moura; Evidence for the Formation of a $CoFe_3S_4$ Cluster in *Desulfovibrio gigas* ferredoxin II; *J. Am. Chem. Soc.*; 1986; 108; 349-351.

38) M. G. Finnegan, R. C. Conover, J.-B. Park, Z. H. Zhou, M. W. W. Adams and M. K. Johnson; Electronic, Magnetic, Redox, and Ligand-Binding Properties of $[MFe_3S_4]$ Clusters (M = Zn, Co, Mn) in *Pyrococcus furiosus* Ferredoxin; *Inorg. Chem.*; 1995; 34; 5358-5369.

39) R. Staples, I. K. Dhawan, M. G. Finnegan, D. A. Dwinell, Z. H. Zhou, H. Huang, M. F. J. M. Verhagen and M. W. W. Adams; Electronic, Magnetic, and Redox Properties of $[MFe_3S_4]$ Clusters (M = Cd, Cu, Cr) in *Pyrococcus*

furiosus Ferredoxin; *Inorg. Chem.*; 1997; 36; 5740-5749.

40) K. P. Srivastava, K. K. Surerus, R. C. Conover, M. K. Johnson, J.-B. Park, M. W. W. Adams and E. Münck; Mössbauer Study of $ZnFe_3S_4$ and $NiFe_3S_4$ in *Pyrococcus furiosus* Ferredoxin; *Inorg. Chem.*; 1993; 32; 927-936.

41) A. Alberola, R. Llusar, C. Vicent, J. Andres, V. Polo and C. J. Gómez-Garcia; Synthesis and Molecular and Electronic Structures of a Series of Mo_3CoS_4 Cluster Complexes with Three Different Metal Electron Populations; *Inorg. Chem.*; 2008; 47; 3661-3668.

42) T. F. Jamarillo, J. Bonde, J. Zhang, B.-L. Ooi, K. Anderson, J. Ulstrup and I. Chorkendorff; Hydrogen Evolution on Supported Incomplete Cubane-type $[Mo_3S_4]^{4+}$ Electrocatalysts; *J. Phys. Chem. C*; 2008; 112; 17492-17498.

43) R. Hernandez-Molina, M. N. Sokolov and A. G. Sykes; Behavioural Patterns of Heterometallic Cuboidal Derivatives of $[M_3Q_4(H_2O)_9]^{4+}$ (M = Mo, W; Q = S, Se); *Acc. Chem. Rev.*; 2001; 34; 223-230.

44) T. Shibahara, H. Kuroya, H. Akashi, K. Matsumoto and S. Ooi; Synthesis and characterization of cubane-type clusters, $[Mo_4S_4(edta)_2]^{n-}$ (n = 2-4), $[Mo_4S_4(H_2O)_{12}]^{n+}$ (n = 4-6) and $[Mo_4S_4(NH_4)_{12}]^{4+}$. X-ray structures of $Na_2[Mo_4S_4(edta)_2]\cdot 6H_2O$, $Ca_{1.5}[Mo_4S_4(edta)_2]\cdot 13H_2O$, $Mg_2[Mo_4S_4(edta)_2]\cdot 20H_2O$, $[Mo_4S_4(H_2O)_{12}](CH_3C_6H_4SO_3)_5\cdot 14H_2O$ and $[Mo_4S_4(NH_3)_{12}]Cl_4\cdot 7H_2O$; *Inorg. Chim. Acta.*; 1993; 212; 251-263.

45) T. Richens; The Chemistry of Aqua Ions; 1997; John Wiley & Sons Ltd. England.

46) T. Sugano, T. Shibahara, H. Kobayashi, N. Uryû and M. Kinoshita; Magnetism and Electronic Structure of a Cubane-Type Mo_4S_4 Cluster; *Bull. Chem. Soc. Jpn.*; 1988; 61; 1785-1786.

47) W. McFarlane, M. Nasreldin, D. M. Saysell, Z.-S. Jia, W. Clegg, M. R. J. Elsegood, K. S. Murray. B. Moubaraki and A. G. Sykes; Spectroscopic, magnetic and structural studies on the mixed-valence cuboidal clusters $[Mo_4E_4(edta)_2]^{3-}$ (E = S or Se, H_4edta = ethylenediaminetetraacetic acid) and $[Mo_4S_4(H_2O)_{12}]^{5+}$; *J. Chem. Soc., Dalton Trans.*; 1996; 363-369.

48) F. A. Cotton, G. Wilkinson and P. L. Gaus; Basic Inorganic Chemistry; 3rd Ed.; 1995; John Wiley & Sons, Inc.; New York.

49) T. O'Sullivan and M. M. Millar; Synthetic and Study of an Analogue for the $[Fe_4S_4]^{3+}$ Center of Oxidized High-Potential Iron-Sulfur Proteins; *J. Am. Chem. Soc.*; 1985; 107; 4096-4097.

50) A. Müller, N. H. Schladerbeck and H. Bögge; $[Fe_4S_4(SH)_4]^{2-}$, the Simplest Synthetic Analogue for a Ferredoxin; *J. Chem. Soc., Chem. Commun.*; 1987; 35-36.

51) T. Herskovitz, B. A. Averill, R. H. Holm, J. A. Ibers, W. D. Phillips and J. F. Weiher; Structure and Properties of a Synthetic Analogue of Bacterial Iron-Sulfur Proteins; *Proc. Nat. Acad. Sci. USA*; 1972; 69; 2437-2441.

52) B. M. Segal; Terminal Ligand Assignments Based on Trends in Metal-Ligand

Bond Length of Cubane-Type $[Fe_4S_4]^{2+,+}$ Clusters; *Inorg. Chem.*; 1998; 37; 3440-3443.

53) M. Berg, K. O. Hodgson and R. H. Holm; Crystal Structure of $[(C_2H_5)_4N]_3[Fe_4S_4(SCH_2Ph)_4]$, a Reduced Ferredoxin Site Analogue with a Nontetragonal Fe_4S_4 Core Structure in the Solid State; *J. Am. Chem. Soc.*; 1979; 101; 4586-4592.

54) Martinez, B.-L. Ooi and A. G. Sykes; Reaction Paths in the Formation of Triangular and Cuboidal Molybdenum/Sulfur Cluster Complexes as Aqua Ions by Reduction of Molybdenum(V) Dimers; *J. Am. Chem. Soc.*; 1987; 109; 4615-4619.

55) T. Shibahara, M. Yamasaki, G. Sakane, K. Minami, T. Yabuki and A. Ichimura; Syntheses and Electrochemistry of Incomplete Cuboidal Cubane-Type Clusters with M_3S_4 Cores (M = Mo, W). X-Ray Structures of $[W_3S_4(H_2O)_9](CH_3C_6H_4SO_3)_4{\cdot}9H_2O$, $Na_2[W_3S_4(Hnta)_3]{\cdot}5H_2O$, and $(bpyH)_5$-$[W_3S_4(NCS)_9]{\cdot}3H_2O$; *Inorg. Chem.*; 1992; 31; 640-647.

56) A. Skoog, D. M. West and F. J. Holler; Fundamentals of Analytical Chemistry; 7th ed.; 1997; Saunders College Publishing; USA; ISBN: 0-03-005938-0.

57) J. Bard and L. R. Faulkner; Electrochemical Methods - Fundamentals and Applications; 1980; John Wiley & Sons, Inc.; USA; ISBN: 0-471-05542-5.

58) G. A. Mabbott; An Introduction to Cyclic Voltammetry; *Jour. Chem. Edu.*; 1983; 60; 697-702.

59) Southampton Electrochemistry Group; Instrumental Methods in Electrochemistry; 2001; Harwood Publishing Limited; England; ISBN: 1-898563-80-2.

60) R. S. Nicholson; Theory and Application of Cyclic Voltammetry for Measurement of Electrode Reaction Kinetics; *Anal. Chem.*; 1965; 37; 1351-1355.

61) W. R. Hagen; Biomolecular EPR Spectroscopy; 2009; CRC Press; ISBN: 978-1-4200-595-1

62) G. Palmer; Electron Paramagnetic Resonance of Metalloproteins; in Physical Methods in Bioinorganic Chemistry; ed.: L. Que, Jr.; 2000; University Science Books; ISBN: 1-891389-02-5.

63) W. R. Hagen; EPR spectroscopy as a probe of metal centres in biological systems; *Dalton Trans.*; 2006; 4415-4434.

64) W. R. Hagen; Wide zero field interaction distributions in the high-spin EPR of metalloproteins; *Mol. Phys.*; 2007; 105; 2031-2039.

65) W. R. Dunham and R. H. Sands; *g*-strain, ENDOR, and structure of active centers of two-iron ferredoxins; *Biochem. Biophys. Res. Commun.*; 2003; 312; 255-261.

66) S. S. Helt; Studies of ferredoxins and dCTP deaminase:dUTPase; PhD. thesis; Department of Chemistry; Technical University of Denmark; 2008.

67) Zhang, H. E. M. Christensen, B. L. Ooi and J. Ulstrup; In situ STM Imaging and Direct Electrochemistry of *Pyrococcus furiosus* Ferredoxin Assembled on

Thiolate-Modified Au(111) Surfaces; *Langmuir*; 2004; 20; 10200-10207.

68) Software accompanying the book in ref. 63. Can be downloaded from www.bt.tudelft.nl/biomolecularEPRspectroscopy (08-03-2009).

69) S. E. J. Fawcett, D. Davis, J. L. Breton, A. J. Thomson and F. A. Armstrong; Voltammetric studies of the reactions of iron-sulphur clusters ([3Fe-4S] or [M3Fe-4S]) formed in *Pyrococcus furiosus* ferredoxin; *Biochem. J.*; 1998; 335; 357-368.

70) N. Hasan, C. Kwakernaak, W. G. Sloof, W. R. Hagen and H. A. Heering; *Pyrococcus furiosus* 4Fe-ferredoxin, chemisorbed on gold, exhibit gated reduction and ionic strength dependent dimerization; *J. Biol. Inorg. Chem.*; 2006; 11; 651-662.

71) Kristensen; Electrochemical Studies on *Pyrococcus furiosus* [4Fe-4S]-Ferredoxin and a Molybdenum-Sulphur Analogue; M.Sc. thesis; Department of Chemistry, Technical University of Denmark; 2006.

72) H. Jankovics, J. Kristensen, S. Christophersen, M. S. Nielsen, H. Gudmundsdóttir, M. Martic, B. L. Ooi and H. E. M. Christensen; High-level expression of low-potential iron-sulfur proteins in Escherichia coli: Exemplified by expression of Pyrococcus furiosus ferredoxin; Article in preparation.

73) P. S. Brereton, M. F. J. Verhagen, Z. H. Zhou and M. W. W. Adams; Effect of Iron-Sulfur Cluster Environment in Modulating the Thermodynamic Properties and Biological Function of Ferredoxin from *Pyrococcus furiosus*; *Biochemistry*; 1998; 37; 7351-7362.

74) M. Martic and J. Kristensen; Unpublished results; Department of Chemistry; Technical University of Denmark; 2009.

75) H. Nørgaard; Characterization of Ancient Ferredoxins & *Chlamydia trachtomatis* Ribonucleotide Reductase; PhD. thesis; Department of Chemistry; Technical University of Denmark; 2009.

76) Benelli, I. Bertini, F. Capozzi and C. Luchinat; MFe_3S_4 (M = Zn, Co) Clusters in the Ferredoxin from *Clostridium acidi urici*; *Gazzetta Chimica Italiana*; 1994; 124; 469-474.

77) K. Y. Faridoon, H.-Y. Zhuang and A. Geoffrey Sykes; Kinetic Studies on the Reaction of M^{2+} Ions with Aconitase $Fe_3S_4^0$ To Give $Fe_3MS_4^{2+}$ Clusters (M = Fe, Mn, Co); *Inorg. Chem.*; 1994; 33; 2209-2212.

78) K. A. Johnson, M. F. J. M. Verhagen, P. S. Brereton, M. W. W. Adams og I. J. Amster; Probing the stoichiometry and oxidation states of metal centers in iron-sulfur proteins using electrospray FTICR mass spectrometry; *Anal. Chem.*; 72, 1410-1418; 2000.

79) Protein Structure: A Practical Approach, pp 208-211; Ed. T. E. Creighton; IRL Press; Oxford; 1989.

80) T. Shibahara, T. Yamamoto, H. Kanadani and H. Kuroya; Double-Cubane-Type Molybdenum-Sulfur Cluster Aqua Ion, $[(H_2O)_9Mo_3S_4MoS_4Mo_3(H_2O)_9]^{8+}$; *J. Am. Chem. Soc.*; 1987; 109; 3495-3496.

81) J. W. McDonald, G. D. Friesen, L. D. Rosenhein and W. E. Newton; Syntheses and Characterization of Ammonium and Tetraalkylammonium Thiomolybdates and Thiotungstenates; *Inorg. Chim. Acta.*; 1983; 72; 205-210.

82) P. W. Dimmock, J. McGinnis, B.-L. Ooi, and A. G. Sykes; Redox Interconversions and Aqueous Solution Properties of the Cuboidal Complexes $[Mo_4S_4(edta)_3]^{m-}$ (m = 4, 3, 2); *Inorg. Chem.*; 1990; 29; 1085-1089.

83) Y.-J. Li, M. Nasreldin, M. Humanes, and A. G. Sykes; Kinetics of 1:1 Thiocyanate (and Chloride) Substitution at Molybdenum on the Cuboidal Clusters $[Mo_4S_4(H_2O)_{12}]^{4+}$ and $[Mo_4S_4(H_2O)_{12}]^{5+}$ in Aqueous Solution; *Inorg. Chem.*; 1992; 31; 3011-3017.

84) T. Yamase; Multi-electron reduction sites of polymolybdates as photoredox catalysts; *Polyhedron*; 1986; 5; 79-86.

85) Baffert, J. F. Boas, A. M. Bond, P. Kögerler, D.-L. Long, J. R. Pilbrow and L. Cronin; Experimental and Theoretical Investigations of the Sulfite-Based Polyoxometalate Cluster Redox Series: α- and β-$[Mo_{18}O_{54}(SO_3)_2]^{4-/5-/6-}$; *Chem. -Eur. J.*; 2006; 12; 8472-8483.

86) Bevers and W. R. Hagen; One- and two-electron reduction of molybdate reversibly bound to the archaeal tungstate/molybdate transporter WtpA; *Dalton Trans.*; 2009; 8168-8170.

87) T. Sow; Design, Synthesis and Characterisation of Iron-Sulphur Proteins and a Novel Molybdenum Sulphur Analogue; Ph.D. Thesis; National University of Singapore; 1997; Chapter 4.

88) B. Caspersen; A Comprehensive Study of the High-Potential Iron-Sulfur Protein from *Rhodocyclus tenius* - From gene to double resonance spectroscopy; Ph.D. Thesis; Department of Chemistry; Technical University of Denmark; 2001.

89) G. K. Hansson and J. Kristensen; Studier af *Pyrococus furiosus* ferredoxin samt fremstilling og karakterisering af en artificiel molybdæn-svovl analog; B.Sc. Thesis; Department of Chemistry; Technical University of Denmark; 2004.

90) R. Drewsen; Synthesis and Preliminary Characterisation of Molybdenum-Sulfur Analogues of *Pyrococcus furiosus* Ferredoxin and *Ectothiorhodospira halophila* High Potential Iron-Sulfur Protein; M.Sc. Thesis; Department of Chemistry; Technical University of Denmark; 2004.

91) H. Baratne-Jankovics; Unpublished studies; Department of Chemistry, Technical University of Denmark.